https://technobius.kz/

e-ISSN 2789-7338

Technobius

A peer-reviewed open-access journal

Technobius, LLP *Volume 6, No. 2, 2026*

Technobius

Volume 6, No. 2, 2026

Special Issue on Advances in Civil Engineering Materials and Structures

A peer-reviewed open-access journal registered by the Ministry of Culture and Information of the Republic of Kazakhstan, Certificate № KZ26VPY00087928 dated 21.02.2024

ISSN (Online): 2789-7338
Thematic Directions: Construction, Materials Science
Publisher: Technobius, LLP
Address: 15/3 Sauran street, 43, 010000, Astana, Republic of Kazakhstan

Contacts:
Website: https://technobius.kz/
E-mail: technobius.research@gmail.com

CONTENTS

Technobius, 2026, 6(2), 0100, DOI: https://doi.org/10.54355/tbus/27897338.6.2.2026.0100

Technobius

https://technobius.kz/

e-ISSN 2789-7338

Review

Vibration diagnostics of beam bridges for serviceability assessment: a comparative analysis of international practice

Madina Zarlykova[1*], Denis Tsygulyov[1], Murat Karacasu[2]

[1]Department of Civil Engineering, L.N. Gumilyov Eurasian National University, 010008 Astana, Kazakhstan
[2]Department of Architecture and Civil Engineering, Eskişehir Osmangazi University, 26480 Eskisehir, Turkey
*Correspondence: madinazarlykova888@gmail.com

Abstract. Vibration-based methods are widely used in bridge assessment, yet their engineering interpretation for serviceability evaluation remains inconsistent across studies and national practice. This paper comparatively analyzes international practice in the vibration diagnostics of beam bridges with a focus on how measured dynamic response is translated into conclusions about operational suitability. The analysis covers field-oriented studies and review sources and compares excitation strategies, sensor layouts, measured parameters, interpretation routes, and links between diagnostic results and engineering decisions. Across the reviewed studies, the most frequently used indicators are natural frequencies, mode shapes, damping characteristics, and vibration response levels, since these quantities are sensitive to changes in stiffness, boundary conditions, and structural deterioration. The comparison also shows that these indicators are not equally informative across all field conditions and do not, by themselves, provide a uniform basis for serviceability assessment. Their practical value depends on the test organization, signal interpretation, and the extent to which vibration data are combined with structural models, inspection context, or baseline states. The paper identifies the most transferable findings from international practice and highlights considerations relevant to bridge networks that require practical, selective, and reproducible assessment procedures, including those in Kazakhstan.

Keywords: beam bridges, serviceability assessment, vibration diagnostics, operational modal analysis, bridge monitoring, structural health monitoring.

1. Introduction

The assessment of bridge serviceability cannot be reduced to simply recording the presence or absence of damage. In engineering terms, serviceability refers to a structure's ability to sustain operational actions at prescribed traffic speeds while maintaining an acceptable technical condition, reliability, and stability throughout its service life. For beam bridges, this means that the superstructure must remain fit for normal operation without unacceptable deformation, excessive vibration, accelerated deterioration, or loss of functional performance. A bridge may therefore retain sufficient load-carrying capacity while already exhibiting behavior that is unsatisfactory in routine service [1].

This issue becomes especially important when serviceability is interpreted only through deformation-based checks. The Federal Highway Administration (FHWA) study [2] on steel girder bridges showed that, within American AASHTO LRFD practice, deflection limits under the Service I load combination were historically used to control both excessive bridge vibrations and deformation-related damage, even though a single deflection criterion is insufficient for both tasks. The same report noted that criteria based on natural frequency reflect excessive vibration more adequately than deflection limits alone, whereas deterioration of the reinforced concrete deck is better represented by strain-related indicators [2]. This suggests that if serviceability is interpreted only as a deflection problem, part of the actual structural behavior remains outside the assessment framework.

For beam bridges, this is particularly relevant because changes in stiffness, support conditions, and operational regime are often reflected rather quickly in the dynamic response.

Under these conditions, vibration diagnostics has become increasingly important in bridge assessment. Vibration-based structural health monitoring studies [3] show that a structure's dynamic response can provide information about its actual condition. In bridge applications, this response reflects the effects of traffic, wind, impact, and other dynamic actions, while the most commonly used diagnostic parameters include natural frequencies, mode shapes, and damping ratios. These quantities are valuable because they are sensitive to changes in stiffness, mass distribution, boundary conditions, and structural deterioration. At the same time, they do not automatically translate into an engineering judgment on serviceability, since interpretation depends on structural context, field conditions, and the purpose of the investigation [3].

The engineering value of vibration diagnostics is also shaped by methodological diversity. Saidin et al. [3] distinguish between forced vibration testing and ambient vibration testing, that is, between tests with artificially introduced excitation and tests based on uncontrolled operational loading. The same review notes that the choice of testing strategy depends on structural size, access conditions, available equipment, and inspection objectives. In practice, bridge diagnostics is rarely performed under fully controlled conditions, so the usefulness of a method depends not only on sensitivity but also on reproducibility, labor demand, and compatibility with in-service operation.

At the same time, vibration diagnostics occupies an intermediate position between conventional inspection, load testing, and full-scale permanent structural health monitoring systems [3]. Unlike purely visual assessment, it provides access to the structure's actual dynamic behavior. Unlike permanent Structural Health Monitoring (SHM), however, it can also be applied as a one-time or periodic instrumented investigation, which is especially important for bridge networks where continuous monitoring of every structure is neither technically nor economically justified [3], [4].

Beam bridges are particularly suitable for comparative analysis because they are widely used and sufficiently repetitive in structural form to enable meaningful comparison of diagnostic approaches. In the reviewed literature, beam and girder systems frequently serve as the basis for operational assessment: the FHWA report analyzed a dataset of 195 steel girder bridges [2], while the Kazakhstan-based publication on the safe operation of artificial structures [1] directly considers vibration diagnostics for beam bridge superstructures. In that publication, the first natural frequency, the relative damping coefficient, and the relative midspan deformation or stress are proposed as informative parameters for technical-condition assessment. These indicators are important because they connect a measurable dynamic response with an engineering interpretation of structural condition.

Despite the growing number of studies in bridge monitoring and vibration-based assessment, the literature remains uneven in scope and emphasis. The review by Saidin et al. [3] focuses on vibration-based SHM, modal identification, and dynamic testing. In contrast, the review by Deng et al. [4] covers a much broader spectrum of bridge monitoring technologies, including sensors, computer vision, warning systems, and data processing. Both are useful, but neither is centered specifically on the comparative international practice of vibration diagnostics for beam-bridge serviceability assessment [3], [4]. By contrast, the FHWA report [2] is more directly connected to engineering decision-making, since it shows that the relationship between vibration, deformation, and deterioration is more complex than conventional code limits may suggest. The Kazakhstan-based publication [1] is also practice-oriented, but it does not extend to a structured comparison of international approaches, implementation conditions, or interpretation strategies. As a result, bridge vibration monitoring is well studied in general terms, whereas fewer works examine how vibration measurements are actually translated into serviceability-related engineering conclusions across different practical contexts [1], [3], [4].

For Kazakhstan, this issue has direct practical relevance. According to current official data, 1,335 bridge structures are in operation on republican roads, of which 735 are in good technical condition, 547 are assessed as satisfactory, and 53 require repairs of varying complexity (Figure 1). In terms of construction period, 341 bridges were built before 1980, 534 were commissioned between

1980 and 2015, and 460 were built after 2015 (Figure 2). By structure type, 1,144 bridges cross rivers and other water barriers, 151 are road overpasses, 21 are railway overpasses, and 19 are dry bridges (Source: JSC NC «KazAvtoZhol», official letter dated 03.03.2026). This bridge stock includes structures of different generations, designed under different regulatory conditions and operating under different service demands. Under such conditions, selective and technically interpretable diagnostic methods that can be applied when needed become especially valuable.

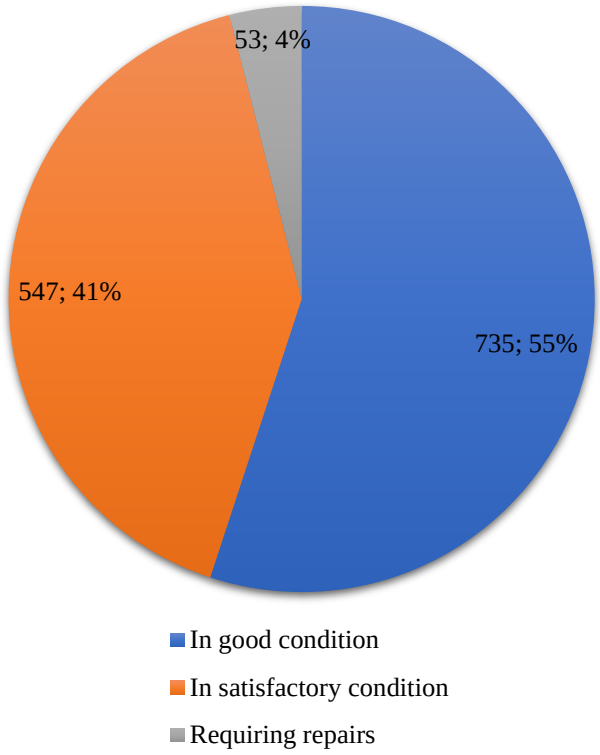

Figure 1 – Distribution of bridge structures on republican roads in Kazakhstan by technical condition

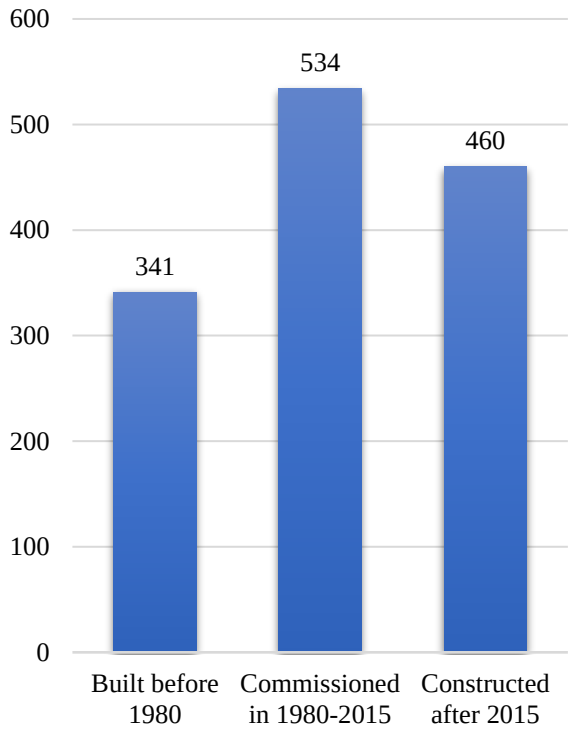

Figure 2 – Distribution of bridge structures on republican roads in Kazakhstan by construction period

Based on the above, this study aims to analyze international practices in vibration diagnostics of beam bridges and identify transferable diagnostic approaches, indicators, and interpretation strategies that can support practical serviceability assessment and maintenance decision-making for bridge structures.

2. Methods

This study employs a comparative analytical framework to examine international practices in vibration-based diagnostics for beam bridges. The primary objective is to evaluate how dynamic data is collected, processed, and translated into meaningful indicators of structural serviceability across different engineering traditions.

The literature was sourced from major engineering databases (including Scopus, Web of Science, ScienceDirect, and ASCE Library) covering the period from 2000 to 2025. This timeframe was chosen to capture the transition from traditional field-based modal testing to modern automated, output-only monitoring techniques.

The search strategy utilized targeted keyword combinations focusing on the intersection of bridge dynamics, modal analysis, and serviceability assessment. To ensure a comprehensive dataset, the initial search was supplemented by a backward reference check of seminal papers and case studies. The specific criteria for inclusion are detailed in Table 1.

Table 1 – Literature search and selection criteria

Criterion	Specification
Review type	Comparative analytical review
Methodological basis	PRISMA-inspired structured selection
Scope of structures	Reinforced concrete and steel beam bridges
Databases	Scopus, Web of Science, ScienceDirect, SpringerLink, ASCE Library, IEEE Xplore, TRID
Time window	2000–2026
Search fields	Title, abstract, keywords, plus backward reference checking
Main query groups	beam bridge and vibration diagnostics; bridge serviceability and modal analysis; vibration-based assessment and bridge; operational modal analysis and beam bridge; bridge monitoring and frequency and serviceability

To facilitate consistent comparisons across diverse studies, a standardized data-extraction protocol was used. Each publication was analyzed based on:

- Technical parameters: sensor configurations, excitation methods, and identified dynamic characteristics (frequencies, damping, mode shapes);
- Operational context: bridge material, span length, and regional environmental conditions;
- Engineering interpretation: the logic used to correlate vibration data with serviceability limits, maintenance decisions, and structural integrity.

This review treats vibration diagnostics as a continuous workflow – extending from raw measurement to final engineering judgment. Rather than viewing monitoring and manual inspection as competing domains, this study assumes they are complementary. Consequently, the evidence base includes both long-term monitoring systems and one-time diagnostic investigations, provided they offer actionable insights into the structure's operational state.

The methodology acknowledges several challenges inherent in this field. These include the inconsistent use of the term «serviceability» across different jurisdictions, a prevalent research focus on damage detection over operational assessment, and the fact that much practical experience remains locked in project-specific reports rather than standardized academic literature.

3. International experience and measurement strategies in vibration diagnostics of beam bridges

3.1 From modal testing to operational diagnostics: how international practice has evolved

International practice in bridge vibration diagnostics has evolved from controlled modal testing toward measurements under real operating conditions and, increasingly, toward operational modal analysis (OMA), in which modal parameters are identified from structural response to unknown input excitation [3], [5]. This shift reflects practical engineering constraints: for in-service bridges, controlled excitation is often expensive, labor-intensive, and only partially compatible with normal traffic, whereas output-only approaches and long-term monitoring enable measurements under actual service conditions.

In the reviewed European studies, vibration diagnostics is most often associated with long-term observation, environmental normalization, and statistical interpretation. On the Westend Bridge in Berlin, continuous monitoring was used to remove temperature-related effects from modal frequencies and to track possible prestress loss [6]. The Ponte Moesa Campagnola campaign in Switzerland combined ambient and forced vibration data on a prestressed concrete bridge with controlled artificial damage [7]. Taken together, these studies suggest that European practice often develops vibration diagnostics within a broader SHM framework rather than as a one-time extraction of a limited set of modal parameters [6], [7].

The North American line in the reviewed literature is defined less by the number of cases than by the structure of the diagnostic workflow. In the long-term VBSHM review, the Confederation Bridge is presented as a reference example of extended automated monitoring, including modal estimation, mode tracking, and sensor self-diagnostics [5]. Another influential direction is the development of deployable wireless systems. This is reflected in the Nine Wells Rail Bridge study, where measurements from a wireless accelerometer network were used directly for structural identification based on Finite Elements (FE) [8]. In this type of framework, vibration testing is not treated as an isolated measurement exercise, but as part of a model-supported engineering interpretation [5], [8].

The reviewed Asian studies are more strongly oriented toward field practicality and operational applicability. On the Sungai Raia UHPC bridge in Malaysia, ambient vibration testing was carried out under normal traffic conditions and was combined with FE model updating and serviceability verification [9]. In Japan, measurements were performed from an under-bridge maintenance walkway without traffic closure using a wireless system based on Microelectromechanical Systems (MEMS) [10]. The Indonesian case of the A.P. Pettarani Flyover Bridge represents a simpler but practically relevant configuration based on permanently installed accelerometers and processing with Fast Fourier Transform/Stochastic Subspace Identification (FFT/SSI) [11]. In this part of the literature, the emphasis is less on large-scale permanent SHM and more on feasible measurement schemes for bridges in regular service [9], [10], [11].

An important comparative observation is that the algorithms themselves do not primarily define international differences. The more meaningful distinction lies in what each study treats as the central engineering task: long-term interpretation, rapid field deployment, or minimal interference with bridge operation [6], [8], [10]. For comparative analysis, this distinction is more informative than a simple inventory of signal-processing methods.

3.2 Excitation methods, sensor layouts, and measurement campaign parameters

With respect to excitation, international practice shows clear recurring patterns. For in-service bridges, ambient and traffic-induced vibrations dominate, as they enable measurements without heavy excitation equipment or major traffic disruption [5], [8], [9], [10]. This is evident in the Sungai Raia bridge [9], the Nine Wells Rail Bridge [9], and the Japanese under-walkway system [10], where operational traffic served as the main excitation source. The broader review of long-term vibration-based SHM similarly emphasizes that the value of such systems lies in their ability to operate under real-world service uncertainty rather than under artificially controlled laboratory conditions [5].

Forced excitation remains relevant, but mainly in validation-oriented or benchmark studies. The Ponte Moesa campaign is a representative example in which both ambient and forced vibrations were recorded after artificial damage was introduced to a real prestressed concrete bridge [7]. Such campaigns are highly valuable for testing the sensitivity of diagnostic features, but they are too demanding for routine bridge-network assessment [7].

Impact-based express methods occupy a separate niche. In Bondar's method for railway beam bridges, the main diagnostic criterion is the first-mode vibration period, while excitation is introduced by a small impulse at midspan [12]. This approach is intended for periodic instrumental diagnostics rather than continuous monitoring. Its main advantage is operational simplicity, while its limitation is that it primarily captures the global structural response rather than a more complete modal portrait of the bridge.

Sensor layouts vary as much as excitation strategies. The reviewed studies range from compact short-session arrangements to dense long-term monitoring systems. Some cases rely on relatively moderate instrumentation, while others use larger sensor networks, higher sampling rates, and repeated-measurement configurations [12]. This variation does not point to a single "correct" instrumentation scale; rather, it indicates that the measurement configuration is selected based on the objective of the investigation.

To illustrate these differences, Figure 3 compares the instrumentation scale adopted in selected international case studies of vibration-based bridge diagnostics. The figure highlights the considerable variation in sensor deployment across different monitoring programs.

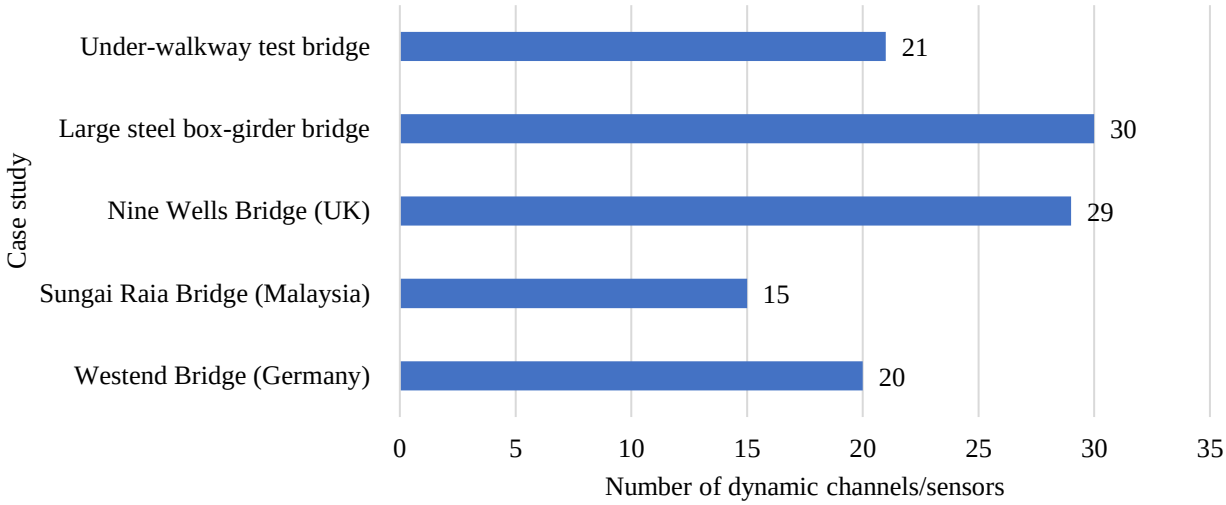

Figure 3 – Instrumentation scale in selected international case studies of vibration diagnostics for beam bridges

A similar pattern is observed in sampling frequency and record duration. As shown in Figure 4, the reviewed studies employ a wide range of sampling frequencies, reflecting differences in monitoring objectives, expected vibration characteristics, and data-processing requirements.

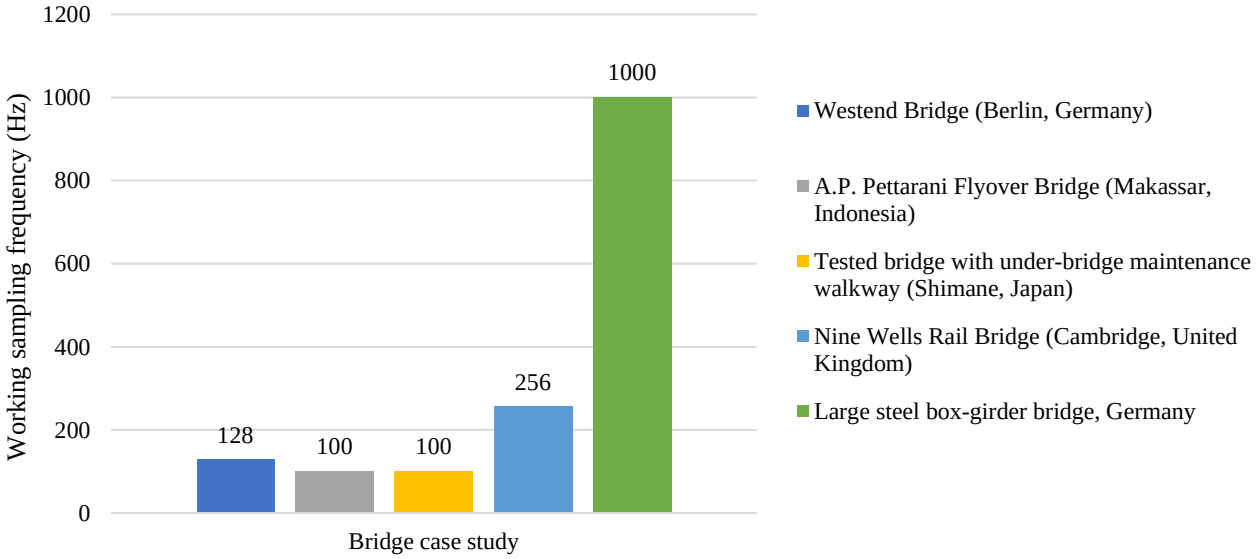

Figure 4 – Sampling frequency in selected bridge vibration-monitoring case studies

A compact comparison of the most informative case studies is presented in Table 2. The comparison indicates that the most informative diagnostic configuration is not necessarily the one with the largest number of sensors. In several studies, the key contribution lies in the clear link between measurement, signal processing, and engineering interpretation. This can be observed in the Sungai Raia bridge study, where the measured frequencies were validated against an updated FE model and serviceability criteria [11]. A similar approach was adopted in the German steel box-girder bridge case, where the identified modal properties were used to refine the numerical model and improve the interpretation of structural behavior [13].

Table 2 – Comparative characteristics of selected international vibration-diagnostic bridge case studies for condition assessment

Case study	Bridge type	Measurement setup	Key result
Westend Bridge, Germany [6]	Prestressed concrete box-girder bridge	20 vertical velocity sensors; 128 Hz; 32 s setup	Frequently excited modes at about 2.5, 3.4, 4.9, 7.8, and 8.9 Hz; long-term analysis was used to detect possible prestress loss.
Nine Wells Rail Bridge, UK [8]	Three-span prestressed reinforced-concrete bridge	29 accelerometers; 256 Hz	16 mode shapes were reconstructed, of which 10 were used for structural identification and FE updating
Sungai Raia UHPC Bridge, Malaysia [9]	Single-span UHPC bridge, 50 m	15 single-axis accelerometers; ambient vibration test	After model updating, the discrepancy for the first five frequencies was < 5%; the first dominant frequency was 3.348 Hz
Large steel box-girder bridge, Germany [14]	Steel box-girder bridge	30-channel system; 1000 Hz; 60 min per setup	9 modes were identified; the first five frequencies were 0.85, 2.03, 2.61, 4.22, and 4.76 Hz
Ponte Moesa Campagnola, Switzerland [7]	Three-span prestressed concrete bridge	7 triaxial accelerometers; 200 Hz; ambient + forced vibrations	4-day benchmark campaign after artificial damage; forced vibration level was about one order of magnitude higher than the ambient response
Underneath maintenance walkway wireless test, Japan [10]	In-service bridge tested from below	21 acceleration channels; 100 Hz; 5 min records	The dominant vertical frequencies were 2.34, 4.10, 10.30, 14.45, and 18.75 Hz; the deck–girder response comparison proved more informative.

3.3 What the International Experience Shows for Reinforced-Concrete and Steel Beam Bridges

The reviewed international experience shows that reinforced-concrete and steel beam bridges are not interpreted in the same way in vibration diagnostics.

For reinforced-concrete beam bridges, the dominant approach is to use vibration data to assess global structural behavior and support FE model refinement. This is evident in the Westend Bridge [6], the Nine Wells Rail Bridge [9], and the Sungai Raia UHPC bridge [9], where vibration measurements were interpreted primarily in terms of stiffness-related behavior and consistency with structural models. In these cases, vibration diagnostics is used less as a direct damage detector and more as a means of evaluating whether the bridge behaves as expected under service conditions [6], [8], [9].

For steel beam and box-girder systems, the reviewed studies indicate a greater need for detailed spatial interpretation and caution when evaluating frequency changes. On a large steel box-girder bridge in Germany, identified modal properties were used not only to validate but also to refine the numerical model [13]. Similarly, in the Japanese deck-damage study, the most valuable information was obtained not from frequency shifts alone but from comparing the relative responses of the bridge deck and the main steel girders [12]. These examples suggest that, for steel bridge systems, vibration diagnostics often relies on component-level assessment, environmental-effect filtering, and careful distinction between local and global structural responses [12].

An important conclusion from this section is that the reviewed literature does not support the existence of one universal measurement strategy for all beam bridges. For reinforced-concrete systems, the reviewed studies more often emphasize global stiffness behavior, FE calibration, and serviceability-oriented interpretation [6], [10]. For steel systems, they more often highlight the importance of relative-response comparison when local deterioration is not clearly reflected in a limited set of global frequencies [12].

Accordingly, for one-time inspection of beam bridges, the engineering value of a vibration-diagnostic approach appears to depend less on instrumentation density alone than on a balanced combination of excitation type, rational sensor layout, appropriate signal processing, and comparison with either a baseline state or a numerical model. For some railway and short-span structures under restricted-access conditions, a period-based express approach, such as Bondar's method, may also remain relevant [12]. In practical terms, international experience points not to one preferred measurement scheme, but to the need to match diagnostic depth to structural type and engineering objective.

4. Diagnostic indicators, serviceability interpretation, and transferability of approaches to Kazakhstan

4.1 Vibration-based diagnostic indicators and their interpretation in terms of serviceability

Among the indicators used in vibration diagnostics of beam bridges, natural frequency and vibration period remain the most consistently applied. Both are directly related to global structural stiffness, and their variation is commonly interpreted as a sign that the overall structural behavior of the span has changed. In the review on modal-based damage detection, frequency is described as a practically convenient global indicator because it is relatively easy to extract and compare. At the same time, in Bondar's Kazakhstan-oriented methodology, the principal evaluation criterion is explicitly defined as the vibration period of the first mode of a girder span [12]. In the UHPC bridge study from Malaysia, the first dominant frequency after FE-model updating was 3.348 Hz, and the discrepancy between the updated model and the first five measured frequencies was less than 5%, which allowed this parameter to be interpreted not only as a modal characteristic but also as an indicator relevant to serviceability assessment [9].

At the same time, frequency and period are useful only up to the point where the task shifts from identifying that a deviation exists to explaining what that deviation means structurally. Their main strength lies in their sensitivity to changes in global stiffness. Their main limitation is that local deterioration may have only a limited influence on the global modal response. As a result, the same indicator that performs well in rapid screening may be insufficient for an engineering judgment about the actual mechanism of deterioration [15].

Interpretation becomes more reliable when frequency is considered together with mode shapes and their consistency with the numerical model. In the field study of a simple beam bridge, the identified modal parameters were used to update the FE model after a relatively short instrumented campaign [13]. In the UHPC bridge study, model validation was additionally strengthened through the Modal Assurance Criterion (MAC), with the minimum MAC value exceeding 90% after updating [9]. This type of interpretation is more robust than relying on a single frequency because it compares not a single measured value but a set of dynamic characteristics against the expected structural behavior [13], [16].

Damping must be treated more cautiously. In principle, it reflects the dissipation of vibration energy and may therefore contain information about structural condition. In bridge testing practice, however, damping estimates are more sensitive than frequency to the identification method, signal quality, and excitation conditions. For this reason, in local studies on railway transport structures, damping is proposed not as an independent diagnostic criterion, but as one of several parameters together with the first frequency or period and relative midspan deformation or stress [1], [17]. This combined use is methodologically more realistic than any attempt to rely on a single modal indicator [1], [17].

The engineering meaning of serviceability-oriented interpretation becomes clearest when vibration-based indicators are compared with external performance criteria. In the UHPC bridge study, the identified dominant frequency was evaluated against serviceability requirements, and the authors concluded that it fell within the admissible range. However, the same study also demonstrated that serviceability limits depend on span configuration [11]. The relationship between natural

frequency and span length, together with the corresponding admissible serviceability range, is illustrated in Figure 5.

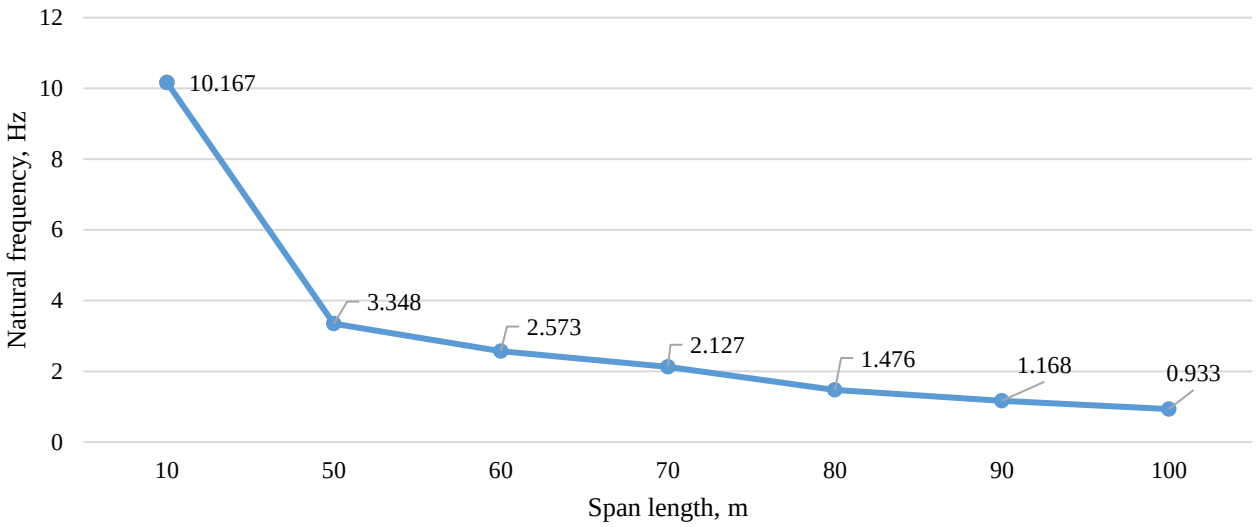

Figure 5 – Relationship between natural frequency and span length for the UHPC bridge, with the admissible serviceability range [9]

The FHWA report based on 195 steel girder bridges leads to an even more important engineering conclusion: a single deflection limit is insufficient, because excessive vibration is better controlled by a criterion based on natural frequency, whereas deterioration of the concrete deck is better represented by flexural tensile strain [2]. Bridge serviceability, in the dynamic sense, therefore, cannot be reduced to a single parameter. In most cases, it requires at least two lines of interpretation: one related to vibration behavior and another related to deformation-induced deterioration [2], [11].

4.2 Limits of interpretation and the integration of vibration diagnostics with inspection, load testing, and FE modeling.

The main limitation of vibration-based diagnostics is not that it fails to detect change, but that it cannot always explain that change reliably on its own. In review [15], this boundary is formulated through Rytter's damage-detection levels: when only vibration data are used, it is realistic to expect detection, localization, and partial assessment of damage, but not a reliable prediction of remaining service life without a sufficiently developed numerical and engineering framework. This is a fundamental limitation because it dispels the misleading assumption that a single set of modal parameters can replace inspection, structural analysis, and engineering judgment [15].

Accordingly, in well-designed field studies, vibration testing is rarely conducted in isolation from finite-element modeling. In the study of a simple beam bridge, a numerical model was used prior to field measurements to identify expected modes, select reference points, and design the sensor layout [13], [18]. This type of workflow is particularly informative for one-time inspections: the field test remains relatively short, but its interpretation is grounded in the actual structural scheme rather than in an isolated set of spectral peaks [13].

In more complex cases, the role of engineering context becomes even more important. For the retrofitted bridges B1 and B2 in Central Italy, ambient vibration tests were performed after the interventions to verify whether the post-retrofit dynamic behavior of the structures was consistent with the engineering intent of the strengthening scheme [19]. In this context, OMA does not function as a universal "damage detector," but as a tool for checking whether the bridge behaves as expected after repair or modification [19].

A separate but equally important issue is the influence of the environment, especially temperature. The review on temperature effects states explicitly that temperature-induced changes in modal properties may be comparable to, or even larger than, those caused by damage; if such effects

are not accounted for, vibration-based diagnostics may produce both false positives and false negatives [20]. The West End Bridge provides a clear long-term example of this problem. In that study, modal features were extracted from continuous measurements, temperature effects were filtered using multiple linear regression, and interpretation was based on a health index derived from residual trends rather than on raw frequency shifts alone [6]. This is an important methodological point: once environmental variability becomes significant, the condition of the structure can no longer be interpreted through a single frequency value. Only a normalized trend relative to the bridge's own baseline remains meaningful [6], [20].

Even after such normalization, one more limitation remains: the scale of damage. This leads to an important practical conclusion. Vibration diagnostics works well when the task is to detect a system-level change in structural behavior. However, when the problem concerns local corrosion, crack opening, bearing condition, or a defensible prediction of remaining life, reliable interpretation usually cannot be achieved without combining vibration data with inspection, deformation measurements, and a numerical model [16].

4.3 Transferability of international approaches to Kazakhstan and criteria for method selection under local conditions

For Kazakhstan, the key question is not whether international experience in vibration diagnostics can be used, but which elements of that experience can be transferred in a technically realistic and economically justified way. Since the national bridge stock is heterogeneous in age, technical condition, structural configuration, and likely also in the completeness of available design and maintenance records, the direct transfer of one uniform monitoring strategy to all bridges would be methodologically weak. What is needed instead is a differentiated selection of diagnostic approaches according to bridge type, expected deterioration mechanism, availability of reference data, and the level of engineering decision required.

Table 3 – Comparative evidence on vibration-based diagnostic indicators, serviceability interpretation, and applicability to Kazakhstan

Bridge/sample	Main indicator(s)	Key result and serviceability interpretation	Relevance for Kazakhstan
UHPC single-span bridge [9]	Natural frequency, MAC, FE updating	The difference between the updated FE and the measured first five frequencies was <5%; the minimum MAC was 90%.	Suitable for one-time assessment when a benchmark FE model is available.
195 steel girder bridges [2]	Natural frequency, deck tensile strain	Deflection alone was found insufficient; natural frequency was proposed for vibration comfort, while flexural tensile strain was proposed for deck deterioration.	Useful as a framework for separating vibration-related serviceability from structural deterioration.
Westend Bridge, Berlin (2000–2013) [6]	Frequency trends, normalized novelty index, tendon strain	Baseline was built from the first year; NI indicators increased after 2008; tendon strain changed from 85.29 to −43.99 μmm/mm. Interpretation was based on deviation from a normalized baseline.	Appropriate for strategically important bridges, but too complex for routine network-wide use.
Two retrofitted multi-span prestressed RC bridges (B1, B2) [19]	OMA, frequencies, mode shapes	AVTs used 30 min records at 2048 Hz; 6 tests for B1 and 8 for B2; identified frequencies were 2.04–6.31 Hz for B1 and 1.05–4.44 Hz for B2. Dynamic testing was used for post-retrofit verification.	Relevant for bridges after repair, strengthening, or bearing replacement.
Railway girder spans [12]	Vibration period under small impulse action	Express diagnostics is based on the response to "a person's jump"; the main criterion is the vibration period of the first mode.	Highly relevant for low-cost periodic assessment of typical beam spans.
Railway bridges under operational loads [1], [17]	First frequency or period, relative damping, midspan deformation/stress	Condition assessment is based on comparing measured dynamic and deformation parameters with those of a defect-free model.	Directly relevant to Kazakhstan because it aligns with local railway monitoring practices.

As shown in Table 3, the reviewed studies differ not only in the indicators they use, but also in the engineering logic through which vibration results are translated into serviceability decisions. This distinction is especially important for Kazakhstan, where typical beam spans, repaired bridges, and strategically important structures cannot reasonably be assessed with the same diagnostic depth.

For a large and heterogeneous bridge network, the more realistic option is not the most technologically complex SHM scenario, but periodic instrumental inspections based on a limited yet interpretable set of indicators. This logic is clearly reflected in Bondar's methodology, where express diagnostics of reinforced-concrete and steel girder railway spans is performed using a small impulse excitation and the first-mode vibration period as the main evaluation criterion [12]. This scheme does not address every diagnostic problem, but for typical beam spans, it is considerably closer to engineering reality than permanent continuous monitoring at every structure.

Local Kazakhstan-oriented publications move in a similar direction, though in a somewhat more explicitly engineering form. In studies [17], the proposed technical-condition parameters include the first natural frequency or period, the relative damping ratio, and the relative midspan deformation or stress. Condition assessment is based not on a single measured number alone, but on a comparison between field-test results and the calculated parameters of a defect-free structural model. For Kazakhstan, this appears to be one of the most practically transferable diagnostic logics: first, a rapid vibration-based inspection, then comparison with a numerical scheme, and only after that a decision on whether deeper investigation is required [1], [17].

This directly leads to the criteria for method selection. For typical short and medium beam spans, when the task is screening and identifying possible signs of stiffness loss, a rapid scheme based on the first frequency or period, with a minimal sensor set and subsequent comparison against a benchmark or analytical model, appears rational [12], [13], [17]. For strategic or already problematic bridges, where tracking of slow deterioration is critical, long-term monitoring with temperature normalization and statistical indices is justified – but only as a selective scenario, not as a universal practice for the whole network [6].

Ultimately, international experience is most transferable to Kazakhstan not as a single ready-made technology, but as a hierarchy of approaches. At the lower level, frequency or period serves as a rapid indicator of a general change in structural behavior. At the next level, mode shapes and FE modeling are added when it becomes necessary to understand not only that a deviation exists, but what it means structurally. Only at the upper level does long-term SHM with temperature normalization and statistical pattern recognition become justified, and then only where the structure truly warrants it. For local bridge practice, this three-level logic appears more realistic and useful than any attempt to force all serviceability problems into a single universal monitoring scheme.

5. Discussion

The comparative analysis shows that international experience in the vibration diagnostics of beam bridges remains methodologically heterogeneous rather than fully unified. Different practical lines coexist in the current literature, including one-time field testing, long-term vibration-based monitoring, operational modal analysis, and, more recently, indirect and AI-assisted approaches [5], [21], [22], [23], [24], [25]. At the same time, one stable pattern is evident across the reviewed studies: frequency-based interpretation and OMA-based analysis remain central to practical bridge vibration diagnostics [8]. Serviceability is rarely measured directly. In most cases, it is inferred through changes in modal parameters, stiffness-related response, or the degree of consistency between measured vibration behavior and an expected structural model [5], [26].

From an engineering perspective, vibration diagnostics should not be treated as a self-sufficient decision tool. Its main strength lies in the ability to detect and interpret changes in structural behavior under operational conditions. Its main limitation is that such changes do not always explain themselves. For this reason, the reviewed studies repeatedly show that reliable serviceability assessment requires not only vibration data, but also structural context, inspection results, and, where necessary, FE-supported interpretation [26].

This is also why the most practically useful distinction in the reviewed literature is not between traditional and advanced algorithms, but between different levels of diagnostic purpose. Some studies are aimed at rapid field screening, others at post-repair verification, and others at long-term tracking of deterioration under environmental and operational variability [5], [19]. These are not interchangeable tasks, and they should not be forced into one universal monitoring scheme. A method that is sufficient for identifying a possible change in stiffness may still be insufficient for explaining a local defect, evaluating the effect of repair, or supporting maintenance prioritization.

Indirect and AI-assisted approaches are promising, especially for rapid screening of large bridge stocks, but their current engineering role remains limited [23], [24], [25]. Indirect monitoring is operationally attractive because it reduces the need for bridge-mounted instrumentation, yet extracting bridge-specific information from vehicle responses remains sensitive to vehicle–bridge interaction and road roughness [23], [24]. Similarly, AI-based methods are likely to become more useful for serviceability-oriented bridge assessment only if they become more interpretable, more robust to incomplete and noisy field data, and more transferable across bridge types and operational conditions [25]. At present, such methods are better viewed as supplementary tools rather than as replacements for measurement-based engineering interpretation.

The reviewed studies also indicate that future progress in beam-bridge vibration diagnostics depends less on increasing data volume alone than on improving the interpretability and reproducibility of the full diagnostic chain. This includes baseline definition, resistance to environmental and operational variability, automated but controllable mode tracking, and a clearer relationship between measured dynamic response and engineering decisions [5], [25], [27], [28]. In practical terms, the main methodological challenge is not simply to detect a dynamic deviation, but to establish when that deviation is meaningful for serviceability assessment and when it is not.

Overall, the review leads to several conclusions. First, international practice does not support one universal vibration-diagnostic scheme for all beam bridges. The engineering value of vibration measurements depends not only on the identified parameters but also on how they are interpreted in relation to structural behavior, inspection findings, baseline state, and numerical modeling [5], [26]. Second, reinforced-concrete and steel beam bridges require partly different diagnostic emphases: the former are more often assessed through global stiffness-related behavior and model consistency, whereas the latter more often require environmental filtering, denser spatial interpretation, or relative-response comparison [1], [17]. Third, for bridge networks such as those considered in this article, the most realistic strategy is not universal continuous monitoring, but a selective hierarchy of approaches ranging from rapid frequency- or period-based screening to OMA- and FE-supported assessment and, where justified, long-term SHM [6], [12].

For Kazakhstan, this conclusion is particularly important. The most transferable international experience is not a single ready-made technology, but a differentiated diagnostic logic matched to the bridge type, the expected deterioration mechanism, and the required decision level [1], [17]. For typical short- and medium-beam spans, rapid instrumental assessment based on the first frequency or period may be sufficient for screening. For repaired or modified bridges, OMA combined with FE support is more appropriate. For strategically important or already problematic structures, long-term monitoring with environmental normalization may be justified, but only selectively [6], [17]. In this sense, the practical future of vibration diagnostics lies not in methodological expansion alone, but in the development of reproducible, engineering-oriented procedures that can be adapted to real bridge networks and operating conditions.

References

[1] N. Makhmetova, M. Kvashnin, I. Bondar, and V. Shultz, “Ensuring safe operation of artificial structures,” *Bull. KazATC*, vol. 128, no. 5, pp. 28–37, Oct. 2023, doi: 10.52167/1609-1817-2023-128-5-28-37.

[2] M. G. Barker and J. Staebler, “Servicability limits and economical steel bridge design,” in *Report No. FHWA-HIF-11-044*, Washington DC, USA: Federal Highway Administration, 2011, p. 93.

[3] S. S. Saidin, A. Jamadin, S. Abdul Kudus, N. Mohd Amin, and M. A. Anuar, “An Overview: The Application of Vibration-Based Techniques in Bridge Structural Health Monitoring,” *Int. J. Concr. Struct. Mater.*, vol. 16, no. 1, p. 69, Dec. 2022, doi: 10.1186/s40069-022-00557-1.

[4] Z. Deng, M. Huang, N. Wan, and J. Zhang, "The Current Development of Structural Health Monitoring for Bridges: A Review," *Buildings*, vol. 13, no. 6, p. 1360, May 2023, doi: 10.3390/buildings13061360.
[5] S. Desjardins and D. Lau, "Advances in intelligent long-term vibration-based structural health-monitoring systems for bridges," *Adv. Struct. Eng.*, vol. 25, no. 7, pp. 1413–1430, May 2022, doi: 10.1177/13694332221081186.
[6] W.-H. Hu, D.-H. Tang, J. Teng, S. Said, and Rolf. G. Rohrmann, "Structural Health Monitoring of a Prestressed Concrete Bridge Based on Statistical Pattern Recognition of Continuous Dynamic Measurements over 14 years," *Sensors*, vol. 18, no. 12, p. 4117, Nov. 2018, doi: 10.3390/s18124117.
[7] Y. Reuland, L. Garcia-Ramonda Estevez, P. Martakis, S. Bogoevska, and E. Chatzi, "A full-scale case study of vibration-based structural health monitoring of bridges: prospects and open challenges," *ce/papers*, vol. 6, no. 5, Sep. 2023, doi: 10.3929/ETHZ-B-000665062.
[8] M. J. Whelan, M. V. Gangone, K. D. Janoyan, N. A. Hoult, C. R. Middleton, and K. Soga, "Wireless operational modal analysis of a multi-span prestressed concrete bridge for structural identification," *Smart Struct. Syst.*, vol. 6, no. 5_6, pp. 579–593, Jul. 2010, doi: 10.12989/SSS.2010.6.5_6.579.
[9] S. S. Saidin *et al.*, "Operational modal analysis and finite element model updating of ultra-high-performance concrete bridge based on ambient vibration test," *Case Stud. Constr. Mater.*, vol. 16, p. e01117, Jun. 2022, doi: 10.1016/j.cscm.2022.e01117.
[10] L. Li and T. Ohkubo, "Wireless vibration testing and bridge deck damage identification using underneath maintenance walkway," *Sci. Rep.*, vol. 14, no. 1, p. 25247, Oct. 2024, doi: 10.1038/s41598-024-77179-y.
[11] M. Akbar, A. Aminullah, and A. Awaludin, "Operational Modal Analysis of a Box Girder Bridge using Fast Fourier Transform and Stochastic Subspace Identification," *INERSIA J. Tek. Sipil Dan Arsit.*, vol. 21, no. 2, pp. 270–280, 2025, doi: 10.21831/inersia.v21i2.83380.
[12] I. S. Bondar, P. G. Khardikov, D. T. Aldekeyeva, and R. S. Imambaeva, "Methodology for determining the period of vibrations of beam span structures of bridges," *Bull. Kazakh Lead. Acad. Archit. Constr.*, vol. 83, no. 1, pp. 127–133, Jan. 2022, doi: 10.51488/1680-080X/2022.1-07.
[13] I. G. Araujo, E. Maldonado, and G. C. Cho, "Ambient vibration testing and updating of the finite element model of a simply supported beam bridge," *Front. Archit. Civ. Eng. China*, vol. 5, no. 3, pp. 344–354, Sep. 2011, doi: 10.1007/s11709-011-0124-8.
[14] R. Schneider, P. Simon, F. Hille, R. Herrmann, and M. Baeßler, "Vibration-based system identification of a large steel box girder bridge," *J. Phys. Conf. Ser.*, vol. 2647, no. 18, p. 182039, Jun. 2024, doi: 10.1088/1742-6596/2647/18/182039.
[15] J. J. Moughty and J. R. Casas, "A State of the Art Review of Modal-Based Damage Detection in Bridges: Development, Challenges, and Solutions," *Appl. Sci.*, vol. 7, no. 5, p. 510, May 2017, doi: 10.3390/app7050510.
[16] O. Krutikov, I. Gershuni, and D. Ryzhov, "Evaluation of the self-induced vibrations modes of bridge superstructure during monitoring," *Russ. J. Transp. Eng.*, vol. 9, no. 2, p. 01SATS222, Jun. 2022, doi: 10.15862/01SATS222.
[17] M. Ya. Kvashnin, S. E. Bekzhanova, A. S. Akbayeva, I. S. Bondary, and A. Kurbenov, "On the question of safe operation of artificial structures of railways," *Bull. Kazakh Lead. Acad. Archit. Constr.*, vol. 79, no. 1, pp. 229–240, Mar. 2021, doi: 10.51488/1680-080X/2021.1-30.
[18] A. De Angelis, G. Esposito, G. Maddaloni, E. Cosenza, and M. R. Pecce, "Ambient vibration test on an existing prestressed conctere bridge," in *Proceedings of the 8th International Conference on Computational Methods in Structural Dynamics and Earthquake Engineering*, Athens, Greece: Institute of Research and Development for Computational Methods in Engineering Sciences (ICMES), 2021, pp. 3720–3730. doi: 10.7712/120121.8741.18728.
[19] V. Nicoletti, R. Martini, L. Amico, S. Carbonari, and F. Gara, "Operational modal analysis for supporting the retrofit design of bridges," *ce/papers*, vol. 6, no. 5, pp. 1182–1188, Sep. 2023, doi: 10.1002/cepa.2125.
[20] J. Luo, M. Huang, and Y. Lei, "Temperature Effect on Vibration Properties and Vibration-Based Damage Identification of Bridge Structures: A Literature Review," *Buildings*, vol. 12, no. 8, p. 1209, Aug. 2022, doi: 10.3390/buildings12081209.
[21] C. Qu, G. Tu, F. Gao, L. Sun, S. Pan, and D. Chen, "Review of Bridge Structure Damping Model and Identification Method," *Sustainability*, vol. 16, no. 21, p. 9410, Oct. 2024, doi: 10.3390/su16219410.
[22] Z. Li, W. Lin, C.-W. Kim, M. P. Limongelli, and E. Chatzi, "A comprehensive review of indirect bridge health monitoring," *Mech. Syst. Signal Process.*, vol. 247, p. 113918, Mar. 2026, doi: 10.1016/j.ymssp.2026.113918.
[23] Y. Lan, Z. Li, and W. Lin, "Physics-guided diagnosis framework for bridge health monitoring using raw vehicle accelerations," *Mech. Syst. Signal Process.*, vol. 206, p. 110899, Jan. 2024, doi: 10.1016/j.ymssp.2023.110899.
[24] Z. Li, K. Feng, A. Markou, and W. Lin, "State-of-the-art review of vibration-based bridge health monitoring using Artificial Intelligence," *ce/papers*, vol. 8, no. 5, pp. 56–65, Oct. 2025, doi: 10.1002/cepa.3377.
[25] V. M. Di Mucci, A. Cardellicchio, S. Ruggieri, A. Nettis, V. Renò, and G. Uva, "Artificial intelligence in structural health management of existing bridges," *Autom. Constr.*, vol. 167, p. 105719, Nov. 2024, doi: 10.1016/j.autcon.2024.105719.
[26] R. Niyirora, W. Ji, E. Masengesho, J. Munyaneza, F. Niyonyungu, and R. Nyirandayisabye, "Intelligent damage diagnosis in bridges using vibration-based monitoring approaches and machine learning: A systematic review," *Results Eng.*, vol. 16, p. 100761, Dec. 2022, doi: 10.1016/j.rineng.2022.100761.
[27] V. Rillo, A. De Angelis, and G. Maddaloni, "Effective structural health monitoring (SHM) system for bridges: a case study," *Procedia Struct. Integr.*, vol. 64, pp. 700–707, 2024, doi: 10.1016/j.prostr.2024.09.332.

[28] Y. Fujino, D. M. Siringoringo, T. Nagayama, and D. Su, "Proceedings of the IABSE-JSCE Joint Conference on Advances in Bridge Engineering-II, August 8-10, 2010, Dhaka, Bangladesh," in *Proceedings of the IABSE-JSCE Joint Conference on Advances in Bridge Engineering-II*, Dhaka: Bangladesh Group of IABSE, 2010, pp. 61–74.

Information about authors:
Madina Zarlykova – PhD Student, Department of Civil Engineering, L.N. Gumilyov Eurasian National University, Astana, Kazakhstan, madinazarlykova888@gmail.com
Denis Tsygulyov – Candidate of Technical Sciences, Associate Professor, Department of Civil Engineering, L.N. Gumilyov Eurasian National University, Astana, Kazakhstan, denis_riza_72@mail.ru
Murat Karacasu – Professor, Department of Architecture and Civil Engineering, Eskişehir Osmangazi University, 26480 Eskisehir, Turkey, muratk@ogu.edu.tr

Author Contributions:
Madina Zarlykova – methodology, visualization, interpretation, drafting.
Denis Tsigulyov – concept, analysis, funding acquisition.
Murat Karacasu – resources, editing.

Conflict of Interest: The authors declare no conflict of interest.

Use of Artificial Intelligence (AI): Grammarly was used to improve the language and general readability.

Received: 27.04.2026
Revised: 10.06.2026
Accepted: 15.06.2026
Published: 21.06.2026

Technobius, 2026, 6(2), 0101, DOI: https://doi.org/10.54355/tbus/27897338.6.2.2026.0101

Technobius

https://technobius.kz/

e-ISSN 2789-7338

Article

Geodetic monitoring of building deformations based on total station and GNSS measurements in the city of Kentau

Rustem Akhmetov[1], Zhanar Bimurat[1,2], Aminyam Baltiyeva[1], Gulmira Makhmetova[1,*]

[1]Rock Pressure Laboratory, D.A. Kunaev Institute of Mining, Almaty, Republic of Kazakhstan
[2]Department of Mathematical Computer Modeling, International Information Technology University, Almaty, Republic of Kazakhstan
*Correspondence: gmakhmetova@igd.com.kz

Abstract. Abstract. This study evaluates building deformation in Kentau, Kazakhstan, a post-mining urban area affected by subsidence and flooded underground workings. Two geodetic observation cycles were conducted in May and October 2025 for 14 residential and administrative buildings using GNSS-referenced total station measurements. Reflective markers installed on building corners were observed with a Leica TS10 total station, while local control networks were tied to the city GNSS framework and adjusted in a unified WGS84-based coordinate system. Inter-cycle displacements were then assessed using positional and vertical errors and compared with normative tolerance levels. Valid repeated measurements were obtained for 26 markers on 11 buildings. Approximately 85% of the markers showed planimetric displacement magnitudes below 20 mm, and about 70% showed vertical displacements within ±5 mm. Localized anomalies were recorded at individual markers, including planimetric displacement up to 74.8 mm and vertical displacement values of +616.3 mm and –122.7 mm. The three-marker analysis of building No. 10 indicated differential vertical movement between corners. The results show that GNSS-referenced total station monitoring can provide useful building-scale deformation information in post-mining urban areas, while detected outliers require marker verification, engineering inspection, and continued multi-cycle monitoring.
Keywords: geodetic monitoring, building deformation, total station survey, GNSS, mining subsidence.

1. Introduction

Kentau is a mining-affected city in southern Kazakhstan where ground and structural deformations develop as post-closure processes linked to the shutdown of underground operations and progressive flooding of mine workings. A principal geodynamic driver within the built-up area is the flooded Mirgalimsay deposit, whose galleries were repeatedly inundated from karst cavities filled with sandy-clayey material during industrial operation [1]. While an active dewatering system maintained low groundwater levels and limited geomechanical disturbance, complete dewatering shutdown on 18 October 2002 altered the hydrogeological regime, leading to rock saturation, strength reduction, and activation of post-closure deformation processes [2]. Persistent underground voids and zones of disrupted rock continuity pose continuing hazards: self-collapse may reactivate rock movement and surface subsidence, adversely affecting buildings and utilities [3]. Under such conditions, systematic deformation monitoring is an essential component of urban geodynamic assessment.

Engineering geodesy offers a well-established toolkit for structural displacement control. Terrestrial geodetic techniques, particularly electronic total station observations to discrete control points, provide object-scale three-dimensional coordinates at millimeter to centimeter precision when redundant observation schemes are applied [4], [5]. Complementary methods such as precise levelling and terrestrial laser scanning are widely used in deformation monitoring but were outside the scope

of the present campaign. Global Navigation Satellite System (GNSS) techniques deliver georeferenced time series of control points and are widely used for regional geodynamic networks and large engineering structures [6], [7], [8]. Nevertheless, GNSS building monitoring exhibits known limitations: reduced sensitivity to small vertical movements, multipath in dense urban environments, and dependence on stable monumentation [7], [9]. Interferometric Synthetic Aperture Radar (InSAR), including Persistent Scatterer and Small Baseline Subset variants, complements point-based geodesy by mapping spatially continuous ground motion; recent applications in Kazakhstan document tectonic and anthropogenic deformation around Almaty and support predictive geodynamic modelling [10], [11]. Mining subsidence literature [2], [12] further emphasizes that technogenic ground movement is spatially heterogeneous and may combine subsidence, heave, and uneven settlement, requiring multi-sensor integration rather than single-technique interpretation.

Integrated monitoring frameworks that combine GNSS, total station observations, remote sensing, and geospatial databases are increasingly proposed for technogenic landscapes, open-pit mines, and subsidence-prone urban districts [12], [13], [14]. In seismic regions of Central Asia, cyclic total station GNSS campaigns on engineering structures have been used to evaluate planimetric and vertical response under complex soil-structure interaction [5], [15]. Three-point or multi-corner marker schemes on buildings enable detection of rigid-body translation, uneven settlement, and orientation change when coordinates are adjusted in a statistically tested reference frame [5,15]. Methodology guidance for accuracy evaluation, least-squares adjustment, and comparison with normative tolerance levels is codified in engineering surveying texts and national standards for geotechnical monitoring [9], [16], [17].

Despite this broader methodological base, relatively few studies validate integrated GNSS-total station building monitoring under the specific post-mining subsidence conditions of Kentau. Regional InSAR and GNSS investigations describe ground-motion patterns at city scale [2], [10], yet building-level validation with repeatable terrestrial networks remains limited. Observation layouts proposed for generic disturbance zones are seldom tested against actual urban fabric affected by flooded workings. Existing Kentau-related work concentrates on karst hazard assessment and deposit-scale geodynamics [1], [2], but does not systematically report inter-cycle building displacements referenced to WGS84 and evaluated against published tolerance levels. Accordingly, this study addresses three gaps: 1) Operational verification of a GNSS-referenced, three-marker total station scheme on multiple buildings in an active technogenic subsidence zone; 2) Quantitative inter-cycle displacement analysis with explicit positional error and vertical error reporting after network adjustment; 3) Comparison of observed movements with tolerance levels prescribed for geotechnical monitoring [17].

The working hypothesis is that integration of GNSS control with redundant total station observations enables more reliable separation of local structural deformation from network noise than either technique applied independently. The objective is to apply this integrated geodetic approach to quantitatively evaluate planimetric and vertical inter-cycle deformations of buildings in Kentau and to interpret the results in the context of contemporary deformation-monitoring practice.

2. Materials and Methods

2.1 Study area and monitored objects

Two geodetic observation cycles were executed in May and October 2025 across the built-up area of Kentau, Kazakhstan. The monitoring program covered 14 buildings of varied functional use, predominantly low- to mid-rise residential and administrative, with masonry and reinforced-concrete structural schemes typical of the Soviet-era mining-town urban fabric (generally two to five stories, rectangular footprints, plastered or brick facade surfaces). Fieldwork was conducted by personnel of the D.A. Kunaev Institute of Mining, Almaty, Kazakhstan. Figure 1 shows the spatial distribution of monitored buildings within the city.

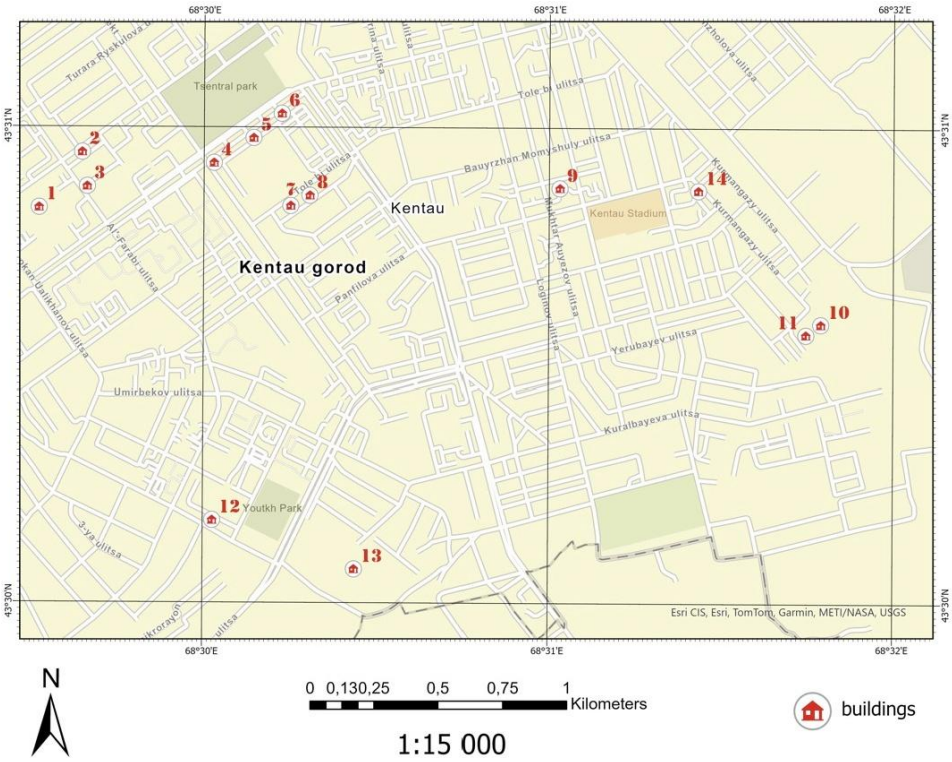

Figure 1 – Location of buildings included in the Kentau deformation monitoring program

2.2 Geodetic network design and coordinate system

An integrated methodology combining total station observations and GNSS monitoring was adopted in accordance with established deformation-monitoring practice in complex engineering-geological settings [4], [13]. Figure 2 presents the observation geodetic network deployed across the study area.

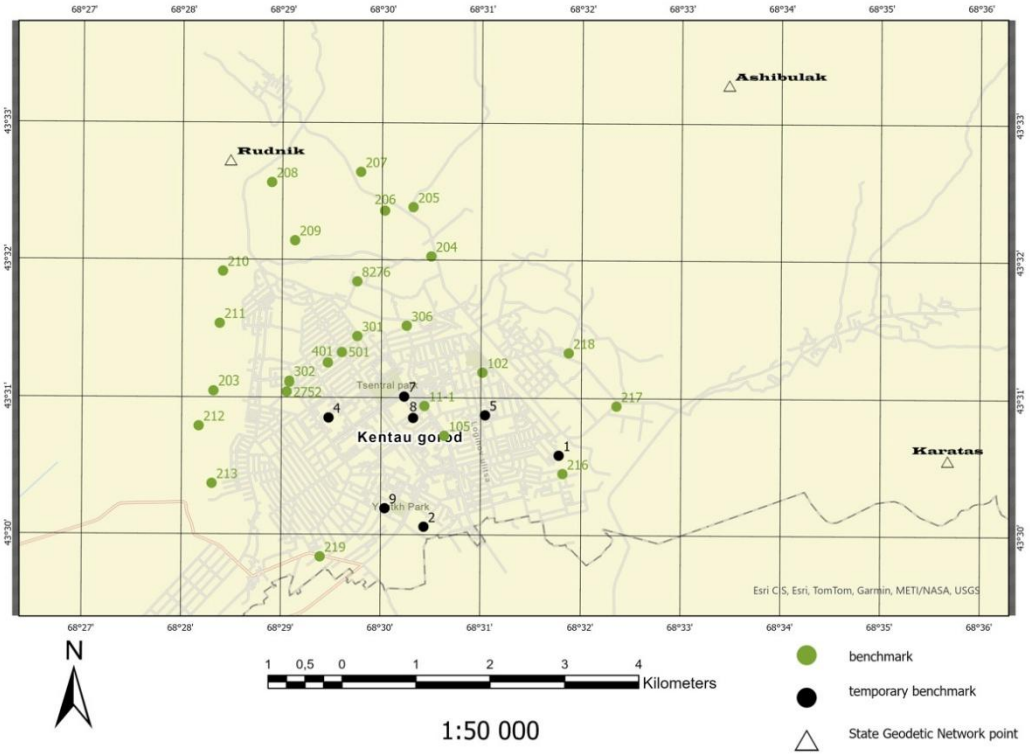

Figure 2 – Schematic of the geodetic monitoring network in Kentau, showing local total station networks, temporary benchmarks, and connection to the city GNSS framework

Near each investigated building, a local total station network with temporary benchmarks was established to ensure repeatability between cycles. The network was initially defined in a local topocentric coordinate system tied to a main instrument station established on stable open ground adjacent to the building. Coordinates of temporary benchmarks were determined from static GNSS observations using dual-frequency receivers. Session duration was not uniform across the network: at individual monitoring points, receivers operated in static mode for 2–5 h, depending on the point observed, while continuously logging carrier-phase and code data. One benchmark per building was integrated into the city GNSS network and designated as the main (reference) station for that object. This station served two functions:

1) Linking local total station vectors to a global geodetic frame;

2) Detecting potential absolute site shifts between observation cycles [6], [12].

Geodetic integration proceeded as follows. GNSS baseline solutions were computed in WGS84 (EPSG:4326 for geodetic latitude/longitude; projected processing used a local UTM-compatible metric frame consistent with the city GNSS reference). Total station observations were reduced in the local system and transformed to WGS84-compatible metric coordinates using a three-dimensional similarity transformation (translation, rotation, and scale) constrained by the GNSS-derived coordinates of the main benchmark. All total station and GNSS observations from both cycles were finally adjusted in a unified WGS84-based coordinate system so that inter-cycle coordinate differences refer to a common reference frame. Office processing, including total station network adjustment, GNSS baseline computation, coordinate transformation, and variance analysis, was performed with Leica Infinity survey software (version 4.3, Leica Geosystems AG, Heerbrugg, Switzerland).

Figure 3 illustrates a typical temporary GNSS benchmark used for network referencing.

Figure 3 – Temporary GNSS benchmark

2.3. Three-marker deformation monitoring scheme

To record building deformations, three reflective deformation markers were installed on each structure following a corner-control configuration widely applied in engineering geodesy [5], [15]. Markers were fixed directly to the load-bearing facade surfaces at building corners using adhesive mounts compatible with repeated sighting. The geometric layout was defined as follows:

– Two markers on the facade (typically the long side facing the primary instrument approach);

– One marker on an adjacent facade meeting at a corner;

– All three markers placed at upper-floor or parallel level where practicable, on externally visible wall surfaces unobstructed by vegetation, balconies, or adjacent structures.

This configuration was selected for four reasons. First, three non-collinear points minimally constrain planimetric translation, vertical displacement, and rotation in the horizontal plane. Second, corner locations maximize structural representativeness for rigid-body tilt and differential settlement. Third, the two-plus-one layout ensures that at least two markers remain visible from any single instrument station, while the third remains observable from an alternate station on the opposite side of the building. Fourth, corner-mounted markers on exterior walls provide direct line-of-sight access for the total station without interior occupancy constraints, critical for operational monitoring in inhabited urban blocks.

Figure 4 shows the marker arrangement relative to the stations and temporary benchmarks.

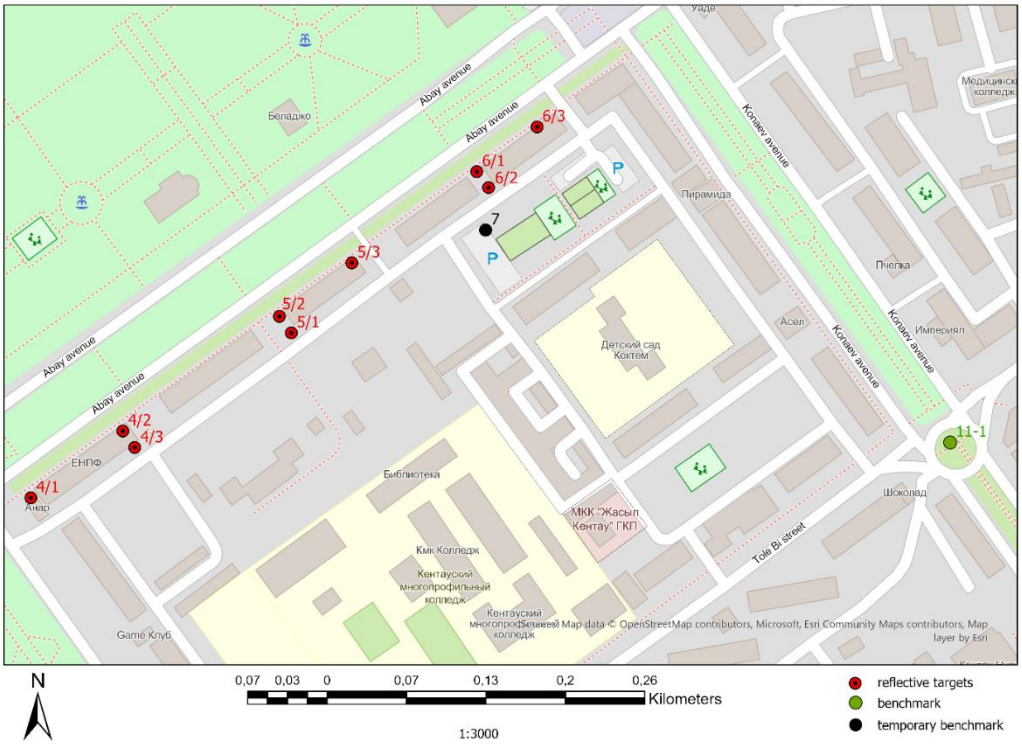

Figure 4 – Layout of three deformation markers on building corners (two markers on one facade, one on the adjacent facade), temporary benchmarks, and total stations ensuring direct line-of-sight visibility: point labels follow the field notation used in the monitoring network; designations with a slash (e.g., 4/1, 4/2, 4/3) identify reflective targets (deformation markers), whereas designations with a hyphen (e.g., 11-1) identify benchmarks

2.4. Field observation procedure

Total station observations were performed with a Leica TS10 electronic total station (angular accuracy 1″, Leica Geosystems AG, Heerbrug, Switzerland), an instrument class suitable for building deformation monitoring [5], [12]. Observations were organized sequentially from different sides of each building to guarantee visibility of all three markers:

1) The instrument was set up at the main station on the side offering clear sight lines to the two markers on the primary facade; face-left and face-right observations were completed with six rounds per marker, and mean directions and distances were computed.

2) The instrument was then moved to a secondary station on the opposite or adjacent side to observe the third marker and to provide independent check observations where geometry permitted.

3) Local benchmark points were observed in the same session to maintain network closure.

4) Observations from all stations were compared and adjusted jointly, with coordinates referred to the main (GNSS-linked) station as the primary reference for the building network.

Each marker was observed six times in both face-left and face-right positions to suppress collimation, pointing, and eccentricity errors [5], [18]. The three-marker geometry enabled detection of planimetric shifts, vertical displacements, and changes in building orientation between cycles [5].

2.5. Data processing, accuracy assessment, and tolerance levels

After least-squares adjustment of the combined total station and GNSS network, the accuracy of each deformation marker was evaluated using standard error-propagation expressions [9], [15], [16].

The horizontal positional error was computed as:

$$S_{xy} = \sqrt{S_x^2 + S_y^2}, \quad (1)$$

where: S_x and S_y are the standard deviations (root mean square errors or RMSE) of the adjusted planimetric coordinates of the marker [9], [15].

The vertical error was computed as:

$$S_h = \sqrt{D_h}, \quad (2)$$

where: D_h is the variance of the adjusted elevation obtained from the least-squares adjustment [16].

Eqs. (1) and (2) express the propagation of adjusted coordinate uncertainties for uncorrelated horizontal components and the height component, respectively, and are standard metrics in geodetic monitoring quality reporting [9], [15].

Inter-cycle displacements between observation cycles i and $i - 1$ were calculated as coordinate differences:

$$\Delta X = X_i - X_{i-1}, \Delta Y = Y_i - Y_{i-1}, \Delta H = H_i - H_{i-1}, \quad (3)$$

where: X_i, Y_i, H_i, and X_{i-1}, Y_{i-1}, H_{i-1} are the adjusted coordinates of the marker in the current and previous cycles [15], [18].

The resultant planimetric displacements magnitude was obtained as:

$$\Delta S_{xy} = \sqrt{(\Delta X)^2 + (\Delta Y)^2}, \quad (4)$$

where: ΔX and ΔY are the planimetric coordinate increments between consecutive cycles [18].

Deformation significance was assessed by comparing inter-cycle displacements ΔX, ΔY, ΔH, and ΔS_{xy} with tolerance levels prescribed for geotechnical monitoring of buildings and structures. In this study, the comparative normative framework was [17], which defines allowable displacement increments and monitoring accuracy requirements for building safety control [17]. For each marker, measured displacements were evaluated against the corresponding tolerance levels tabulated in [17] for planimetric and vertical displacement control, accounting for building category and observation stage. Displacements exceeding both the adjusted "positional error" or "vertical error" (Eqs. (1) and (2)) and the normative tolerance level were flagged for detailed engineering review. Terminology is applied consistently throughout: positional error and vertical error describe coordinate precision after adjustment; tolerance level denotes the normative allowable displacement threshold; displacement and distribution refer to inter-cycle movement statistics across the marker population.

3. Results

Processed total station and GNSS observations yielded planimetric and vertical displacements for all surveyed buildings. For most markers, horizontal positional error remained within approximately 10–20 mm, whereas vertical error was on the order of a few millimeters, supporting reliable detection of vertical movement at the building scale.

Figures 6 and 7 present the distribution of inter-cycle displacements for all deformation markers with valid May–October 2025 comparisons across the monitored building stock (n = 26 markers on 11 buildings; the remaining markers could not be reoccupied in October 2025). These diagrams aggregate every successfully measured marker, not a single building subset. Figures 5 and 6 depict the displacement magnitudes ΔS_{xy} and ΔH, as given by Eqs. (3) and (4).

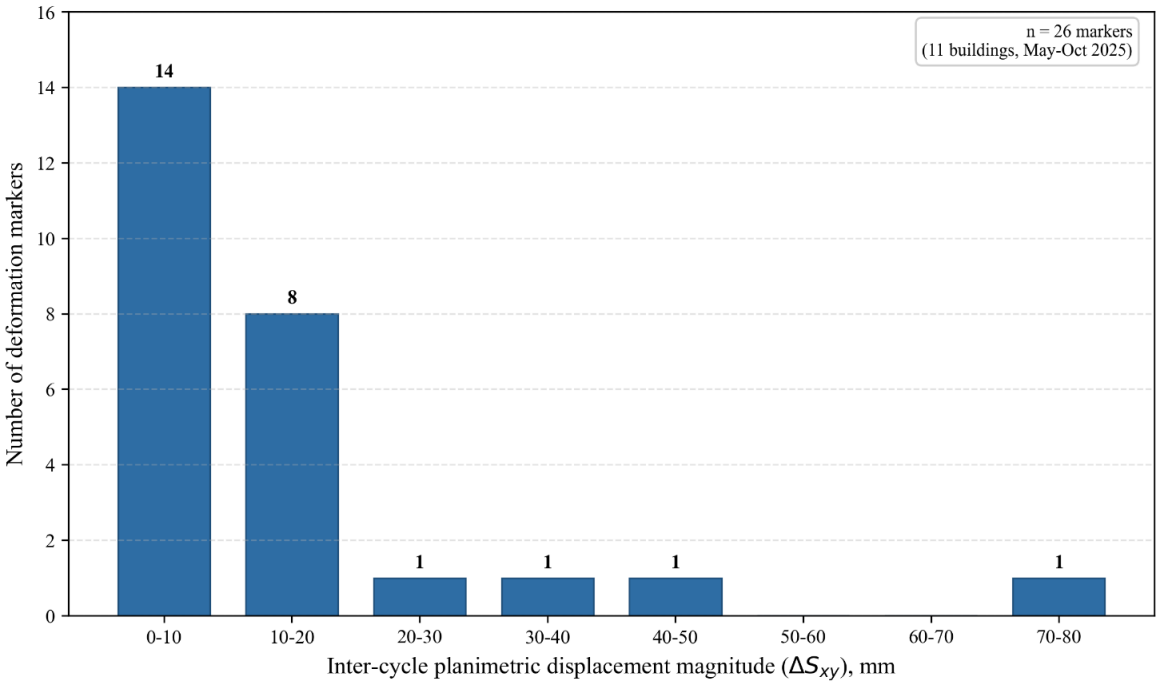

Figure 5 – Distribution of inter-cycle planimetric displacement magnitude ΔS_{xy}

As shown in Figure 5, the distribution of ΔS_{xy} is strongly skewed toward small values: approximately 85% of all monitored markers exhibited planimetric displacement magnitudes below 20 mm. Notable outliers include marker 1/2 (ΔS_{xy} = 74.8 mm) and 2/1 (ΔS_{xy} = 40.3 mm).

Figure 6 presents the corresponding distribution of vertical displacement ΔH. Roughly 70% of markers fall within the ±5 mm range, indicating predominantly stable vertical behavior at the network scale. The distribution is strongly influenced by extreme values at individual corners, including ΔH = 616.3 mm at marker 2/3 and ΔH = –122.7 mm at marker 10/2.

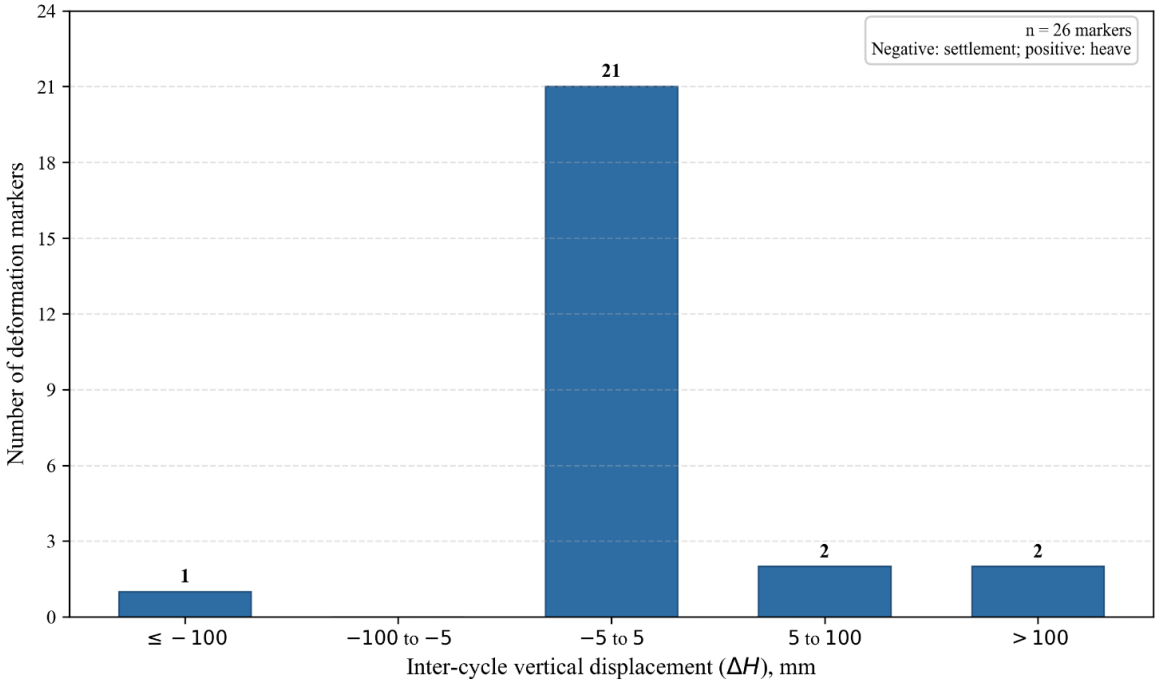

Figure 6 – Distribution of inter-cycle vertical displacement ΔH

The largest structurally interpretable vertical contrast was recorded at three markers on point 10, with inter-cycle displacements shown in Table 1.

Table 1 – Inter-cycle displacements of deformation markers on building No. 10

Marker	Displacement, mm		
	ΔX	ΔY	ΔH
10/1	–8.8	–4.7	131.3
10/2	–8.1	–5.2	–122.7
10/3	4.2	11.9	2.2

Figure 7 presents the temporal evolution of elevation changes for the three markers between May and October 2025.

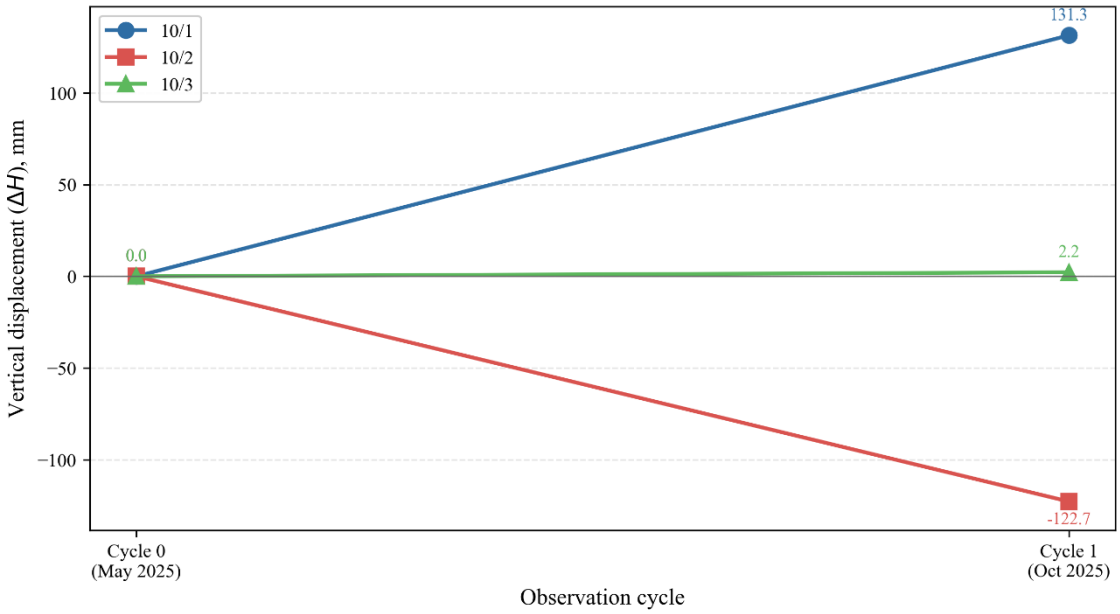

Figure 7 – Temporal development of vertical displacement at deformation marker 10

For the other monitored buildings, consolidated inter-cycle values are presented in Table 2 on a selective basis, retaining only markers with significant displacement amplitudes and excluding cases of negligible, geometrically similar movement.

Table 2 – Selected significant vertical displacements of deformation markers in Kentau

Marker	Displacement ΔH, mm
1/2	6.0
2/1	5.5
2/3	616.3

During the October 2025 cycle, repeated measurements could not be completed at several objects because temporary benchmarks or deformation markers were lost or damaged, reducing the number of directly comparable records from the nominal 42 markers (14 buildings × 3) to 26.

4. Discussion

4.1. Interpretation of network-scale behavior

The aggregated displacement distributions (Figures 5 and 6) indicate that most markers on most buildings remained stable between May and October 2025. Approximately 85% of all valid marker records exhibited $\Delta S_{xy} < 20$ mm, and roughly 70% showed $|\Delta H| \leq 5$ mm. This pattern is consistent with slow, spatially differentiated technogenic deformation rather than city-wide catastrophic movement – a finding aligned with regional InSAR and GNSS studies reporting heterogeneous subsidence and local uplift pockets in Kentau rather than uniform basin-scale settlement [2], [10].

The extreme vertical outlier at marker 2/3 ΔH = 616.3 mm and the large opposing vertical components at markers 10/1 and 10/2 requires cautious interpretation. Values of this magnitude within a five-month window exceed typical elastic building response and likely reflect local foundation disturbance, possible marker instability, or unresolved datum effects at individual corners rather than uniform building subsidence alone. Such outliers underscore the value of the three-marker scheme: single-point monitoring would mischaracterize structural behavior, whereas corner arrays expose differential patterns indicative of tilting or local ground failure [5], [15].

For the majority of markers where $|\Delta H|$ remained within a few millimeters and ΔS_{xy} below 20 mm, displacements were comparable to or smaller than normative tolerance levels in [17] when applied to operational monitoring of existing structures [17]. Where displacements exceeded tolerance levels, notably at selected markers at points 2 and 10, engineering follow-up, including inspection, marker verification, and densification of observations, is warranted.

4.2. Comparison with previous studies

Relative to GNSS-dominated high-rise monitoring in seismically active cities [7], [8], the present work emphasizes terrestrial corner control better suited to low- to mid-rise masonry buildings where rooftop GNSS mounting is impractical, and multipath is severe. Compared with InSAR-only regional assessments [10,11], the total station network provides building-resolved, three-dimensional corner displacements at monthly-to-seasonal cadence, albeit at sparse spatial density. This complementarity mirrors integrated frameworks proposed for technogenic objects combining InSAR reconnaissance with total station and GNSS control benchmarks [12], [13].

[6] demonstrated combined GNSS and total station monitoring of engineering structures in seismic regions of Kazakhstan, reporting millimeter-scale accuracy for stable objects, consistent with our adjusted positional error (approximately 10–20 mm at the 95% confidence level for planimetric components) and vertical error (a few millimeters). [5] showed that redundant face measurements and corner marker geometry improve detection of subtle tilting in heritage structures; the six-round face-left/face-right procedure adopted here follows the same principle. [15] emphasize that deformation interpretation must follow formal network adjustment and variance testing; our explicit use of Eqs. (1) and (2) before the displacement analysis adheres to that recommendation.

4.3. Methodological strengths and limitations

The methodological strengths of the study include reproducible three-marker geometry with a documented line-of-sight strategy, GNSS anchoring of each local network in WGS84, redundant total station observations, and explicit comparison with normative tolerance levels [17].

At the same time, the study has several limitations. Only two observation cycles were conducted over five months, which is insufficient to resolve long-term velocity or seasonal effects. In addition, the loss of 16 markers and several benchmarks in October 2025 introduced selection bias in the aggregated distributions. Another limitation is the absence of concurrent InSAR extraction at building corners, which limited regional corroboration of local outliers. Possible conflation of ground and structural components without subsurface profiling at outlier locations should also be considered [1], [2].

Future work should extend the time series over multiple years, integrate Sentinel-1 InSAR velocities with corner displacements, implement automated statistical testing between epochs, including variance-ratio and global congruency tests [15], and replace temporary dowel benchmarks with forced-centering monuments where long-term monitoring is approved [10].

5. Conclusions

1. An integrated geodetic monitoring workflow combining GNSS-referenced total station networks, three-marker corner control, and least-squares adjustment in a unified WGS84-based

coordinate system was implemented for building deformation monitoring in the mining-affected city of Kentau, Republic of Kazakhstan.

2. The May–October 2025 inter-cycle comparison showed predominantly stable behavior for the valid marker set. Approximately 85% of the markers had planimetric displacement magnitudes below 20 mm, while about 70% showed vertical displacements within ±5 mm. This indicates that most monitored buildings did not demonstrate large inter-cycle movements during the observation period.

3. Localized anomalies were detected at individual markers, including planimetric displacement up to 74.8 mm and vertical displacement values reaching 616.3 mm and –122.7 mm. The three-marker analysis of building No. 10 showed differential vertical movement between corners, indicating the need for detailed engineering inspection, marker verification, and continued monitoring of outlier locations.

4. The results confirm that GNSS-referenced total station monitoring can provide useful building-scale deformation information in post-mining urban areas. However, because the study was based on only two observation cycles and part of the original marker network was lost, further multi-cycle monitoring with more durable benchmarks is required to confirm long-term deformation trends and support reliable risk assessment.

Acknowledgments

This research is funded by the Committee of Industry of the Ministry of Industry and Construction of the Republic of Kazakhstan under program-targeted funding for scientific research for 2024–2026, BR23991563: “Creation of Innovative Resource-Saving Technologies for Mining and Integrated Processing of Mineral and Technogenic Raw Materials”.

References

[1] A. Baltiyeva, E. Orynbassarova, Z. Bimurat, and G. Makhmetova, “Comprehensive ground-space monitoring of geodynamic processes at the Mirgalimsay deposit,” in *Proceedings of the 25th SGEM International Multidisciplinary Scientific GeoConference 2025*, Albena, Bulgaria: SGEM, 2025, pp. 127–136. doi: 10.5593/sgem2025/2.1/s09.16.

[2] E. V. Drobinina, S. V. Shcherbakov, D. R. Zolotarev, O. N. Kovin, G. V. Fedorov, and D. A. Inkin, “Assessment of karst hazards within the orogen territories using geophysical methods (on the example of Kentau city and surroundings, Kazakhstan),” *News of the Ural State Mining University*, vol. 65, no. 1, pp. 28–45, 2022, doi: 10.21440/2307-2091-2022-1-28-45.

[3] A. Behera and K. Singh Rawat, “A brief review paper on mining subsidence and its geo-environmental impact,” *Materials Today: Proceedings*, p. S2214785323020795, 2023, doi: 10.1016/j.matpr.2023.04.183.

[4] I. S. Gribkova, R. O. Kuzmin, L. A. Shchenyavskaya, and A. A. Panyutishcheva, “Modern methods and devices of geodetic monitoring of buildings and structures,” *Science. Engineering. Technology (polytechnical bulletin)*, no. 2, pp. 44–47, 2023.

[5] Z. M. Pawlak, I. Wyczałek, and P. Marciniak, “Two Complementary Approaches toward Geodetic Monitoring of a Historic Wooden Church to Inspect Its Static and Dynamic Behavior,” *Sensors*, vol. 23, no. 20, p. 8392, 2023, doi: 10.3390/s23208392.

[6] D. Kirgizbayeva, M. Nurpeisova, K. Menayakov, T. Nurpeisova, and A. Umirbayeva, “Monitoring deformations of engineering structures in seismic regions,” *Bulletin of Kazakh Leading Academy of Architecture and Construction*, vol. 96, no. 2, pp. 87–97, 2025, doi: 10.51488/1680-080X/2025.2-09.

[7] D. Paudel, B. Sherchan, and K. P. Bhandari, “A General Review on Application of GNSS for Structural Deformation Monitoring,” in *Proceedings of 12th IOE Graduate Conference*, Kathmandu, Nepal: Tribhuvan University, 2022, pp. 188–196.

[8] B. B. Imansakipova, Zh. D. Baygurin, and N. B. Imansakipova, “Geodetic observations of high-rise buildings and structures in seismically hazadous areas,” *KazNU Bulletin. Geography series*, vol. 38, no. 1, pp. 44–47, 2014.

[9] C. D. Ghilani and P. R. Wolf, *Elementary surveying: an introduction to geomatics*, 13th ed. Upper Saddle River, N.J: Pearson Prentice Hall, 2012.

[10] E. Bayramov, N. Sydyk, S. Nurakynov, A. Yelisseyeva, J. Neafie, and S. Aliyeva, “Advanced Spaceborne InSAR for monitoring tectonic and anthropogenic ground deformation in the seismically sensitive Almaty region, Kazakhstan,” *Advances in Space Research*, vol. 77, no. 1, pp. 118–146, 2026, doi: 10.1016/j.asr.2025.11.083.

[11] M. Crosetto, O. Monserrat, M. Cuevas-González, N. Devanthéry, and B. Crippa, "Persistent Scatterer Interferometry: A review," *ISPRS Journal of Photogrammetry and Remote Sensing*, vol. 115, pp. 78–89, 2016, doi: 10.1016/j.isprsjprs.2015.10.011.
[12] V. V. Kazantseva, D. S. Ozhigin, N. Kosarev, A. K. Satbergenova, and S. B. Ozhigina, "Development of complex system of geotechnical monitoring of technogenic objects based on geospatial data," *Journal of Mining Institute*, vol. 276, no. 1, pp. 142–156, 2025.
[13] M. M. Abdukarimov, "Analiz zarubezhnogo opyta geodezicheskogo monitoringa deformatsiy gidrotekhnicheskikh sooruzheniy," vol. 5, no. 2, pp. 18–25, 2026, doi: 10.5281/ZENODO.18231593.
[14] A. Ferretti, A. Monti-Guarnieri, C. Prati, F. Rocca, and D. Massonnet, *InSAR principles: guidelines for SAR interferometry processing and interpretation*. in ESA TM, no. 19. Noordwijk, the Netherlands: ESA Publications, ESTEC, 2007.
[15] M. G. Mustafin, A. V. Zubov, and G. E. Vasiljev, "Deformation estimation procedure for monitoring engineering facilities," *MIAB*, vol. 8, 2025, doi: 10.25018/0236_1493_2025_8_0_92.
[16] C. D. Ghilani and P. R. Wolf, *Adjustment computations: spatial data analysis*, 4th ed. Hoboken, N.J: John Wiley & Sons, 2006.
[17] "SP 305.1325800.2017 Buildings and structures. The rules of geotechnical monitoring under construction," Moscow, Russia: Standardinform, 2017, p. 57.
[18] V. V. Simonian, A. V. Labuznov, N. V. Angelova, and M. S. Savin, "The comparative analysis of methods of range measurements to asses the applicability of these methods for geodetic monitoring of extended objects," *International scientific, technical and industrial electronic journal «Geo Science»*, no. 3–4, pp. 22–30, 2011.

Information about authors:
Rustem Akhmetov – Junior Researcher, Rock Pressure Laboratory, D.A. Kunaev Institute of Mining, Almaty, Republic of Kazakhstan, rakhmetov@igd.com.kz
Zhanar Bimurat – PhD; 1) Leading Researcher, Rock Pressure Laboratory, D. A. Kunaev Institute of Mining, Almaty, Republic of Kazakhstan; 2) Assistant Professor, Department of Mathematical Computer Modeling, International Information Technology University, Almaty, Republic of Kazakhstan, zhbimurat@igd.com.kz
Aminyam Baltiyeva – Leading Researcher, Rock Pressure Laboratory, D.A. Kunaev Institute of Mining, Almaty, Republic of Kazakhstan, geomine.lab@igd.com.kz
Gulmira Makhmetova – Junior Researcher, Rock Pressure Laboratory, D.A. Kunaev Institute of Mining, Almaty, Republic of Kazakhstan, gmakhmetova@igd.com.kz

Author Contributions:
Rustem Akhmetov – methodology, resources, testing, data collection, analysis.
Zhanar Bimurat – drafting, editing.
Aminyam Baltiyeva – data collection, drafting, editing.
Gulmira Makhmetova – analysis, interpretation, concept.

Conflict of Interest: The authors declare no conflict of interest.

Use of Artificial Intelligence (AI): AI assistance was applied to improve language clarity.

Received: 04.03.2026
Revised: 08.06.2026
Accepted: 17.06.2026
Published: 22.06.2026

Technobius, 2026, 6(2), 0102, DOI: https://doi.org/10.54355/tbus/27897338.6.2.2026.0102

Technobius
https://technobius.kz/

e-ISSN
2789-7338

Article

Mechanical responses of Ili saline loess to EICP treatment under variable salinity and freeze-thaw conditions

Kaixin Shi[1,2], Li Ma[1,2,*], Xuejun Liu[3]

[1]College of Civil Engineering and Architecture, Xinjiang University, Urumqi, China
[2]Xinjiang Key Laboratory of Building Structure and Earthquake Resistance, Xinjiang University, Urumqi, China
[3]Xinjiang Institute of Building Science Co., Ltd, Urumqi, China
*Correspondence: mali@xju.edu.cn

Abstract. This study evaluated the effectiveness of the enzyme-induced carbonate precipitation (EICP) method in improving the mechanical properties of saline loess from Northwest China under different salinity and freeze-thaw conditions. Four different Na_2SO_4 concentrations (0.16%−3.16%) were used to simulate varying degrees of salinization in the Ili loess, and consolidation tests, unconfined compressive strength tests, and freeze-thaw cycle tests were conducted on both treated and untreated specimens. The results show that in consolidation tests, the effect of EICP treatment on the compressibility of saline loess is significantly modulated by salinity – under low-salinity conditions (≤1.16%), the compression index C_c decreased by up to 19.8%; however, under high-salinity conditions (≥2.16%), C_c actually increased by approximately 17%, indicating a reversal of the cementation effect. Unconfined compressive strength tests and freeze-thaw cycle tests showed that, under low salinity conditions, EICP can effectively enhance particle cementation, increasing strength by 15%−39% and improving freeze-thaw resistance. Under high salinity conditions, however, particularly after undergoing six freeze-thaw cycles, calcium carbonate cementation significantly deteriorated, and the strength of treated specimens was lower than that of untreated specimens. The failure mode gradually evolved from end shear and single shear planes to distributed cracking as the number of freeze-thaw cycles increased, ultimately progressing to complete disintegration. In summary, EICP holds engineering potential for reinforcing loess under low salinity conditions; however, in coupled saline-alkali and cold regions, its applicability requires optimized design based on salinity and freeze-thaw conditions.

Keywords: EICP, saline loess, compression characteristics, freezing-thaw cycles.

1. Introduction

Before the term loess was formally introduced and adopted within the geological community, this distinctive sediment was referred to as “Löß” or “Löss” by residents of Heidelberg, Germany, and as “Lehm” by inhabitants of Alsace, France. The term loess first appeared in a formal scientific context in 1824, in Section 89 of Volume III of Charakteristik der Felsarten, authored by the renowned mineralogist Professor Leonhard of the University of Heidelberg [1]. Predominantly composed of silt-sized particles, loess is characterized by a loose fabric, high porosity, and well-developed vertical jointing [2].

Loess deposits, formed primarily during the Quaternary Pleistocene [3], accumulated progressively through aeolian processes under alternating glacial-interglacial climatic conditions. They are widely distributed across Eurasia and parts of the Americas, covering approximately one-tenth of the Earth’s terrestrial surface [4], [5]. As a representative structured unsaturated soil, loess exhibits distinctive engineering properties, including collapsibility, underconsolidation, and pronounced sensitivity to dynamic loading [6], [7]. Under external influences such as rainfall infiltration, snowmelt recharge, and anthropogenic disturbances, its metastable structure is prone to degradation and collapse, potentially triggering geohazards including landslides, ground collapse, and foundation

settlement. In recent years, climate warming has intensified the frequency and magnitude of extreme rainfall and snowmelt events. Coupled with increasing disturbances from urbanization and infrastructure development, loess-related hazards (Figure 1) have shown clear trends toward higher frequency, abrupt initiation, and repeated occurrence, posing significant challenges to regional safety and risk management.

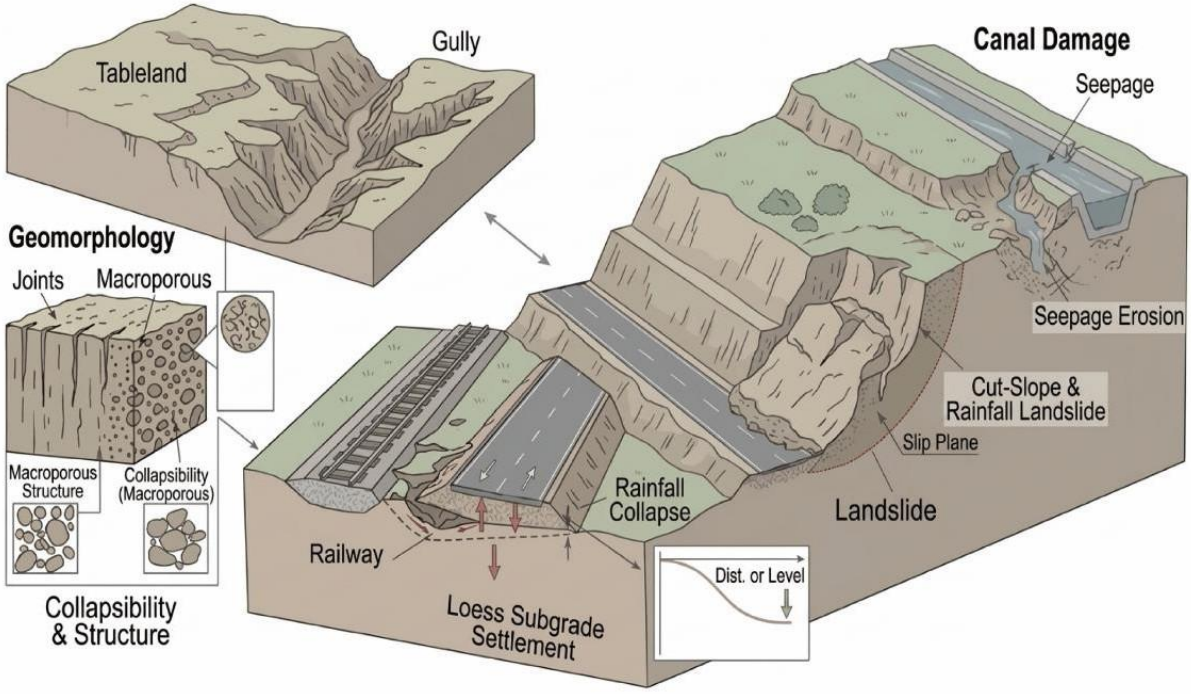

Figure 1 – Typical loess hazards

The Ili Valley in Xinjiang and the Central Asian loess belt are typical sensitive loess regions. In 2017, the Piliqing River landslide evolved into a landslide–damming breach–debris flow disaster chain [8] under the combined effects of prolonged river erosion and freeze-thaw action, while subsequent monitoring showed that the landslide remained in an active deformation state. In 2019, reactivation of a high-position loess landslide in the Zeketai River basin triggered repeated creep movements, forming a ~30 m thick sliding mass that endangers both transportation routes and river safety [9]. Moreover, highway slopes and oil/gas pipelines in Central Asia frequently suffer from shallow slumping and differential settlement under the dual actions of rainfall and collapsibility [10]. The cases presented above reveal that loess disasters are characterized by both marked regional clustering and notable trans-regional commonality. Hence, a systematic investigation of their formation mechanisms and the development of validated prevention-control technologies are of urgent practical importance.

For loess improvement techniques, traditional stabilization methods using cement and lime can enhance strength; however, they are associated with high carbon emissions, significant ecological disturbance, and uncertain long-term durability [11]. In recent years, enzyme-induced carbonate precipitation (EICP), a biochemical coupled ground improvement technique, has attracted increasing attention. This method relies on urease-catalyzed hydrolysis of urea to generate carbonate ions, which subsequently react with calcium ions to precipitate calcium carbonate (Figure 2). The precipitates form microscale cementation bonds between soil particles [12], promoting pore filling and interparticle bridging, thereby reducing the permeability of porous soil media [12], enhancing shear strength, and mitigating collapsibility. Existing studies have demonstrated that EICP can significantly improve the mechanical properties and erosion resistance of sandy soils and some silty soils. Its effectiveness is governed by factors such as solution concentration, enzyme activity, injection strategy, and curing conditions.

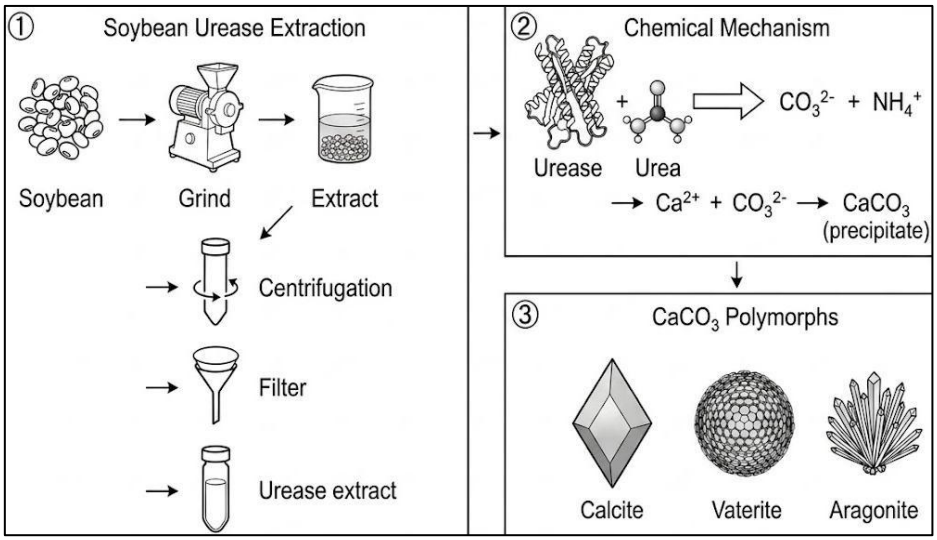

Figure 2 – EICP enzyme extraction procedure and its biomineralization mechanism

However, for the eastern margin of the Central Asian loess belt, particularly the Ili Valley in Xinjiang, where loess genesis is complex, silt content is high, and hydrothermal conditions are distinctive, the mechanisms and engineering applicability of EICP remain insufficiently understood. Specifically: (i) the effects of ion composition and concentration in saline environments on urease activity and calcium carbonate crystallization are not yet well clarified; and (ii) the stability and durability of the cemented soil under coupled multi-physics processes, such as freeze-thaw cycles and wetting-drying cycles, lack systematic evaluation. These limitations constrain the broader application of EICP in loess regions.

Accordingly, this study focuses on loess from the Ili Valley in Xinjiang, investigating the EICP-induced stabilization mechanisms and the mechanical behavior of sulfate-rich saline loess treated with EICP. The findings are expected to provide theoretical support for green bio-mediated improvement of loess and to offer practical guidance for geohazard mitigation and engineering design in northwestern China and other regions with similar geological conditions.

2. Methods

The loess samples used in the experiment were collected from the surface layer (depth of 1−2 m) of a slope in the Hursai loess landslide area of the 61st Regiment, 4th Division, Xinjiang Uygur Autonomous Region, China. The soil is yellowish-brown with sparse fine plant roots. Basic physico-chemical properties were determined following the Chinese standard GB/T 50123-2019 Standard for Geotechnical Testing Method. Mechanical sieving was conducted using standard geotechnical sieves, and laser diffraction analysis was performed using a laser particle size analyzer, Microtrac, USA. The resulting grading curve showed that the grain size distribution spanned a wide range, but the mass was concentrated in the silt fraction 10−100 μm, with low proportions of fine and coarse particles. The gradation exhibits good continuity, yet the dominant particle group (silt) is prominent. The tested loess sample exhibits a specific gravity of 2.7 and a low initial salinity of 0.16%. Its Atterberg limits are characterized by a liquid limit of 27.7% and a plastic limit of 16.5%, resulting in a plasticity index of 11.2, which classifies the soil as a low-plasticity silty clay. The compaction characteristics indicate an optimum moisture content of 16.64% and a maximum dry density of 1.67 g/cm^3.

The soil samples were air-dried, pulverized, oven-dried, and sieved through a 2.0-mm mesh before testing. Given the prevalence of chloride-sulfate saline soils in Northwest China, characterized by distinct sulfate transformation behaviors and a dominance of sodium cations, and referencing the standard definition of saline soil (salt content > 0.3%), four specific salinity levels were selected for this study: 0.16% (control), 1.16%, 2.16%, and 3.16%.

First, mix the oven-dried soil evenly with the calculated amount of salt to achieve the target salinity level.

The soybean urease solution is prepared as follows: Mix 20 grams of soybean flour with 1 liter of deionized water and stir for 15 minutes at 25 °C. Then refrigerate the mixture for 24 hours. After refrigeration, filter the suspension through a 500-mesh gauze, then centrifuge at 4,000 rpm for 15 minutes. Collect the resulting supernatant as the soybean urease solution. Determine urease activity using the conductivity method.

To prepare the binding solution, urea and calcium chloride were dissolved in deionized water, with both set at a concentration of 0.5 mol/L. Before sample preparation, the soybean urease solution was mixed with the binding solution at a 2:3 volume ratio to produce the EICP treatment solution.

Subsequently, under continuous stirring, the EICP treatment solution was gradually added to the saline loess until the optimal moisture content of 16.64% was reached, ensuring uniform mixing. The prepared soil samples were then statically compacted into cylindrical specimens with a diameter of 50 mm and a height of 100 mm (Figure 3). After preparation, each specimen was sealed with plastic film and cured at 25 °C for 72 h.

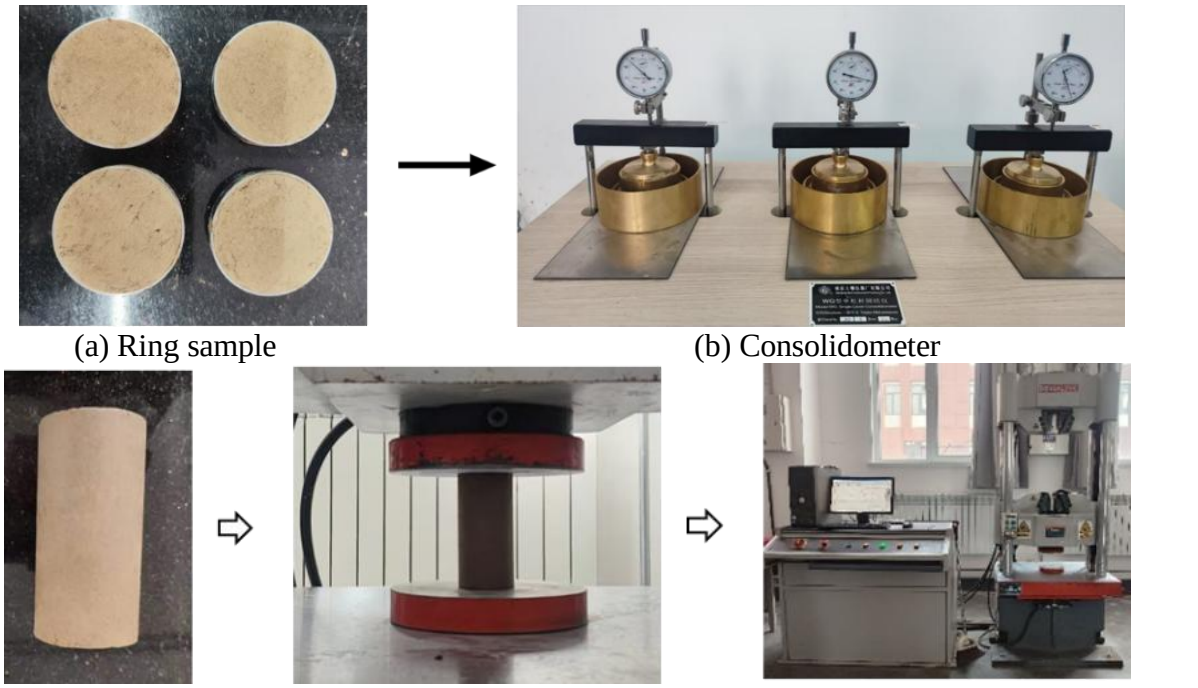

(a) Ring sample (b) Consolidometer

(c) Cylinder sample (d) Loading (e) Universal Testing Machine system

Figure 3 – Specimen preparation and testing setup

Consolidation tests were conducted using a WG-type single-lever consolidometer (Nanjing Soil Instrument Co., Ltd., Nanjing, China) following the standard consolidation test method. Each load increment was maintained until the hourly deformation was less than 0.01 mm before the next load was applied. The loading sequence comprised six vertical pressures: 1, 12.5, 50, 100, 200, and 800 kPa. The tests were performed on both untreated saline loess and EICP-treated saline loess with salt contents of 0.16%, 1.16%, 2.16%, and 3.16%. The target salinity levels were achieved by thoroughly mixing the oven-dried soil with predetermined amounts of analytical-grade sodium sulfate (Na_2SO_4).

Unconfined compressive strength tests were conducted on soil specimens using a universal testing machine with a shear rate of 1 mm/min. The test was terminated when the axial strain continued to increase by 5% after reaching the peak stress. To investigate the freeze-thaw effect on the Ili loess, the freezing temperature was set to −20°C and the thawing temperature to 20°C, with a duration of 12 h for both freezing and thawing, resulting in a 24-h freeze-thaw cycle. The number of freeze-thaw cycles applied to the specimens was 3, 6, and 9, respectively, with 0 cycles serving as the control. After completing the designated freeze-thaw cycles, the specimens were subjected to

unconfined compressive strength tests.

3. Results and Discussion

3.1 Compression tests

From the e-p compression curves of loess with different salt contents in Figure 4, the void ratio of all specimens decreased monotonically as the consolidation pressure increased from 1kPa to 800 kPa. Under the same salt content, the compression curves of the EICP-treated group generally lie above those of the untreated group for most of the loading range, with the most notable difference occurring in the pressure range of 50−200 kPa.

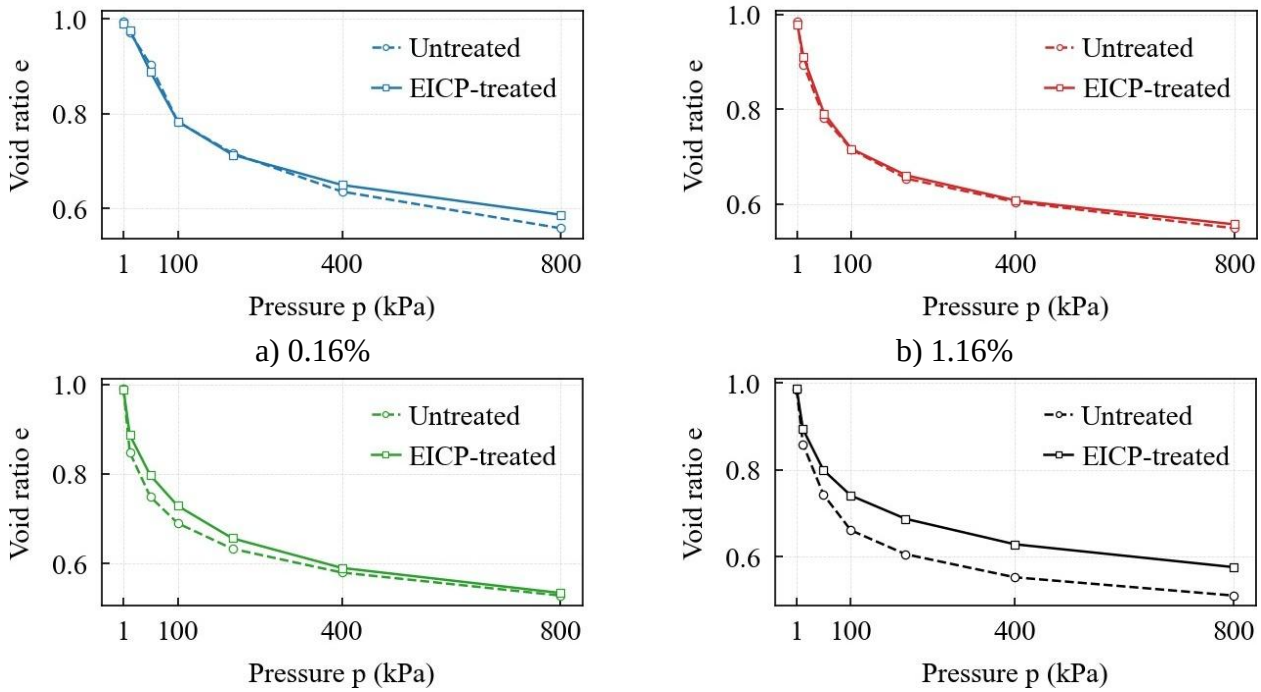

Figure 4 – Compression curves of loess before and after EICP treatment under different salt contents

At the lowest salt content (0.16%), however, the two curves cross near 200 kPa, where the EICP-treated soil shows a slightly lower void ratio than the untreated soil. This observation suggests that the beneficial effect of EICP treatment on compressive deformation resistance may be less pronounced under very low salt conditions, possibly due to insufficient calcium carbonate precipitation or weaker cementation. Nevertheless, for salt contents of 1.16% and above, the EICP-treated curves remain consistently above the untreated curves over the entire pressure range, indicating effective improvement. Regarding the effect of salt content, for untreated loess, the compression curves shift progressively downward as the salt content increases, implying a salt-induced reduction in compressibility. For EICP-treated loess, the trend is not strictly monotonic: the void ratio decreases from 0.16% to 1.16% but increases again at 2.16% and 3.16%. This behavior may result from the dual role of salt, which moderately enhances cementation at low concentrations while potentially inhibiting urease activity or altering crystal morphology at higher concentrations. Previous SEM and XRD analyses of EICP-treated saline soils have shown that $CaCO_3$ precipitates are dominated by vaterite, with minor calcite, and that high-salinity, ion-rich environments can distort vaterite morphology from well-defined spherical forms to disc-like or flake-like crystals. Such morphological distortion reduces the effectiveness of pore filling and interparticle cementation, thereby contributing to strength loss [13].

All compressibility parameters were determined in accordance with the relevant standards.

Specifically, the pre-consolidation pressure (P_c) was computed using a cubic spline curvature maximization technique, which numerically replicates the graphical Casagrande procedure. The remaining parameters were then calculated from Eqs. (1-3), as specified in standards [14] and [15].

$$a_{1-2} = \frac{e_{100} - e_{200}}{200 - 100}, \quad (1)$$

$$E_s = \frac{1 + e_{100}}{a_{1-2}}, \quad (2)$$

$$C_c = \frac{e_{200} - e_{800}}{log_{10}(800) - log_{10}(200)}, \quad (3)$$

where: $a_{1\text{-}2}$ is a coefficient of compressibility; e_{100}, e_{200}, e_{800} are void ratios at 100 kPa, 200 kPa and 800kPa obtained by linear interpolation, respectively; E_s – constrained modulus of deformation (oedometer modulus); C_c – compression index.

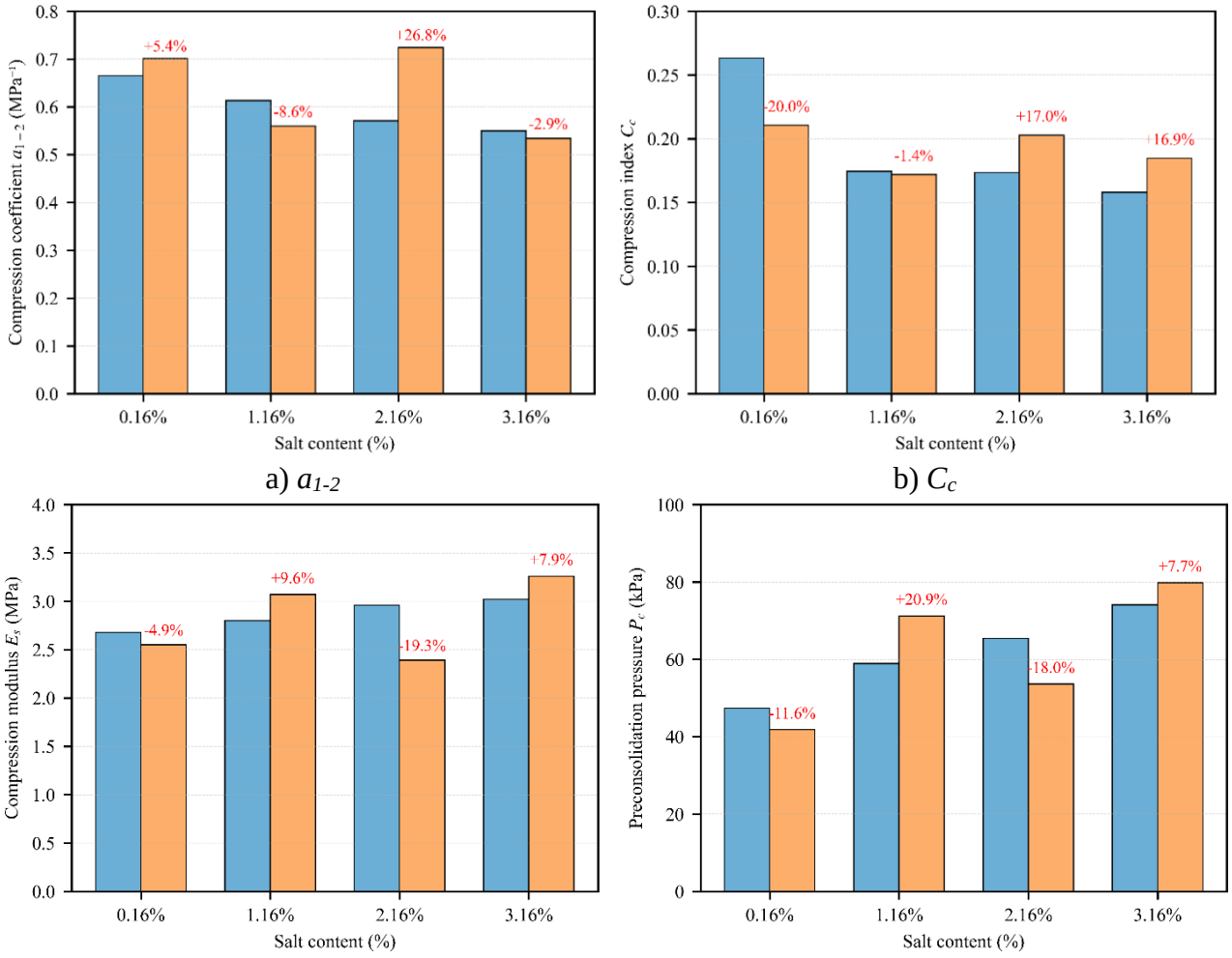

a) $a_{1\text{-}2}$ b) C_c

c) E_s d) P_c

Figure 5 – Compression parameters of untreated and EICP-treated saline loess

Figure 5(a) shows the variation of the compressibility coefficient $a_{1\text{-}2}$ (100-200 kPa) with salt content. For untreated loess, $a_{1\text{-}2}$ decreases gradually from 0.665 MPa^{-1} at 0.16% salt to 0.550 MPa^{-1} at 3.16% salt, indicating that higher salt loading reduces low- to medium-pressure compressibility. After EICP treatment, the effect becomes non-monotonic: at 0.16% salt, $a_{1\text{-}2}$ increases slightly from 0.665 to 0.701 MPa^{-1} (+5.4%); at 1.16% salt, it decreases from 0.613 to 0.560 MPa^{-1} (−8.6%); at 2.16% salt, it increases again from 0.571 to 0.724 MPa^{-1} (+26.8%); and at 3.16% salt, it decreases from 0.550 to 0.534 MPa^{-1} (−2.9%). This inconsistent behavior suggests that the effectiveness of EICP treatment in the 100-200 kPa range is highly sensitive to salt concentration, possibly due to interactions between calcite precipitation and pre-existing salt crystals. Figure 5(b) presents the compression index C_c obtained from the 200-800 kPa normal consolidation range. For untreated

loess, C_c decreases steadily from 0.263 to 0.158 (−40%) as salt content increases, confirming that salt also reduces high-pressure compressibility. EICP treatment produces a clearer pattern: at 0.16% salt, C_c drops from 0.263 to 0.211 (−19.8%); at 1.16% salt the change is negligible (0.174 to 0.172, −1.1%); but at 2.16% and 3.16% salt, C_c unexpectedly increases compared to untreated samples (from 0.173 to 0.203, +17.3%; and from 0.158 to 0.185, +17.1%, respectively). This contrasting trend indicates that EICP-induced cementation effectively reduces compressibility under low-salt conditions, yet becomes detrimental at high salt contents, presumably because the cementation solution disturbs the existing salt-cemented fabric or forms a weaker particle network.

Comparing the two indices, the response of compression parameters at different pressure ranges to EICP treatment differs markedly. In untreated samples, both indices decrease with increasing salt content, showing consistency. However, after EICP treatment, $a_{1\text{-}2}$ displays large non-monotonic fluctuations (e.g., a +26.8% change at 2.16% salt), while C_c shows a more systematic trend: beneficial at low salinity and detrimental at high salinity (2.16% salt). The discrepancy may be attributed to the different pressure ranges: $a_{1\text{-}2}$ reflects the soil's response in the transitional stress stage that may still be influenced by the pre-consolidation pressure, whereas C_c captures the intrinsic compressibility in the fully normal-consolidated region. Therefore, compared with $a_{1\text{-}2}$, C_c provides a more consistent measure for evaluating the long-term effect of EICP treatment on soil compressibility in the normally consolidated stress range (200−800 kPa). The C_c trend clearly reveals that EICP treatment is beneficial only for low-salt loess in this stress regime, but may inadvertently increase compressibility when the salt content reaches approximately 2.16%.

According to the results presented in Figures 5(c) and 5(d), the constrained modulus E_s and the pre-consolidation pressure P_c exhibit broadly similar evolution trends, although the governing physical mechanisms differ to some extent. For the untreated loess, both parameters increase with increasing salt content. Specifically, E_s rises from 2.68 MPa to 3.02 MPa, while P_c increases from 47.3 kPa to 74.1 kPa. This behavior can be attributed to salt-induced crystallization and apparent cementation effects, which enhance interparticle bonding, increase soil stiffness and structural yield strength, and consequently reduce compressibility. For the EICP-treated loess, the response is non-monotonic with respect to salinity. At a low salt content of 0.16%, both E_s and P_c decrease slightly (by 4.9% and 11.6%, respectively), which may be associated with dilution effects of the treatment solution and/or disturbance of the original soil fabric. At salt contents of 1.16% and 3.16%, both parameters increase significantly (E_s: +9.6% and +7.9%; P_c: +20.9% and +7.7%), indicating that a favorable saline environment facilitates calcium carbonate precipitation, thereby promoting effective cementation and enhancing soil stiffness and structural strength. In contrast, at salt content of 2.16%, both parameters decrease markedly (E_s: −19.3%, P_c: −18.0%), suggesting the presence of an unfavorable salinity range in which EICP treatment may disrupt pre-existing salt-crystal skeletons or lead to the formation of weak and discontinuous cementation products.

Overall, E_s and P_c exhibit consistent responses to EICP treatment. Unlike C_c, which captures the high-stress normally consolidated behavior, these two parameters reflect the soil response at low to moderate stress levels. The results indicate that, under these stress conditions, EICP treatment is unfavorable at the lowest salinity (0.16%), beneficial at moderate and high salinities (1.16% and 3.16%), and detrimental at intermediate-high salinity (2.16%). This divergence from the C_c trend underscores that the effect of EICP on saline loess is stress-range-dependent. In practical applications, soils with salt contents of ~2.16% should be avoided, or the treatment formulation should be optimized to accommodate such conditions.

3.2 UCS tests in ambient temperature

Based on the overall trends in the stress-strain curves, the unconfined compressive strength curves of loess under both untreated and EICP-cured conditions, regardless of salt content, exhibit relatively typical phased characteristics and can be broadly divided into a linear elastic stage, a softening stage, and a residual strength stage. In the linear elastic stage (Figure 6a), stress increases approximately linearly with strain; this stage primarily reflects the soil's compression process.

Following the elastic stage, the specimen reaches a peak and enters the softening stage, during which stress begins to decrease, accompanied by the expansion and penetration of internal cracks within the specimen. Subsequently, the specimen enters the residual strength stage. At this point, the main cracks have largely formed, the stress decline becomes more gradual, and the specimen maintains a certain load-bearing capacity primarily through intergranular friction. In terms of failure mode, the untreated specimen exhibited ductile failure characteristics in the soil's compression process, whereas the low-salinity EICP-treated specimen displayed brittle failure. As the salt content increases, EICP-stabilized soil (Figure 6b) exhibits a gradual transition from brittle to ductile behavior. For stabilized specimens with 0.16% and 1.16% salt content, the initial segment of the curve is relatively steep, indicating high soil stiffness; the curve reaches its peak when the axial strain approaches 3% and drops rapidly thereafter. For the solidified specimens with a salt content of 2.16%, the peak stress-strain curve shifted to the rightward, with a slight decrease in peak stress and an increase in ductility. As the salt content rose to 3.16%, the stress-strain curve became flatter; the peak stress decreased by nearly half compared to the 0.16% group and remained at a lower level after reaching the peak.

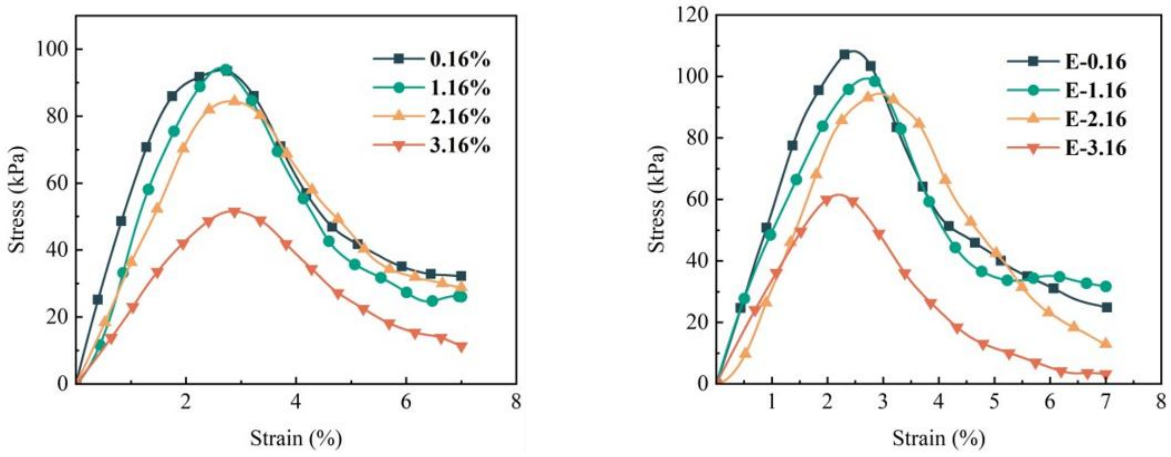

a) Untreated b) EICP-treated

Figure 6 – Stress and strain curves of saline loess

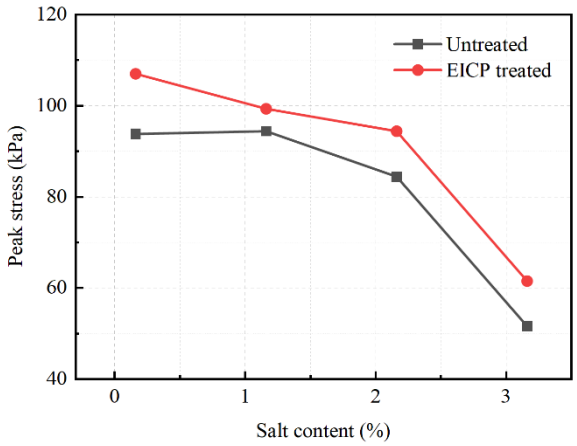

Figure 7 – Peak strength of UCS for saline loess

As shown in Figure 7, salt content has a significant effect on the mechanical properties of untreated specimens. As salt content increases, the peak compressive strength exhibits a monotonically decreasing trend: when the salt content is 3.16%, the specimen strength decreases by approximately 45% compared to the 0.16% group. The primary reason is that aggregates and crystals formed by excess sulfates increase the soil’s porosity and surface roughness, thereby weakening the cementation between particles. In contrast, the EICP-stabilized group exhibited increased strength at all salt content levels, indicating that calcium carbonate cementation played an effective role.

However, the influence of salt content on the reinforcement effect remains quite significant. Specifically, at a salt content of 0.16%, the peak stress reached 108 kPa, approximately 1.15 times that of the untreated group; whereas at a salt content of 3.16%, the peak stress was only 61 kPa, with a significantly reduced increase. When the salt content exceeded 2.16%, the decline in cementation effectiveness accelerated, and its strength characteristics gradually approached those of the untreated soil samples, indicating that high-salt environments inhibit urease activity.

Overall, the EICP technique demonstrated significant reinforcement effects in loess with salt contents of 0.16% and 1.16%; however, when the salt content reached 2.16% or higher, the reinforcement effect was significantly suppressed. Therefore, when applying the EICP technique in high-salinity regions such as the Ili Valley, the inhibitory effect of salt on urease activity must be carefully considered in the mix design.

3.3 Unconfined compressive strength tests following freeze-thaw cycles

Under unconfined compression, soils typically exhibit several characteristic failure modes, including end shearing, barreling, single shear plane, and disintegration. Figure 8 presents the failure patterns of loess specimens subjected to freeze-thaw cycling under unconfined compressive conditions. The results indicate that, with increasing numbers of freeze-thaw cycles, the failure mode progressively evolves from end-dominated shear and distinct single shear planes to distributed cracking, and ultimately to disintegration.

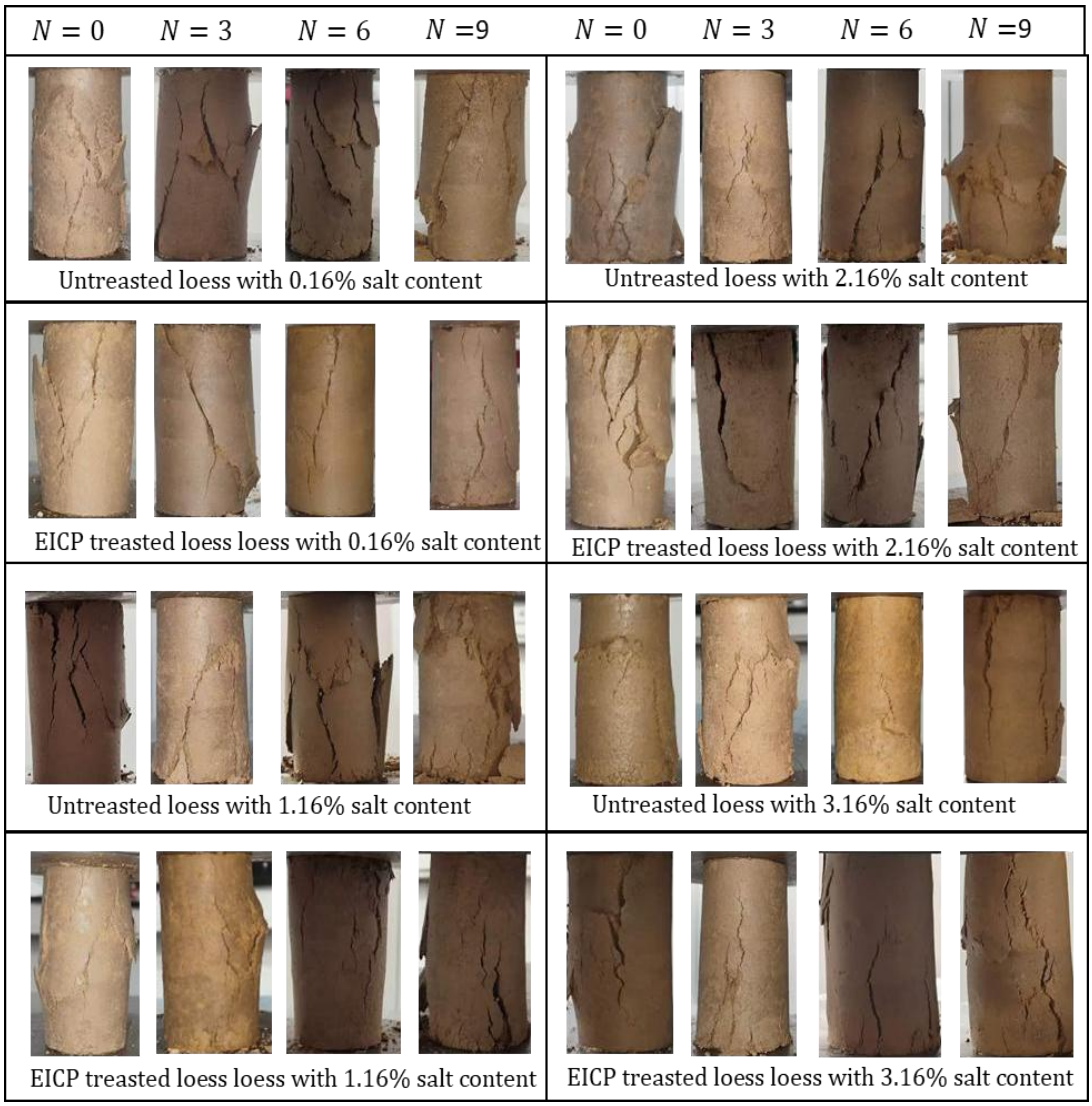

Figure 8 – Failure modes of molded loess specimens after freeze-thaw cycling under UCS testing

An increase in salinity further accelerates this transition by weakening interparticle bonding and inducing crystallization-related damage. Under the combined effects of numerous freeze-thaw cycles and elevated salinity, the specimens exhibit pronounced structural collapse and fragmentation, reflecting a shift from shear-controlled failure to degradation governed by structural deterioration.

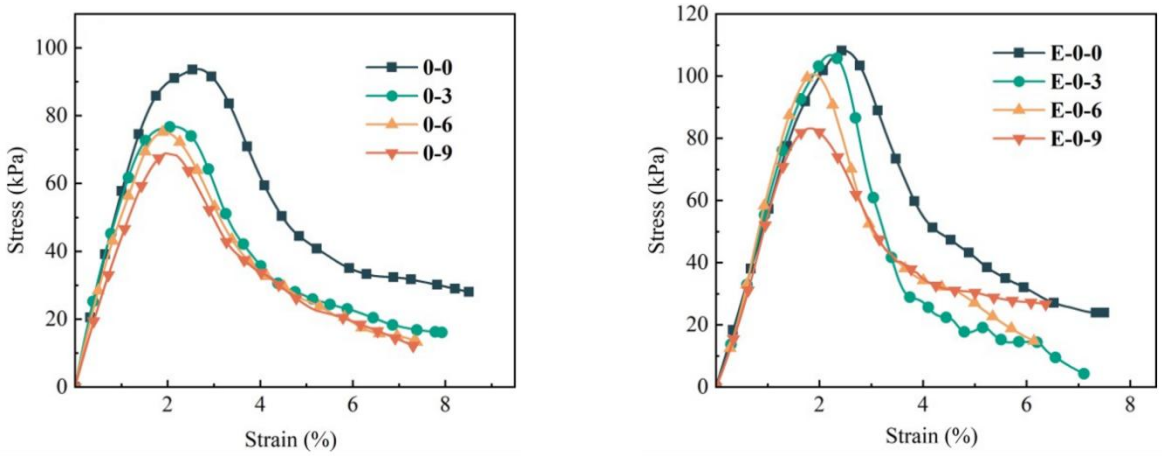

a) Untreated b) EICP-treated

Figure 9 – UCS Curves of specimens under 0.16% salinity condition with freeze-thaw cycling

Figure 9 shows the stress-strain curves of untreated and EICP-treated specimens after different numbers of freeze-thaw cycles at a salt content of 0.16%. All specimens exhibited typical stress-strain behavior: a linear elastic stage, a post-peak softening stage, and a residual stage. As the number of freeze-thaw cycles increased, both peak stress and residual strength decreased, indicating that freeze-thaw cycles disrupted internal cohesion within the soil and weakened structural integrity. The strength degradation of the untreated specimens was faster and more pronounced. Although the peak stress of the EICP-treated specimens was higher than that of the untreated group, their ductility decreased with increasing freeze-thaw cycles, indicating that freeze-thaw cycles had a more significant impact on the ductility of the EICP-treated specimens.

The unconfined compressive strength (UCS) of loess is affected by both freeze-thaw cycles and salt content, with higher cycle counts and salinity generally leading to strength reduction. As shown in Figure 10, the bio-cementation formed by EICP treatment significantly enhances the UCS of the specimens, with increases ranging from 15.2% to 39.1% under different freeze-thaw cycles. This demonstrates the effectiveness of EICP in enhancing the freeze-thaw resistance of the soil. Although UCS generally decreases with increasing freeze-thaw cycles, the EICP-treated group exhibits better durability. Taking the salt content of 0.16% as an example (Figure 10(a)), the strength of the untreated specimen decreases by approximately 18% after three freeze-thaw cycles, while the EICP-treated specimen loses only 23% of its strength after nine cycles, indicating a substantially slower rate of deterioration per cycle.

Across all panels of Figure 10, a higher salt content leads to a significant decrease in the peak strength of untreated specimens, with the peak stress decreasing from 94.4 kPa at a salt content of 0.16% to 63.4 kPa at 3.16%, a reduction of 32.8%. Focusing on the 1.16% salt group (Figure 10(b)), after EICP treatment, the specimens maintain a relatively high peak stress and good strength retention; however, the slope of the post-peak softening stage becomes steeper compared with the untreated specimens, indicating reduced ductility. Regarding the freeze-thaw effect, EICP treatment significantly improves the freeze-thaw resistance of the specimens. At a salt content of 1.16%, the strength of untreated specimens decreases by approximately 22.5% after three freeze-thaw cycles, showing pronounced deterioration. In contrast, the strength of EICP-treated specimens decreases by only about 21.4% after nine freeze-thaw cycles, demonstrating that EICP treatment effectively retards strength reduction and enhances structural stability.

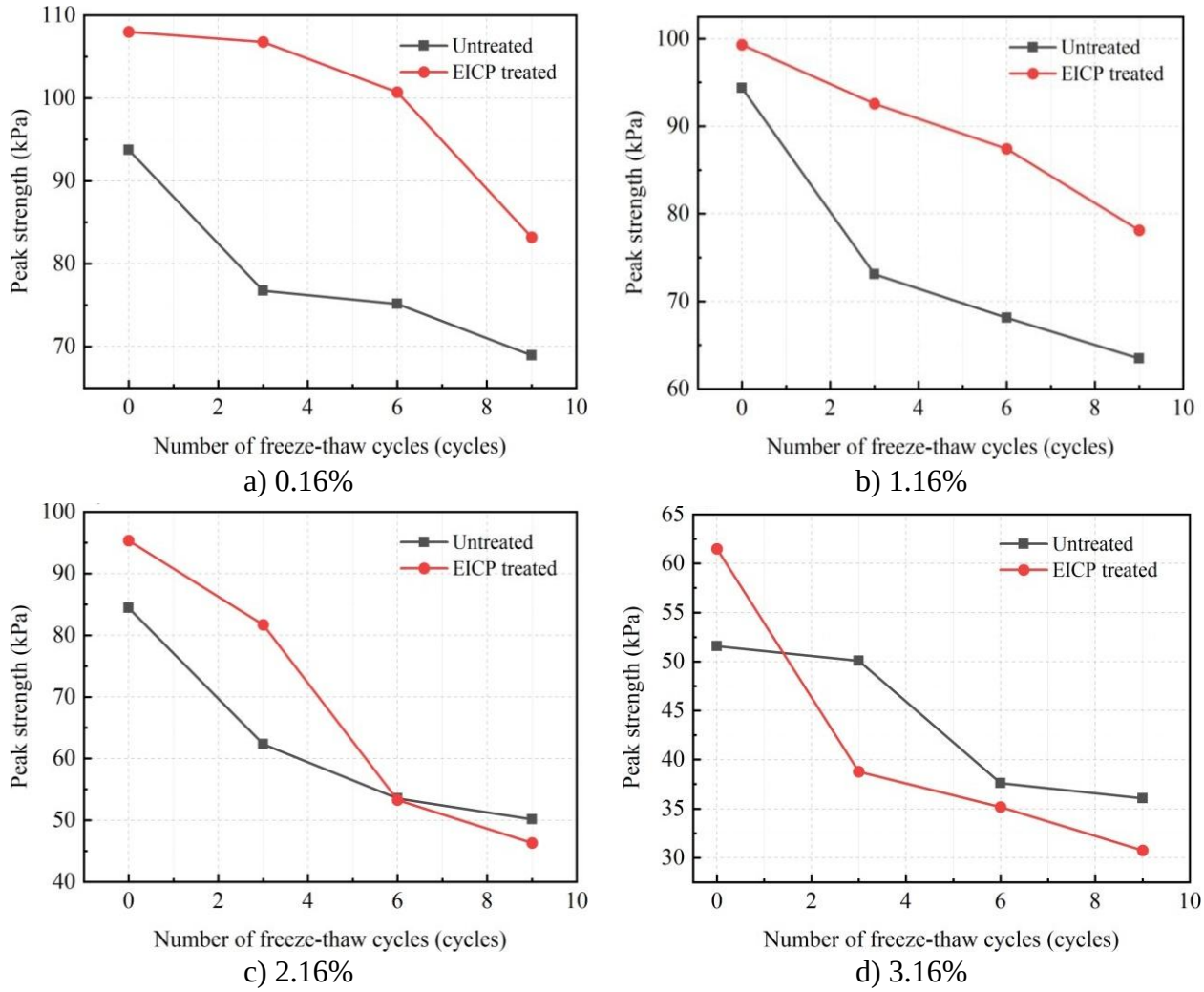

Figure 10 – Peak strength of saline loess with various salt content following freeze-thaw cycles

Figure 10(c) presents the variation in peak unconfined compressive strength (UCS) of specimens with a salt content of 2.16% before and after EICP treatment under different numbers of freeze-thaw cycles. Compared with the specimens at salt contents of 0.16% and 1.16%, the stress-strain curves of the 2.16% salt content specimens also exhibit the three characteristic stages of elastic loading, post-peak softening, and residual response. However, the reduction in peak strength is significantly greater, indicating that a high-salt environment has a more pronounced deterioration effect on the soil structure. As the number of freeze-thaw cycles increases, the strength of the EICP-treated specimens gradually decreases from 95.4 kPa to 46.3 kPa. Notably, after six freeze-thaw cycles, the strength of the EICP-treated specimens becomes lower than that of the untreated loess. Despite the continuous decline in peak strength with increasing freeze-thaw cycles, the peak strain of the EICP-treated specimens remained consistently higher than that of the untreated specimens across all cycle levels. Under 0, 3, 6, and 9 freeze-thaw cycles, the peak strains of the EICP-treated loess were approximately 3.0%, 5.0%, 5.5%, and 5.4%, respectively, whereas those of the untreated loess merely ranged from 2.3% to 2.8%. This observation indicates that, under the high-salt condition of 2.16%, EICP treatment substantially alters the deformation characteristics of the soil, shifting the failure mode from the brittle behavior observed at low salt contents toward a distinctly more ductile failure with enhanced deformability.

Figure 10(d) shows that for specimens with a salt content of 3.16%, the overall trend is generally consistent with that of the other salt content groups (0.16%, 1.16%, and 2.16%), all exhibiting the characteristic stages of elastic loading, post-peak softening, and residual response. Nevertheless, with increasing salt content, the peak strength decreases significantly, and the post-peak drop becomes steeper, indicating that a high-salt environment markedly weakens the structural

stability and cementation strength of the soil.

As the number of freeze-thaw cycles increases, the strength of the EICP-treated specimens continuously decreases, showing a more pronounced degradation trend compared with the untreated specimens. After only three freeze-thaw cycles, the strength of the EICP-treated specimens falls below that of the untreated loess. This turning point occurs earlier than in the 2.16% salt group, demonstrating that the freeze-thaw action damages the bio-cemented structure more rapidly under a high-salt environment. This accelerated degradation is consistent with microstructural observations from analogous MICP-treated sulfate saline soils, where SEM-EDS imaging showed that elevated Na_2SO_4 contents shifted carbonate precipitation from interparticle contacts and pore spaces toward predominantly particle-surface coating. This transition weakened the contact-bonding network and produced a less integrated fabric, making the treated soil more susceptible to freeze-thaw-induced cracking, spalling, and cementation loss [16].

A further comparison of peak strain reveals that, under 0, 3, 6, and 9 freeze-thaw cycles, the peak strains of the EICP-treated loess were approximately 2.2%, 5.2%, 8.2%, and 8.8%, respectively, whereas those of the untreated loess were 2.8%, 4.0%, 6.8%, and 9.8%, respectively. The EICP-treated specimens exhibited a higher peak strain than the untreated specimens at 3 and 6 cycles, but a lower peak strain at 0 and 9 cycles, indicating no consistent benefit in deformability. This result suggests that, at a salt content of 3.16%, freeze-thaw cycling leads to severe structural deterioration in both treated and untreated soils, and both exhibit pronounced flow-plastic deformation characteristics. Under such high-salinity conditions, freeze-thaw damage may progressively weaken the cemented structure, leading to unstable deformation behavior and reduced post-peak stability.

In summary, under the high-salt condition of 3.16%, the strengthening effect of EICP treatment is significantly weakened. Although the EICP-treated specimens may retain limited deformation capacity at certain freeze-thaw stages, this effect is not consistent. With increasing freeze-thaw cycles, the calcium carbonate-cemented structure gradually deteriorates, resulting in rapid strength loss, unstable deformation behavior, and reduced post-peak stability.

It should be noted that the mechanical effect of salinity is loading-mode dependent. Under one-dimensional compression, salt crystallization and pore filling may increase apparent stiffness and structural yield strength, as reflected by the reduced compressibility and increased E_s and P_c of untreated loess. In contrast, under unconfined compression, excessive salinity may weaken effective interparticle bonding and reduce post-peak stability, leading to lower UCS strength and more pronounced softening behavior.

Overall, under salt content conditions of 0.16% and 1.16%, EICP curing can consistently improve the initial strength of the soil and maintain a peak strength higher than that of the untreated group during 0 to 9 freeze-thaw cycles. The rate of strength degradation is relatively gradual, demonstrating good freeze-thaw durability. When the salt content reaches 2.16% or higher, the strength of EICP-treated soil deteriorates more rapidly after initial freeze-thaw cycles, and the peak strength falls below the untreated level after a certain number of cycles. As the salt concentration increases further, this reversal point occurs significantly earlier: it occurs during the 6th cycle for the 2.16% salt group and as early as the 3rd cycle for the 3.16% salt group.

4. Conclusions

1. EICP treatment significantly modified the mechanical behavior of saline loess, and the improvement effect was strongly dependent on salt content. Under low-salt conditions (≤1.16%), the treated specimens exhibited a reduced compression index C_c (by up to 19.8%), indicating suppressed structural collapse and improved resistance to particle rearrangement. However, this beneficial effect was not sustained with increasing salinity. At salt contents ≥2.16%, C_c increased by approximately 17% after treatment, suggesting that excessive salinity adversely affects the development and continuity of interparticle bonding during EICP treatment.

2. Salinity therefore exerts a dual effect on EICP-treated loess. Low salt levels facilitate

calcium carbonate precipitation and enhance stiffness and structural strength, whereas unfavorable salinity conditions, particularly at 2.16%, consistently represent the most unfavorable condition content, weaken the macroscopic improvement effect, and reduce treatment effectiveness. This behavior may be associated with changes in solution chemistry, salt–soil interaction, and the spatial distribution of cementation products; however, the underlying microstructural and chemical mechanisms require further verification. Although previous studies have examined salinity-related changes in $CaCO_3$ polymorphism and crystal morphology in EICP-treated saline soils, as well as the microstructural deterioration of MICP-treated sulfate saline soils under freeze-thaw cycling, direct SEM/XRD evidence for the coupled effects of sulfate salinity, EICP treatment, and freeze-thaw cycling in loess remains limited. This gap motivates the microstructural investigations recommended for future work.

3. Freeze-thaw cycling further accelerates structural degradation, driving a transition in failure mode from end-dominated shear and single shear planes to distributed cracking and eventual disintegration. Under low-salinity conditions, EICP enhanced strength and delayed degradation under cyclic freeze-thaw conditions, with unconfined compressive strength increasing by 15−39%. However, under high salinity conditions, particularly after 6 freeze-thaw cycles, the beneficial effects of EICP diminished or even reversed, with treated specimens exhibiting lower strength than untreated ones. These results indicate that under adverse salinity conditions, the long-term effectiveness of EICP treatment can be severely compromised.

4. These findings suggest that EICP is a promising ground improvement technique for loess soils; however, in saline–alkali and cold regions, its performance depends largely on environmental compatibility and requires targeted optimization, such as adjusting the cementation solution formulation or pre-treating the soil to mitigate salt interference, to ensure reliable field application.to ensure reliable field application.

Acknowledgments

This work was supported by Tianshan Talent Training Program (Grant No. 2023TSYCLJ0055), Xinjiang University “Outstanding Graduate Student Innovation Project” (Grant No. XJDX2025YJS222).

References

[1] H. Ding, Y. Li, Y. Yang, and X. Jia, “Origin and evolution of modern loess science – 1824 to 1964,” *Journal of Asian Earth Sciences*, vol. 170, pp. 45–55, 2019, doi: 10.1016/j.jseaes.2018.10.024.

[2] D. R. Muhs, “Loess Deposits, Origins and Properties,” in *Encyclopedia of Quaternary Science*, Amsterdam, Netherlands: Elsevier, 2007, pp. 1405–1418. doi: 10.1016/B0-44-452747-8/00158-7.

[3] Y. Li, W. Shi, A. Aydin, M. A. Beroya-Eitner, and G. Gao, “Loess genesis and worldwide distribution,” *Earth-Science Reviews*, vol. 201, p. 102947, 2020, doi: 10.1016/j.earscirev.2019.102947.

[4] K. Pye, “The nature, origin and accumulation of loess,” *Quaternary Science Reviews*, vol. 14, no. 7–8, pp. 653–667, 1995, doi: 10.1016/0277-3791(95)00047-X.

[5] Y. Li *et al.*, “Atmospheric dust dynamics over Central Asia: A perspective view from loess deposits,” *Gondwana Research*, vol. 109, pp. 150–165, 2022, doi: 10.1016/j.gr.2022.04.019.

[6] J. M. Plata, J. C. Balasch, J. Boixadera, A. Baltiérrez, F. Preusser, and R. M. Poch, “Source areas and paleoenvironmental reconstruction of the Serra d’Almenara loess (NE Ebro Valley, Iberian Peninsula) from grain-size and heavy mineral signatures,” *Geomorphology*, vol. 451, p. 109085, 2024, doi: 10.1016/j.geomorph.2024.109085.

[7] X. Han, Z. Hu, H. Li, Y. Yin, B. Zhang, and L. Zhang, “Study on the mechanical properties and microstructural evolution of loess under different wet dry and freeze thaw coupled cycling paths,” *Case Studies in Construction Materials*, vol. 21, p. e03924, 2024, doi: 10.1016/j.cscm.2024.e03924.

[8] M. Zhuang *et al.*, “Mechanistic Investigation of Typical Loess Landslide Disasters in Ili Basin, Xinjiang, China,” *Sustainability*, vol. 13, no. 2, p. 635, 2021, doi: 10.3390/su13020635.

[9] Y. Xian, X. Wei, N. Chen, Y. Qi, and H. Xu, “The effects of snowmelt on loess landslides in Tian Shan, China,” *Journal of Hydrology: Regional Studies*, vol. 62, p. 102995, 2025, doi: 10.1016/j.ejrh.2025.102995.

[10] I. J. Smalley *et al.*, “The formation of loess deposits in the Tashkent region and parts of Central Asia; and problems with irrigation, hydrocollapse and soil erosion,” *Quaternary International*, vol. 152–153, pp. 59–69, 2006, doi: 10.1016/j.quaint.2005.12.002.

[11] K. Martin, H. K. Tirkolaei, and E. Kavazanjian, "Enhancing the strength of granular material with a modified enzyme-induced carbonate precipitation (EICP) treatment solution," *Construction and Building Materials*, vol. 271, p. 121529, 2021, doi: 10.1016/j.conbuildmat.2020.121529.
[12] I. Ahenkorah, M. M. Rahman, M. R. Karim, and S. Beecham, "Enzyme induced calcium carbonate precipitation and its engineering application: A systematic review and meta-analysis," *Construction and Building Materials*, vol. 308, p. 125000, 2021, doi: 10.1016/j.conbuildmat.2021.125000.
[13] Z. Zhang, K. Wang, C. Cui, and L. Yu, "Performance and Mechanism of Enzyme-Induced Carbonate Precipitation (EICP) for Fine-Grained Saline Soil Stabilization," *Applied Sciences*, vol. 16, no. 2, p. 1057, 2026, doi: 10.3390/app16021057.
[14] "GB/T 50123-2019 Standard for geotechnical testing method," Beijing, China: China Planning Publishing House, 2019, p. 508.
[15] "ASTM D2435/D2435M-11(2020) Standard Test Methods for One-Dimensional Consolidation Properties of Soils Using Incremental Loading," West Conshohocken, PA: ASTM International, 2020, p. 14.
[16] L. Xiong, L. Tian, X. Zhang, M. Wang, and A. Ahemaiti, "Mechanical properties and microstructural analysis of MICP-reinforced coarse-grained saline soils under freeze-thaw cycling," *PLoS One*, vol. 20, no. 11, p. e0336266, 2025, doi: 10.1371/journal.pone.0336266.

Information about authors:
Kaixin Shi – Master Candidate; 1) College of Civil Engineering and Architecture, Xinjiang University, Urumqi, China; 2) Xinjiang Key Laboratory of Building Structure and Earthquake Resistance, Xinjiang University, Urumqi, China; 107552304720@stu.xju.edu.cn
Li Ma – PhD, Associate Professor, Master Supervisor; 1) College of Civil Engineering and Architecture, Xinjiang University, Urumqi, China; 2) Xinjiang Key Laboratory of Building Structure and Earthquake Resistance, Xinjiang University, Urumqi, China; mali@xju.edu.cn
Xuejun Liu – Professorate Senior Engineer, Xinjiang Institute of Building Science Co., Ltd, Urumqi, China, 625184594@qq.com

Author Contributions:
Kaixin Shi – data collection, testing, modeling, analysis, visualization, interpretation, drafting.
Li Ma – funding acquisition, concept, methodology, resources, editing.
Xuejun Liu – analysis, interpretation.

Conflict of Interest: The authors declare no conflict of interest.

Use of Artificial Intelligence (AI): AI was used to assist in literature screening and language refinement, as well as to aid in the creation of Figures 1 and 2, which were generated with the assistance of an AI image generation tool. All content was critically reviewed, verified, and edited by the authors to ensure accuracy and scientific integrity.

Received: 28.04.2026
Revised: 20.06.2026
Accepted: 22.06.2026
Published: 24.06.2026

Technobius, 2026, 6(2), 0103, DOI: https://doi.org/10.54355/tbus/27897338.6.2.2026.0103

Technobius

https://technobius.kz/

e-ISSN 2789-7338

Article

Study on the influence of polycarboxylic acid water-reducing agent on the performance of gypsum-modified mud mortar

Sawulet Bekey[1,2,*], Wumeng Liu[3], Qing Wang[1], Wenze Wang[1], Jingzheng Mi[1]

[1]College of Architecture and Engineering, Xinjiang University, Urumqi, China
[2]Xinjiang Key Laboratory of Building Structure and Earthquake, Xinjiang University, Urumqi, China
[3]NO.2 Engineering Co., Ltd. OF CCCC Third Harbor Engineering Co., Ltd., Shanghai, China
*Correspondence: jgxyswlt@xju.edu.cn

Abstract. Masonry mortar, as the primary bonding material in adobe construction, plays a crucial role in the integrity of adobe masonry due to its working properties, compressive strength, and shrinkage rate. Based on the use of industrial by-product gypsum for sustainable material modification, gypsum and polycarboxylate superplasticizer were added to address the defects of the masonry mortar and explore their impact. The effect of gypsum on the compressive strength of the mortar specimens exhibited a trend of initially decreasing, then increasing, and eventually decreasing again within a certain range. The experiment found that a 20% gypsum content led to the greatest improvement in compressive strength, reaching 3.12 MPa, which is 1.49 times that of the plain mortar specimens. However, adding gypsum alone negatively affected the mortar's consistency, water retention, and volume shrinkage. Therefore, a combination of polycarboxylate superplasticizer and gypsum was studied to evaluate the mortar's performance. The experiment showed that polycarboxylate superplasticizer effectively improved the consistency and water retention of the gypsum-modified mortar, enabling it to meet the required consistency for masonry under low water-to-soil ratios. The optimal dosage of the superplasticizer ranged from 0.5% to 1.0%, which significantly improved the consistency and water retention properties, with water retention reaching up to 99%. Polycarboxylate superplasticizer also improved the volume shrinkage of the gypsum-modified mortar. With 1% superplasticizer, the volume shrinkage rate of the mortar specimens was reduced to below 10%, almost half of the shrinkage rate of the unmodified mortar. The compressive strength of the gypsum-modified mortar also showed significant improvement with the addition of the superplasticizer. The compressive strength of the mortar increased with the amount of superplasticizer, and when 20% gypsum and 1.5% superplasticizer were mixed, the compressive strength of the mortar specimens reached 5.96 MPa, which is 2.84 times higher than that of the plain mortar specimens.

Keywords: desulphurization gypsum, polycarboxylate water reducing agent, denseness, water-retaining property, compressive strength.

1. Introduction

As early as the Neolithic period, 8000 years ago, humans began using unfired earth as a building material for the construction of dwellings. As one of the most primitive building materials, raw earth has been utilized in construction worldwide [1]. According to incomplete statistics from UNESCO, approximately two billion people globally still reside in various forms of earthen architecture, including earth-sheltered dwellings, rammed earth structures, and cave dwellings. Compared with conventional building materials, raw earth offers economic advantages such as convenient sourcing, ease of processing, and low cost. Earthen architecture is also highly harmonious and environmentally friendly with the natural surroundings; it can be reused or returned to nature after demolition, generating virtually no pollution, which is of significant importance for environmental protection and the maintenance of ecological balance.

Earthen buildings are predominantly masonry structures constructed from traditional adobe blocks and their corresponding earthen mortar. However, compared with industrial materials such as cement mortar, concrete, and fired bricks, earthen mortar exhibits issues including low strength, substantial volumetric shrinkage, and poor water retention capacity [2], [3]. In response to these existing problems, numerous studies [4] have been conducted to modify earthen mortar, yielding relatively favorable results. In 1895, while investigating the formation mechanisms of saline-alkali soils, European and American scholar Hilgard discovered through experimentation that gypsum exerted a beneficial effect on ameliorating the saline-alkali environment within the soil, thereby initially identifying the potential of natural gypsum for the improvement of sodic saline-alkali soils. Over the subsequent period spanning more than a century, countries including China, the United States, Australia, and India have conducted research on the effects of gypsum on the amelioration of saline-alkali soils, as well as on the workability and mechanical properties of masonry mortars [5], [6], [7], [8], [9], [10], [11], achieving numerous notable advancements. Research indicates that the modification of earthen materials using industrial by-products such as flue gas desulfurization (FGD) gypsum can effectively enhance their compressive strength, water resistance, and weatherability [12]. Concurrently, modification with gypsum constitutes a widely adopted approach for the improvement of earthen mortar. When employed as a modifying agent, gypsum exhibits the characteristic of rapid setting, enabling the formation of a complete skeletal framework that imparts early strength to the mortar and substantially improves the mechanical properties of mortar specimens [13]. Superplasticizers, which are commonly used as admixtures in concrete, have found widespread application, and their utilization in the modification of earthen mortar is currently being investigated by numerous researchers [14], [15]. The incorporation of superplasticizers serves both to enhance the fluidity of the mortar and to reduce the water content required during mixing, thereby mitigating drying shrinkage cracks and salt efflorescence on the surface of mortar specimens caused by moisture evaporation. Qian et al. [16] investigated the influence of polycarboxylate superplasticizer on the workability and mechanical properties of gypsum-fly ash modified earthen mortar, concluding that a superplasticizer dosage of 0.8% was sufficient to enable casting and molding of the mud mortar, and further determining that, within a certain range, the compressive strength of the modified mortar increased with increasing superplasticizer content. Existing research demonstrates that gypsum and superplasticizers can effectively ameliorate the inherent deficiencies of earthen mortar. During the course of investigation, it was observed that while modification with gypsum enhances compressive strength, it may adversely affect volumetric stability and water retention. Based on prior experience, modification using polycarboxylate superplasticizer was undertaken to examine the effects of the superplasticizer on the consistency, volumetric stability, water retention, and compressive strength of the gypsum-modified earthen mortar.

2. Methods

2.1 Experimental Materials

The loess excavated from the Xinjiang region was used as soil material. Before testing, the soil was sieved to remove larger stones, debris, and other extraneous matter. In the Urumqi soil particles, silt particles (4–63μm) constitute the largest proportion, accounting for approximately 46.24%–62.49%; clay particles (<4μm) account for 15.97%–35.02%; and sand particles (>64μm) represent the smallest proportion, ranging from approximately 8.16%–37.71%. The basic composition of the soil is presented in Table 1.

Table 1 – Content of various components in the soil used for testing, mg/kg

Na	K	Ca	Mg	HCO^-_3
1668.82	11.34	94.95	27.70	220

The FGD gypsum used in the experiment was sourced from a cement plant in Urumqi. Similar to natural gypsum, its primary constituent is calcium sulfate dihydrate ($CaSO_4 \cdot 2H_2O$). It is primarily

derived from the flue gas desulfurization process and is characterized by a fine particle size, stable composition, and low levels of harmful impurities. FGD gypsum powder also contains silicon dioxide, sodium oxide, calcium carbonate, calcium sulfite, limestone, calcium chloride, and magnesium chloride [17], among other components. It is widely utilized in industries such as building materials, which not only vigorously promotes the further development of the national environmental circular economy but also substantially reduces the extraction of mineral gypsum, thereby conserving resources. It is considered an environmentally friendly material. The specific composition is detailed in Table 2.

Table 2 – Main components of FGD gypsum, %

$CaSO_4 \cdot 2H_2O$	CaO	SO_3	Al_2O_3	SiO_2	Fe_2O_3
≥93	30.42	46.38	1.59	5.46	1.11

The polycarboxylate high-performance superplasticizer (water reduction rate: 42.3%) manufactured by Jinan Shanhai Chemical Technology Co., Ltd. (Jinan, China) was selected. This product conforms to the current national standard [18]. The main component content and factory inspection technical specifications for this polycarboxylate superplasticizer are presented in Table 3.

Table 3 – Main inspection indicators of polycarboxylate superplasticizer

Item	Cl^- content, %	Moisture content, %	Water reduction rate, %	Bleeding rate ratio, %
Standard	≤0.1	≤5	≤25	≤60
Result	0.01	2.5	42.3	24.7
Evaluation	Conforming	Conforming	Conforming	Conforming

2.2 Experimental program

The experimental program consisted of several testing procedures, including the consistency test, water retention test, compressive strength test, and volumetric shrinkage rate measurement.

The consistency in this study refers to the property of mortar, indicating its ease of flow under self-weight or external force, serving as a measure of a material's resistance to permanent deformation. Based on construction experience, when the consistency value of earthen mortar is controlled within the range of 40–50 mm, the fluidity is deemed appropriate and convenient for masonry operations. The test procedures were conducted in full accordance with the [19].

The water retention test was conducted immediately following the completion of the consistency test. The water retention rate index refers to the [20], wherein a water retention rate exceeding 88% is considered qualified.

A compressive strength test was performed with reference to the cube compressive strength test specified in [19]. The dimensions of the test specimens were 70.7×70.7×70.7 mm, with three specimens constituting one group. The specimens were subjected to a curing period of 28 days. After specimen molding, they shall be kept at room temperature (20±5) °C and a relative humidity of not less than 90% for (24±2) h before demolding. After demolding, the specimens shall be immediately placed in a standard curing room for curing. The loading rate during testing shall be 0.2 to 1.5 kN per second. The arithmetic mean of the measured values from the three specimens in a group was taken as the average compressive strength for that group. If the difference between the maximum value or the minimum value among the three measurements and the median value exceeded 15% of the median value, both the maximum and minimum values were discarded, and the median value was taken as the compressive strength value for that group of specimens. The test equipment used is a YAW-3000 electro-hydraulic servo compression testing machine (Jinan Xinguang Test Machine Manufacturing Co., Ltd., Jinan, China).

For the volumetric shrinkage rate measurement, the specimens used were identical to those employed in the cube compressive strength test. Measurements of dimensions were taken at 7 days and 28 days, respectively. The degree of shrinkage of the earthen mortar was expressed in terms of the natural shrinkage rate. The volumetric shrinkage rate is calculated according to Eq. (1).

$$\varepsilon = \frac{V_0 - V_i}{V_0}, \quad (1)$$

where: ε – natural drying volumetric shrinkage rate; V_0 – initial volume after 7 days of curing, mm^3; V_i – molded volume after 28 days of curing, mm^3.

The amounts of FGD gypsum and polycarboxylate superplasticizer incorporated in the experiment were both added as a percentage of the soil mass. With the soil mass fixed as 1, gypsum was sequentially added at proportions of 10%, 15%, 20%, 25%, and 30% of the soil mass to investigate the effect of single gypsum addition on various properties of the earthen mortar. Based on the experimental results obtained from the aforementioned tests, three distinct gypsum dosage levels were selected and subsequently combined with polycarboxylate superplasticizer at dosages of 0.5%, 1.0%, and 1.5%, respectively, for further investigation of their combined effects.

3. Results and Discussion

3.1 Effect of a single addition of gypsum on the consistency and water retention of earthen mortar

The experiment was conducted according to the mixed proportions specified above; the data for the single gypsum addition are presented in Table 4 below.

Table 4 – Data of mortar consistency and water-soil ratio with single gypsum addition

Sample ID	Consistency, mm	Soil amount, kg	Water amount, kg	Water-soil ratio
SGT10	48	2	0.50	1:4
SGT15	49	2	0.60	1:3.33
SGT20	48	2	0.75	1:2.67
SGT25	47	2	0.80	1:2.5
SGT30	48	2	0.85	1:2.35

The consistency of the earthen mortar was adjusted within the range of 40 to 50 mm by controlling the water-to-soil ratio to enable the mortar to meet the requirements for masonry work, as well as to avoid a serious reduction in cohesion, bleeding, and segregation effects in fresh mortar.

The consistency values and the corresponding water-to-soil ratios for the gypsum-modified earthen mortars with varying gypsum dosages are presented in Figure 1.

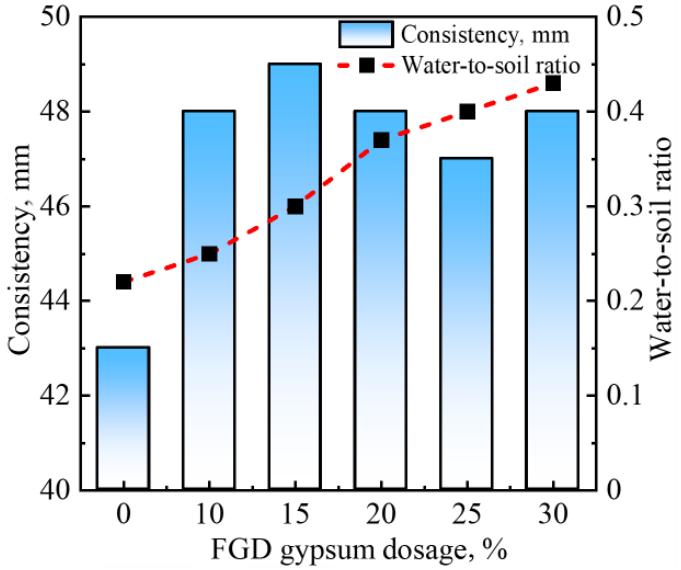

Figure 1 – Effect of a single addition of FGD gypsum on the consistency and water-to-soil ratio of earthen mortar

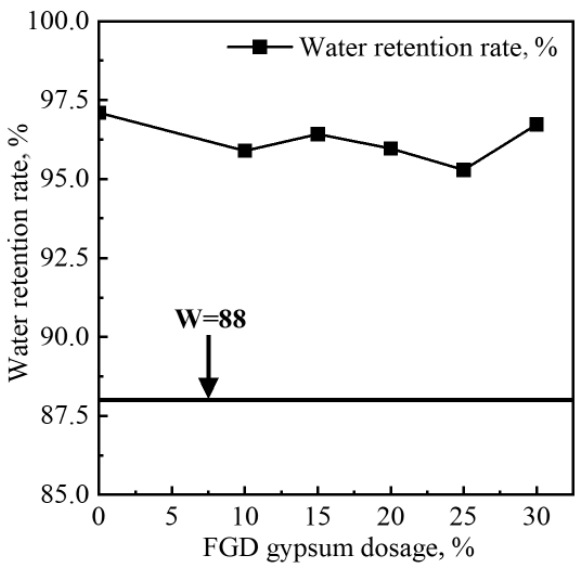

Figure 2 – Effect of a single addition of FGD gypsum on the water retention rate of earthen mortar

It can be observed from the figure that when the consistency of the mortar is controlled within the range of 40 mm to 50 mm, the water-to-soil ratio increases continuously with increasing gypsum content. That is, the addition of gypsum leads to a progressive increase in the amount of water required for mixing. Therefore, a higher water-to-soil ratio is required to maintain the target consistency range. At a gypsum dosage of 30%, the amount of mixing water required is nearly twice that required for mud mortar. The increase in water demand renders the consistency of the mortar difficult to control. Furthermore, the increased water content causes the bonding between soil particles to become looser, and as moisture evaporates, numerous internal pores are left within the set mortar. These factors are collectively detrimental to the proper workability of the earthen mortar.

The phenomenon that the addition of FGD gypsum leads to an increase in the water-to-soil ratio can be explained from three aspects. First, the primary constituent of FGD gypsum is calcium sulfate dihydrate ($CaSO_4 \cdot 2H_2O$), whose crystal structure contains water of crystallization. This crystalline water endows FGD gypsum with a strong affinity for moisture, enabling it to bind with water molecules through hydrogen bonding, thereby exhibiting pronounced hygroscopicity. Under environmental influences, the crystalline water may be released under high-temperature or dry conditions, and reabsorbed in humid environments. Second, FGD gypsum tends to form a porous structure during the production process, containing numerous internal micropores and capillary pores. These pores are capable of adsorbing and retaining moisture, further enhancing their water absorption capacity. In addition, FGD gypsum particles are typically fine and possess a large specific surface area. A larger specific surface area implies a greater number of active surface sites available for the adsorption of water molecules, thus resulting in stronger water absorption.

Water retention refers to the ability of a fresh mortar mixture to retain moisture and resist bleeding, reflecting, to a certain extent, the stability of the mixture. As can be observed from Figure 2, the water retention rates of all groups exceed 88%, meeting the requirements stipulated in the specifications. However, the water retention capacity of the gypsum-modified earthen mortar is slightly decreased compared to that of the unmodified mortar. Poor water retention tends to facilitate the formation of permeable channels within the mortar, leading to severe bleeding. During transportation and construction, rapid moisture loss may cause significant discrepancies in the water content between the upper and lower portions of the mortar, thereby adversely affecting the bond between the mortar and adobe blocks. Concurrently, it can induce non-uniform shrinkage, resulting in shrinkage cracking of the mortar. FGD gypsum is rich in ions that undergo ion exchange with the clay minerals present in the earthen mortar, neutralizing the negative charges on the surfaces of clay particles and disrupting their electrical double-layer structure. This process induces flocculation of the clay particles, reducing their specific surface area and water absorption capacity, and consequently diminishing the water retention of the earthen mortar.

3.2 Effect of gypsum on the volumetric shrinkage rate and compressive strength of earthen mortar

The phenomenon of volumetric shrinkage occurring during the setting process of earthen mortar, also referred to as drying shrinkage, is illustrated in Figure 3.

a) Gap appearing between the specimen and the mold

b) Micro-cracks appearing on the surface of the specimen

Figure 3 – Mud drying shrinkage

The photograph was taken on the third day after casting the specimens. A distinct gap can be observed between the mortar cast in the mold and the mold itself, and some fine cracks have also appeared on the surface of the mortar. Severe drying shrinkage of the mortar is primarily attributed to moisture loss. When traditional earthen mortar hardens in a dry environment, numerous micro-cracks tend to form on the exterior surface. In brick masonry structures, drying shrinkage of the mortar can induce stress concentration, which constitutes a significant factor affecting the overall structural integrity. Concurrently, the shrinkage of the mortar can also adversely affect the quality of the masonry work.

Figure 4 illustrates the volumetric shrinkage rate of earthen mortar modified with a single addition of gypsum and the effect of superplasticizer on the volumetric shrinkage rate of gypsum-modified earthen mortar. As shown in the figure, the volumetric shrinkage rate of the mud mortar specimen is 11.47%, which represents the normal shrinkage behavior of unmodified soil material. With the progressive increase in gypsum content, the volumetric shrinkage rate of the specimens also exhibits a continuous increase. The volumetric shrinkage rate at a gypsum dosage of 30% is 14.49%, representing an increase of 3.07% compared with that of the mud mortar specimen.

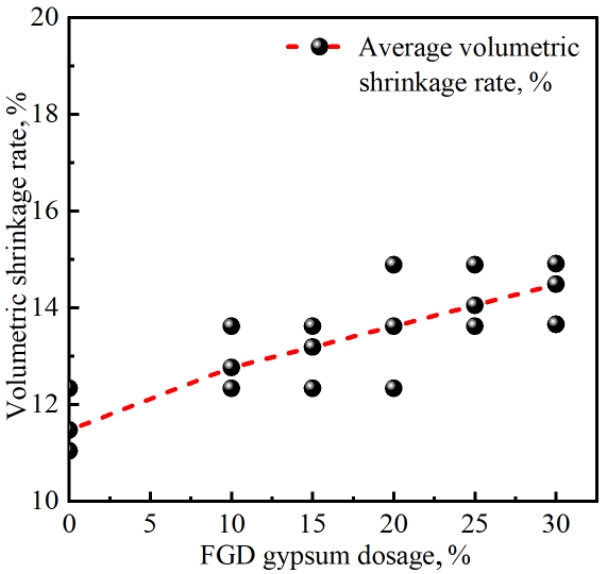

Figure 4 – Volumetric shrinkage rate of specimens with a single addition of gypsum

This observed change may be attributed to the following reasons: First, as established from the relationship between FGD gypsum dosage and the water-to-soil ratio in the preceding experiments, the incorporation of FGD gypsum significantly increases the amount of water required during mixing. During the setting and hardening process of the specimens, the evaporation of this additional moisture induces greater volumetric shrinkage. Second, the chemical composition of FGD gypsum contains two molecules of crystalline water, and the material itself possesses a porous structural characteristic. During the mixing stage, the gypsum absorbs a substantial amount of water to fill its internal pores. In the subsequent drying process, the evaporation of this moisture generates additional voids within the gypsum, providing supplementary space for the overall shrinkage of the specimen. Furthermore, the addition of gypsum may alter the internal microstructure of the earthen mortar, rendering the pathways for moisture migration more unobstructed, thereby accelerating the rate of moisture loss. The combined effect of these factors ultimately results in the gypsum-modified specimens exhibiting a more pronounced volumetric shrinkage phenomenon compared with mud mortar.

The compressive strength of masonry mortar constitutes the most critical performance indicator of the mortar and is also a significant factor influencing the shear resistance of masonry structures. The failure morphology of the mortar specimens is presented in Figure 5.

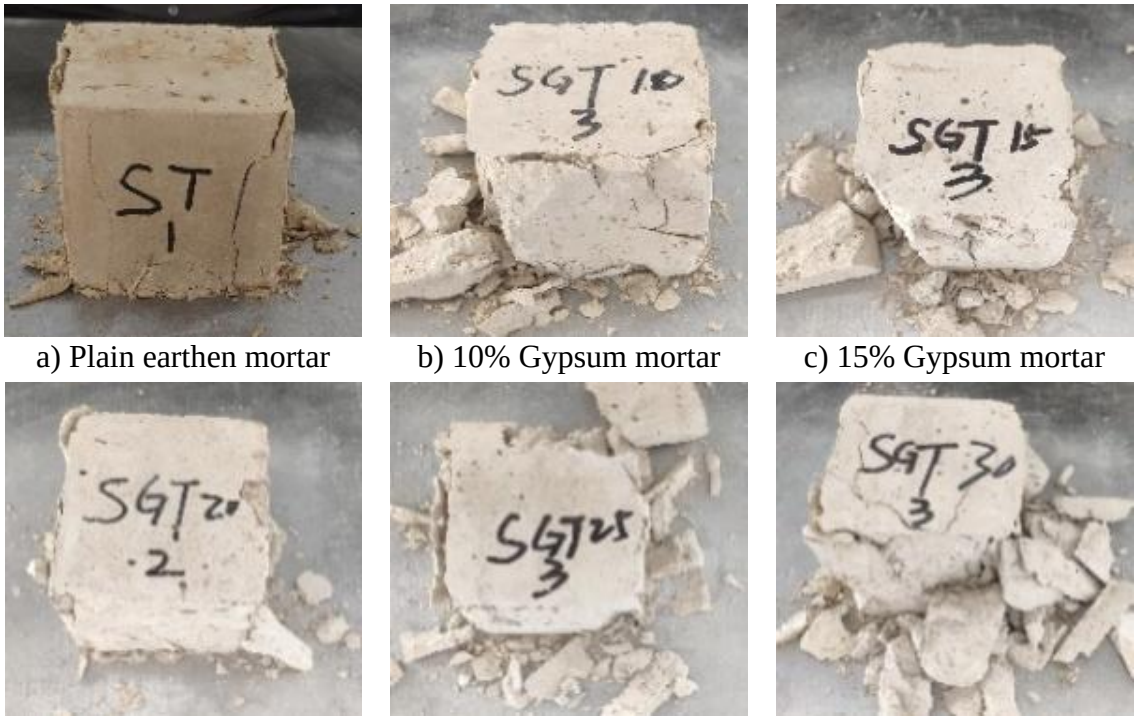

a) Plain earthen mortar b) 10% Gypsum mortar c) 15% Gypsum mortar

d) 20% Gypsum mortar e) 25% Gypsum mortar f) 30% Gypsum mortar

Figure 5 – Compressive strength test of earthen mortar specimens

From left to right, the specimens shown are a mud mortar specimen and those modified with gypsum at dosages ranging from 10% to 30%. It can be observed from the figure that after failure, the mud mortar specimen remains relatively intact as a whole. In contrast, the five gypsum-modified earthen mortar specimens with varying gypsum dosages disintegrate into numerous fragments upon failure. This phenomenon occurs because FGD gypsum, like natural gypsum, is a brittle material. When subjected to compressive stress, it is prone to brittle fracture, resulting in the fragmentation of the material and the formation of debris.

The variation in compressive strength of the specimens with respect to FGD gypsum dosage is presented in Figure 6.

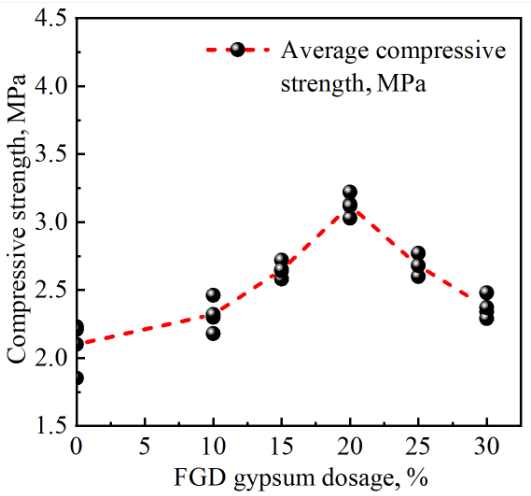

Figure 6 – Compressive strength of specimens with a single addition of gypsum

The compressive strength of the specimens exhibits an initial increasing trend followed by a subsequent decrease as the gypsum dosage increases, reaching a peak value at a gypsum dosage of 20%. The compressive strength of the specimen with a 10% gypsum dosage is 2.32 MPa, representing an increase of approximately 10.5% compared with that of the mud mortar specimen. When the

gypsum dosage is increased to 15%, the compressive strength rises to 2.65 MPa, an increase of 0.55 MPa relative to the mud mortar specimen. At a gypsum dosage of 20%, the compressive strength attains the maximum value among the five groups with varying FGD gypsum dosages, reaching 3.12 MPa, which corresponds to a 49.04% improvement compared with the mud mortar specimen. As the gypsum dosage is further increased to 25% and 30%, the compressive strength of the specimens begins to exhibit a declining trend, with values of 2.68 MPa and 2.37 MPa, respectively; nevertheless, these values remain 27.6% and 12.9% higher, respectively, than that of the mud mortar specimen.

The relatively fine particles of FGD gypsum are capable of filling the pores within the specimen. This kind of filling is expected to improve the specimen's density and overall integrity. The crystal structure of FGD gypsum is comparatively stable. When FGD gypsum is incorporated into the soil, a portion of the calcium sulfate dihydrate dissolves in water, releasing Ca^{2+} and SO_4^{2-} ions. These ions can react with other constituents present in the soil to form potential cementitious substances, such as ettringite ($3CaO{\cdot}Al_2O_3{\cdot}3CaSO_4{\cdot}32H_2O$), which is a substance possessing cementitious properties. The formation of ettringite and other cementitious products establishes a rigid skeletal framework within the specimen, thereby further enhancing its compressive strength [15]. However, excessive formation of such products may induce expansive stresses within the specimen, potentially leading to the initiation of microcracks or structural deterioration, consequently resulting in a reduction in compressive strength.

3.3 Effect of polycarboxylate superplasticizer on the consistency and water retention of gypsum-modified earthen mortar

Based on the investigation of the effects of single modification materials on the consistency, water retention rate, volumetric shrinkage rate, and compressive strength of the earthen mortar, three distinct gypsum dosage levels were selected from each modification category for combined incorporation with superplasticizer in the subsequent experimental study on hybrid addition. The experimental results indicate that FGD gypsum results in water demand during mixing and water retention properties that are inferior to those of mud mortar; however, its effect on compressive strength is improved at dosages of 15% and 20%. To check if the water reducer can effectively counteract the negative effects caused by excessive gypsum. Accordingly, the gypsum dosage levels of 15%, 20%, and 25% were selected for the subsequent combined addition experiments.

The influence of polycarboxylate superplasticizer dosage on the consistency and water-to-soil ratio of the three types of gypsum-modified earthen mortar is presented in Figures 7a, 7b, and 7c.

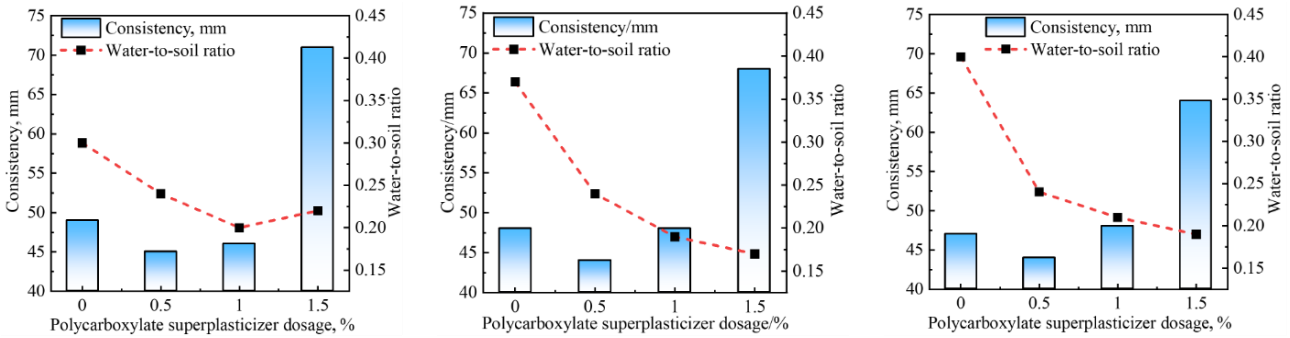

a) 15% FGD gypsum dosage b) 20% FGD gypsum dosage c) 25% FGD gypsum dosage

Figure 7 – Effect of polycarboxylate superplasticizer on the consistency and the water-to-soil ratio of gypsum-modified earthen mortar

The incorporation of polycarboxylate superplasticizer causes the consistency of the three gypsum-modified earthen mortars to exhibit a trend of initially decreasing and subsequently increasing, while also affecting a substantial improvement in the amount of water required for mixing. At superplasticizer dosages of 0.5% and 1.0%, the consistency of all three groups of gypsum-modified mortar was effectively controlled within the range of 40 mm to 50 mm. Moreover, a superplasticizer dosage of 1.0% reduced the mixing water requirement to less than half of the original amount. At a

superplasticizer dosage of 1.5%, the consistency of the mortar increased to values exceeding 60 mm. In the experiment, once mixed to a mortar state, the material exhibited high fluidity, approaching a nearly liquid state, and the consistency could not be maintained within the appropriate range. It can thus be concluded that within a certain range, the dosage of polycarboxylate superplasticizer can reduce the mixing water requirement of the earthen mortar while satisfying workability requirements. Although further increases in superplasticizer dosage can continue to reduce water demand, they readily cause the moisture content to exceed the liquid limit of the soil, rendering the consistency unsuitable for masonry applications.

The incorporation of polycarboxylate superplasticizer also substantially improves the water retention rate of the earthen mortar modified with a single addition of FGD gypsum, as illustrated in Figure 8. Upon the addition of 0.5% superplasticizer, the water retention of the FGD gypsum-modified earthen mortar exhibits an increase, and the water retention performance of the modified mortar continues to improve with increasing superplasticizer dosage. The water retention rate of the 15% FGD gypsum-modified earthen mortar without polycarboxylate superplasticizer is 96.42%, representing a decrease of 0.68% compared with that of mud mortar. After the addition of 0.5% superplasticizer, the water retention rate increases to 98.40%, an improvement of 1.3% relative to the mortar without superplasticizer. Subsequently, as the dosage of polycarboxylate superplasticizer is further increased, the water retention rate continues to exhibit a certain degree of enhancement. Among these several groups of modified mortars, the optimal water retention performance is achieved by the combination of 20% FGD gypsum dosage and 1.5% polycarboxylate superplasticizer, exhibiting a water retention rate of 99.89%. The water retention rates of the remaining two groups, incorporating 0.5% and 1.0% superplasticizer, respectively, also reach 99%.

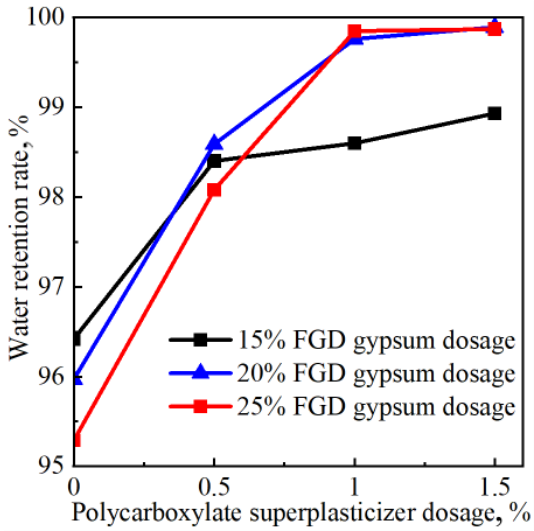

Figure 8 Effect of polycarboxylate superplasticizer on the water retention rate of gypsum-modified earthen mortar

The improvement in water retention of the earthen mortar afforded by the polycarboxylate superplasticizer can be attributed to its ability to regulate the rate of moisture release within the mortar, thereby preserving both the water content and a certain degree of consistency of the mixture [16].

3.4 Effect of polycarboxylate superplasticizer on the volumetric shrinkage rate and compressive strength of gypsum-modified earthen mortar

The volumetric shrinkage rate of the specimens exhibits a marked improvement following the addition of the polycarboxylate superplasticizer. As can be observed from Figure 9, the volumetric shrinkage rate decreases continuously with increasing dosage of the polycarboxylate superplasticizer. At a superplasticizer dosage of 1%, the volumetric shrinkage rates of the three specimens with varying

FGD gypsum contents are all reduced to within 10%. Notably, the volumetric shrinkage rate of the specimen containing 25% FGD gypsum is reduced to 8.82%, representing a decrease of 5.23% compared with the specimen without superplasticizer. At a superplasticizer dosage of 1.5%, the volumetric shrinkage rate of the specimen containing 20% FGD gypsum is merely 6.60%, a value approximately half that of the corresponding specimen without superplasticizer. The experimental results demonstrate that the polycarboxylate superplasticizer can effectively enhance the volumetric stability of the earthen mortar specimens. On one hand, it reduces the water demand, thereby lowering the internal moisture content of the mortar and diminishing the amount of water subject to evaporation, which consequently mitigates the impact of drying shrinkage on volumetric stability. On the other hand, the incorporation of the superplasticizer leads to a reduction in internal porosity and a denser microstructure, which significantly ameliorates the volumetric shrinkage rate of the specimens.

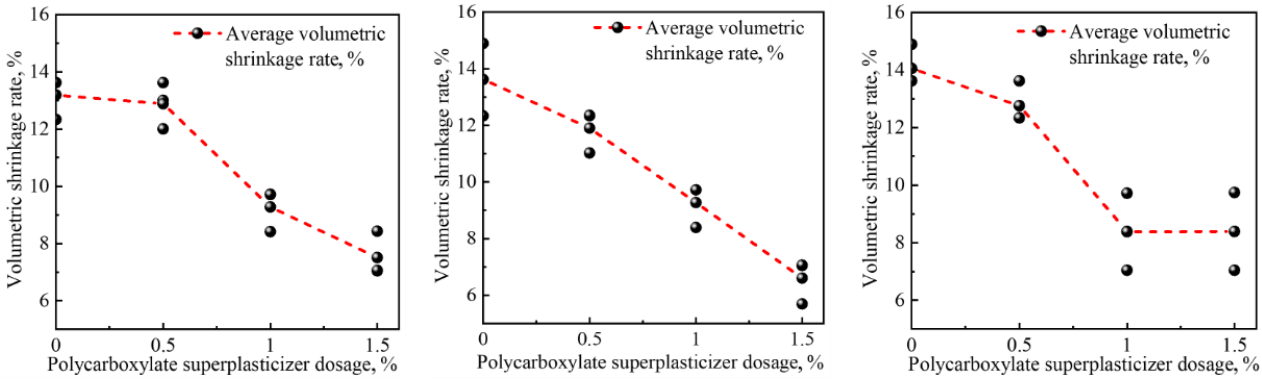

a) 15% FGD gypsum dosage b) 20% FGD gypsum dosage c) 25% FGD gypsum dosage

Figure 9 – Effect of polycarboxylate superplasticizer on the volumetric shrinkage rate of gypsum-modified earthen mortar

The incorporation of polycarboxylate superplasticizer further enhances the compressive performance of the FGD gypsum-modified earthen mortar specimens. The effect on the compressive strength of the earthen mortar specimens modified with 15%, 20%, and 25% FGD gypsum is presented in Figure 10. As shown in the figure, the compressive strength of the FGD gypsum-modified earthen mortar specimens increases continuously with increasing dosage of polycarboxylate superplasticizer. The compressive strength of the mud mortar sample is 2.10 MPa. After the incorporation of 0.5% polycarboxylate superplasticizer into the soils modified with the three different contents of FGD gypsum, the average compressive strengths are 3.01 MPa, 3.34 MPa, and 3.18 MPa, respectively, with the most pronounced improvement observed for the mortar modified with 20% FGD gypsum. When the superplasticizer dosage is increased to 1%, the compressive strengths of the earthen mortars modified with 15% and 20% FGD gypsum both exceed 5 MPa, reaching 5.14 MPa and 5.52 MPa, respectively, representing a significant enhancement in compressive strength. It is 2.45 times and 2.63 times the compressive strength of the reference mud mortar samples, and represents improvements of 94% and 77%, respectively, compared with the FGD gypsum-modified specimens without superplasticizer addition. Adding 1% water-reducing agent to the modified mud mortar with 25% desulfurized gypsum boosted its compressive strength to 3.41 MPa, which is 1.62 times that of the mud mortar, 1.27 times higher than the modified mud mortar without the water-reducing agent, and 7.23% higher compared to the sample with 0.5% water-reducing agent. At a polycarboxylate superplasticizer dosage of 1.5%, the compressive strength of the FGD gypsum-modified earthen mortar specimens continues to rise. The compressive strength of the mortar specimen modified with 20% FGD gypsum reaches 5.96 MPa, representing the highest compressive strength among all modified groups. This value is 2.84 times the compressive strength of the mud mortar and corresponds to an 8% increase relative to the modified mortar specimen incorporating 1% superplasticizer.

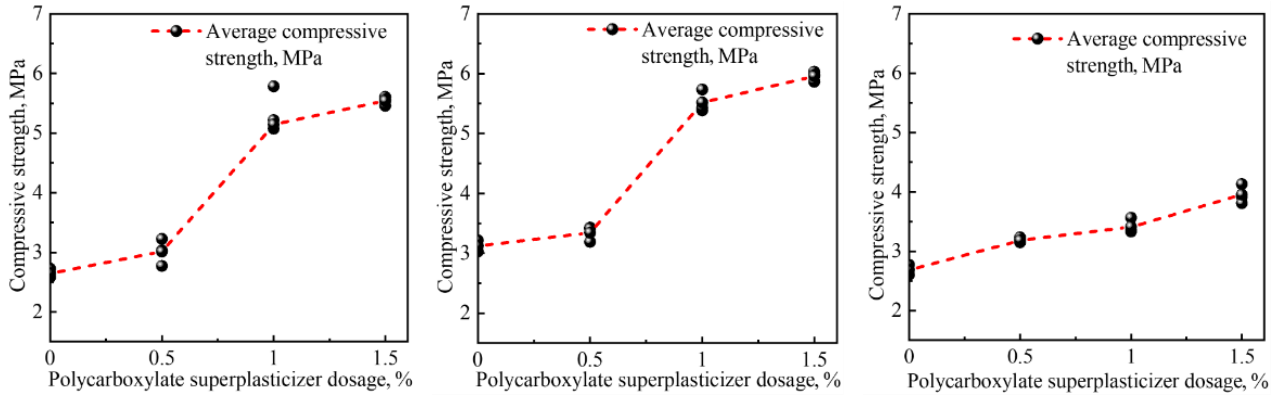

a) 15% FGD gypsum dosage b) 20% FGD gypsum dosage c) 25% FGD gypsum dosage

Figure 10 – Effect of polycarboxylate superplasticizer on the compressive strength of gypsum-modified earthen mortar

4. Conclusions

The effects of a single addition of FGD gypsum at five different dosage levels on the workability, volumetric stability, and compressive strength of plain earthen mortar were first investigated. Based on a comprehensive analysis of the aforementioned experimental results, FGD gypsum dosages of 15%, 20%, and 25% were selected for combined incorporation with polycarboxylate superplasticizer. Through a similar investigation of the workability, volumetric stability, and compressive strength of the resulting mortar, the following conclusions are drawn:

1. To achieve a consistency suitable for masonry requirements, the earthen mortar modified with a single addition of gypsum requires a relatively large amount of water. Polycarboxylate superplasticizer can substantially reduce the water demand; however, the dosage of the superplasticizer should preferably be controlled within the range of 0.5% to 1.0%. When the superplasticizer dosage is increased to 1.5%, it becomes difficult to control the consistency of the mortar. The water retention test was conducted immediately following the consistency test. The incorporation of polycarboxylate superplasticizer results in a significant improvement in the water retention performance of the earthen mortar. When combined with varying dosages of gypsum, the superplasticizer consistently elevates the water retention rate to above 97%.

2. The addition of gypsum increases the water demand, and excessive water content induces pronounced shrinkage in the test specimens. The incorporation of polycarboxylate superplasticizer can reduce the volumetric shrinkage rate of the specimens to half the value observed before its addition. At polycarboxylate superplasticizer dosages of 1.0% and 1.5%, the volumetric shrinkage rate of the specimens can be reduced to below 10%, thereby playing a crucial role in maintaining the volumetric stability of the specimens.

3. The compressive strength of plain earthen mortar specimens is comparatively low. The addition of gypsum enhances their compressive strength, and the experimental results indicate that a gypsum dosage of 20% yields the greatest improvement in the compressive strength of the earthen mortar specimens. Adding a polycarboxylate superplasticizer later further improved the compressive strength of the gypsum-modified mud mortar test blocks. Mixing 20% desulfurized gypsum with 1.5% superplasticizer can make the specimen's compressive strength reach 5.96 MPa, which is 2.84 times that of the mud mortar specimen.

Acknowledgments

This research was funded by the National Natural Science Foundation of China (Grant No. 52268045: Experiment Research and Mechanism Analysis on Mechanical Properties of Composite Mesh Reinforced Adobe Masonry Structure).

References

[1] J. Liu, K. Yuan, S. Zhang, and N. Chen, "Ecological Modification Formula of Raw Soil Masonry Mud," *Bull. Chin. Ceram. Soc.*, vol. 42, no. 2, p. 496, 2023.

[2] J. Qian, W. Qing, and X. Jia, "Research on preparation of adobe materials with desulfurized wastes from coal-fired power plant," *New Build. Mater.*, no. 2, pp. 28–31, 2009.

[3] H. Su, W. Pan, W. Bai, Y. Bai, and X. Yang, "Seismic behavior of new adobe walls structure," *J. Civ. Environ. Eng.*, vol. 37, no. 6, p. 54, 2015, doi: 10.11835/j.issn.1674-4764.2015.06.008.

[4] J. Liu, L. Zhang, and J. Yang, "Research progress of raw earth materials at home and abroad," *Mater. Rep.*, vol. 26, no. 23, p. 14, 2012, doi: 10.3969/j.issn.1005-023X.2012.23.003.

[5] N. Degirmenci, "The using of waste phosphogypsum and natural gypsum in adobe stabilization," *Constr. Build. Mater.*, vol. 22, no. 6, pp. 1220–1224, 2008, doi: 10.1016/j.conbuildmat.2007.01.027.

[6] C. Jayasinghe and N. Kamaladasa, "Compressive strength characteristics of cement stabilized rammed earth walls," *Constr. Build. Mater.*, vol. 21, no. 11, pp. 1971–1976, 2007, doi: 10.1016/j.conbuildmat.2006.05.049.

[7] F. F. Khorasani and M. Z. Kabir, "Experimental study on the effectiveness of short fiber reinforced clay mortars and plasters on the mechanical behavior of adobe masonry walls," *Case Stud. Constr. Mater.*, vol. 16, p. e00918, 2022, doi: 10.1016/j.cscm.2022.e00918.

[8] O. Ige and H. Danso, "Physico-mechanical and thermal gravimetric analysis of adobe masonry units reinforced with plantain pseudo-stem fibres for sustainable construction," *Constr. Build. Mater.*, vol. 273, p. 121686, Mar. 2021, doi: 10.1016/j.conbuildmat.2020.121686.

[9] K. Stathopoulos, M. Apostolopoulou, and A. Bakolas, "Enhancement of water resistance of earthen mortars through stabilization," *Constr. Build. Mater.*, vol. 289, p. 123180, 2021, doi: 10.1016/j.conbuildmat.2021.123180.

[10] K. A. J. Ouedraogo, J.-E. Aubert, C. Tribout, and G. Escadeillas, "Is stabilization of earth bricks using low cement or lime contents relevant?," *Constr. Build. Mater.*, vol. 236, p. 117578, Mar. 2020, doi: 10.1016/j.conbuildmat.2019.117578.

[11] M. Jin, Y. Zhou, B. Wen, L. Liu, and H. Liu, "Progresses of gypsums for the improvement of saline-alkaline soil," *J. Nanjng For. Univ. Nat. Sci. Ed.*, vol. 47, no. 2, pp. 1–8, 2023, doi: 10.12302/j.issn.1000-2006.202209047.

[12] Y. Wang, F. Liu, L. Liu, K. Guan, and K. Zhang, "Experimental analysis on compressive strength of raw soil material modified by industrial waste," *J. Civ. Environ. Eng.*, vol. 38, no. 6, p. 32, 2016, doi: 10.11835/j.issn.1674-4764.2016.06.005.

[13] J. Qian, J. Yu, H. Sun, and y. Ma, "Formation and Function of Ettringite in Cement Hydrates," *J. Chin. Ceram. Soc.*, vol. 45, no. 11, 2017.

[14] M. Xie, "Research on Material Modification and Structure Optimization of Raw Soil Building," in *Dissertation*, Chongqing, China: Chongqing University, 2020, p. 120.

[15] D. Yin, "Study on Gypsum-based Modified Raw Soil Building Materials," in *Dissertation*, Chongqing, China: Chongqing University, 2019, p. 78.

[16] J. Qian, D. Yin, D. Yu, Y. Fan, and Y. Huang, "The effect of polycarboxylate superplasticizer on the properties of modified raw soil materials," *J. Build. Mater.*, vol. 22, no. 03, p. 378, 2019, doi: 10.3969/j.issn.1007-9629.2019.03.008.

[17] S. Wang, Y. Zhao, and Y. Li, *Research and application of desulfurization gypsum for improving saline-alkali soils*. Beijing, China: Science Press, 2020. [Online]. Available: https://liblsp.neau.edu.cn/space/searchDetailLocal/m9239f61399a5c340ecd0f89a0d24bf66

[18] "GB/T 8077-2023 Methods for testing uniformity of concrete admixtures," Beijing, China: State Administration for Market Regulation, China National Standardization Administration, 2023, p. 42.

[19] "JGJT70-2009 Standard for test method of basic properties of construction mortar," in *Bulletin of the Ministry of Housing and Urban*, Beijing, China: Ministry of Housing and Urban-Rural Development of the People's Republic of China, 2009, p. 71.

[20] "RISN-TG008-2010 Technical Guidelines for Ordinary Building Mortar," in *Series of Technical Guidelines for Engineering Construction Standards*, Beijing, China: Ministry of Housing and Urban-Rural Development of the People's Republic of China, 2010, p. 112.

Information about authors:

Sawulet Bekey – Master, Professor, Doctoral supervisor; 1) College of Architecture and Engineering, Xinjiang University, Urumqi, China; 2) Xinjiang Key Laboratory of Building Structure and Earthquake, Xinjiang University, Urumqi, China; jgxyswlt@xju.edu.cn

Wumeng Liu – Master, Assistant Engineer, NO.2 Engineering Co., Ltd. OF CCCC Third Harbor Engineering Co., Ltd., Shanghai, China, 1296544415@qq.com

Qing Wang – Master Candidate, College of Architecture and Engineering, Xinjiang University, Urumqi, China, 2262881295@qq.com

Wenze Wang – Master Candidate, College of Architecture and Engineering, Xinjiang University, Urumqi, China, 1471983186@qq.com
Jingzheng Mi – Master Candidate, College of Architecture and Engineering, Xinjiang University, Urumqi, China, 1028564380@qq.com

Author Contributions:
Sawulet Bekey – funding acquisition, concept, methodology, resources.
Wumeng Liu – data collection, testing, analysis, visualization, interpretation.
Qing Wang – analysis, interpretation, editing.
Wenze Wang – drafting, analysis, interpretation.
Jingzheng Mi – drafting, analysis, interpretation.

Conflict of Interest: The authors declare no conflict of interest.

Use of Artificial Intelligence (AI): The authors declare that AI was not used.

Received: 06.05.2026
Revised: 18.06.2026
Accepted: 24.06.2026
Published: 25.06.2026

Technobius, 2026, 6(2), 0104, DOI: https://doi.org/10.54355/tbus/27897338.6.2.2026.0104

Technobius

https://technobius.kz/

e-ISSN 2789-7338

Article

Flexural behavior of reinforced concrete beams and prediction of failure stages

Abudusaimaiti Kali [1,2], Zihao Wang[1,2], Alipujiang Jierula[1,2,*]

[1]College of Civil Engineering and Architecture, Xinjiang University, Urumqi, China
[2]Xinjiang Key Laboratory of Building Structure and Earthquake Resistance, Xinjiang University, Urumqi, China
*Correspondence: alpj@xju.edu.cn

Abstract. Reinforced concrete (RC) beams are fundamental flexural members in engineering structures. The mechanisms of flexural failure and shear failure differ significantly and directly affect structural safety design. This study systematically investigates the mechanical responses of RC beams with two distinct reinforcement ratios under flexural failure and shear failure. A BP neural network model based on the Bayesian regularization algorithm is developed to predict the failure mode and load state of RC beams. Experimental results of flexural failure indicate that in RC beams, the tensile steel yields first (at a load of 60 kN, the steel strain reaches 1500 με), followed by concrete crushing and the formation of a plastic hinge. The load-deflection curve exhibits a pronounced yield flow stage (deflection jumps from 10.10 mm to 15.15 mm), demonstrating ductile failure with early warning characteristics. In contrast, shear failure tests show that under a short shear span ratio, the beam achieves a higher load-carrying capacity (up to 140 kN, approximately 2.2 times that of the flexural beam) through an arch action. However, the failure is sudden and brittle: as the load increases from 120 kN to 140 kN, the deflection jumps by 4.75 mm, accompanied by a sharp increase in steel strain. Furthermore, the developed BP neural network model takes concrete strain as input and load as output. The regression values for training and testing are all close to 1 (0.994 and 0.996 for the flexural model; 0.999 and 0.998 for the shear model), with small mean square errors. The results demonstrate that the neural network model can predict the load and failure stage of RC beams with high accuracy, providing a reliable basis for engineering design against flexure and shear.
Keywords: reinforced concrete beams, flexural failure test, shear failure test, BP neural network, failure stage.

1. Introduction

Reinforced concrete (RC) beams are the most common flexural members in engineering structures. Their failure modes are mainly influenced by the shear-span ratio (λ), reinforcement ratio (ρ), and stirrup configuration. Flexural failure of the normal section typically manifests as crushing of concrete after yielding of the tensile reinforcement, providing good ductility and warning. In contrast, shear failure of the inclined section is often caused by the propagation of diagonal cracks leading to shear-compression or diagonal tension failure of concrete, characterized by suddenness. Accurately understanding these two failure mechanisms is crucial for structural safety design.

In terms of flexural behavior of the normal section, stress analysis and failure mechanisms based on fracture mechanics and long-term performance have been investigated [1]. Specifically, a fracture mechanics-based program was developed to assess the strength and crack resistance of RC beam elements [2]; a one-dimensional finite element framework incorporating nonlinear material behavior, damage mechanics, and time-dependent effects was proposed to predict the long-term flexural response of RC beams [1]; and the stress intensity factor under bending, involving fracture mechanics analysis of crack propagation, was examined [3].

The performance of beams under serviceability limit states has been investigated. Through finite element analysis, the contribution of the tension stiffening effect to the stiffness of beam

members after concrete cracking was examined [4]. Methods for estimating stress distribution and stiffness of continuous beams under serviceability limit states have also been studied [5].

Flexural behavior and analytical methods for specific beam types have been explored. The finite element method was utilized for ultimate load analysis of RC beams [6]. A comprehensive review of studies on the flexural behavior and design of RC beams strengthened with or using Fiber Reinforced Polymer (FRP) bars as reinforcement or replacement for steel bars has been provided [7].

In terms of the shear behavior of the inclined section, a unified design criterion for shear stress limits has been proposed. Through the design and testing of asymmetrically loaded reinforced concrete deep beams, this research aimed to establish an appropriate unified shear stress limit for RC beam design to simplify the design process and enhance safety [8]. A shear hinge model for analyzing the shear behavior of beams has been developed. This model, which belongs to the concentrated plasticity approach, is capable of capturing complex mechanisms such as shear-moment interaction, nonlinear stress-strain distribution across the section, and concrete softening, thereby providing an effective analytical tool for system-level structural performance assessment [7]. The application of the stress field method for deep beam design has been explored. Through analysis and experimentation, this research investigated the application of the stress field method in the analysis and design of deep beams (particularly those with low shear-span ratios and containing openings), addressing their specific shear mechanics problems [9].

This paper investigates and compares the mechanical responses of RC beams with different reinforcement configurations under two distinct failure modes, analyzes the mechanical response for each failure mode, and establishes models to predict the failure of reinforced concrete beams.

2. Materials and Methods

2.1 Test setup and materials

Figure 1 presents the detailed design drawings of the specimen, while Figure 2 shows the as-built photos.

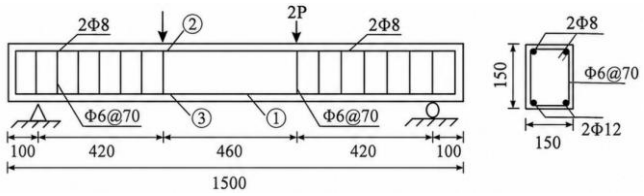

a) Construction drawing of the flexural beam

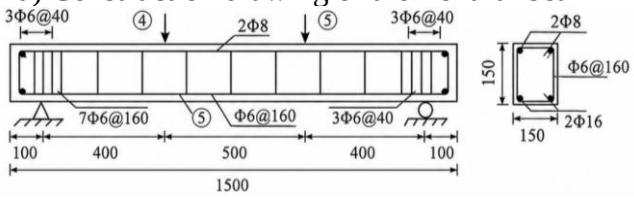

b) Construction drawing of the shear beam

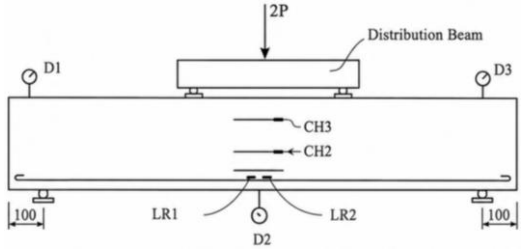

c) Test setup and instrumentation layout

Figure 1 – Test specimens and experimental setup: D – dial gauges (for deflection); CH – strain gauges on the side face of the beam; CP – strain gauges on the top (compression zone) face of the beam; LR – strain gauges on the longitudinal reinforcement

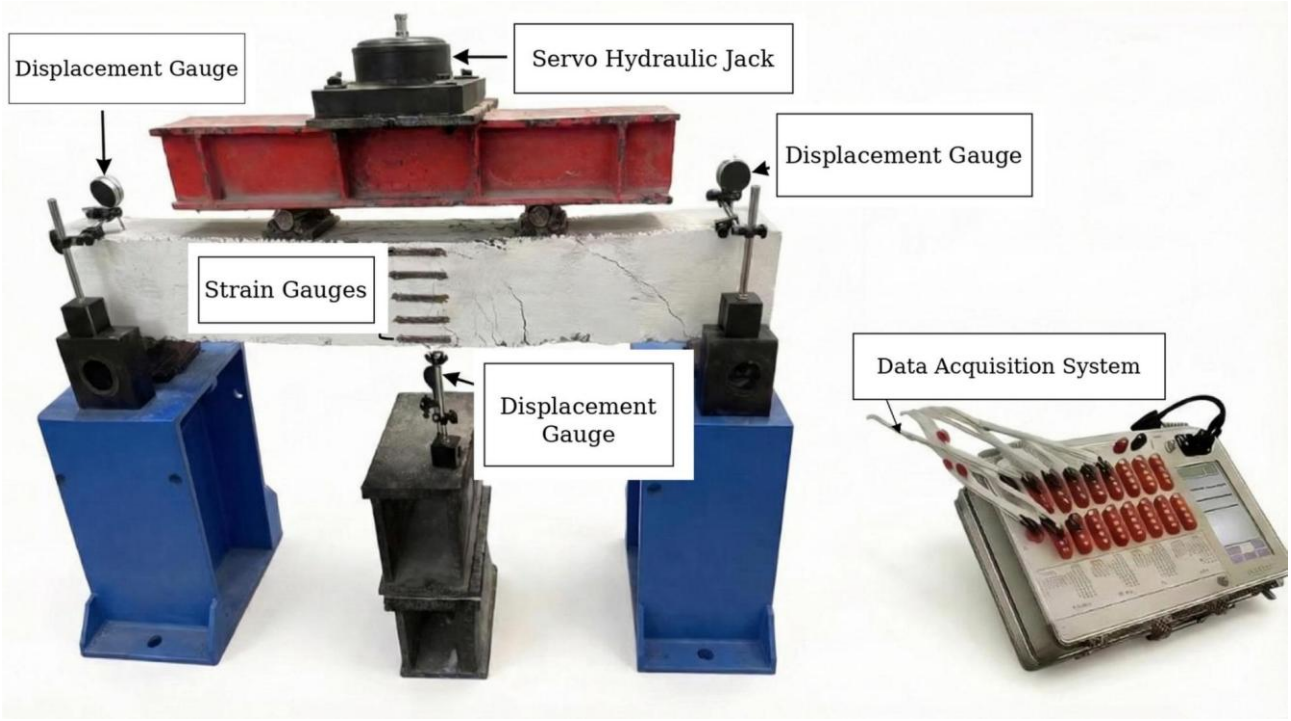

Figure 2 – Photograph of the experimental setup

The longitudinal reinforcement ratio was controlled between ρ_{min} and ρ_{max}. Concrete of grade C30 was used with a mix ratio of 0.44:1:1.328:3.1 (water:cement:sand:coarse aggregate). The specimen configuration for the shear failure test of the supported RC beam is also illustrated. The longitudinal reinforcement ratio similarly satisfied $\rho_{min} \leq \rho \leq \rho_{max}$. The concrete strength grade was C30 (mix ratio consistent with the under-reinforced beam). HRB400 steel bars were used for longitudinal reinforcement, and HPB300 bars were used for hanger bars. The detailed information on the test specimens is provided in Table 1. The major chemical compositions of the cement are presented in Table 2.

Table 1 – Details of test specimens

Category	Parameter	Test 1: Under-reinforced beam (flexural failure-normal section)	Test 2: Shear-critical beam (shear failure-diagonal section)
Geometry	Width b (mm)	150	150
	Height h (mm)	200	200
	Clear Span L (mm)	1500	1500
	Concrete Cover c(mm)	25	25
Concrete	Strength Grade	C 30	C 30
	Mix ratio (water: cement: sand: aggregate)	0.44:1:1.328:3.1	0.44:1:1.328:3.1
	Compressive strength f_{cu}(MPa)	35.0	35.0
	Elastic Modulus E_c(MPa)	3.10×104	3.10×104
Reinforcement configuration	Longitudinal rebar	HPB300, Φ12	HRB400, Φ16
	Compression bars	HPB300, Φ8	HPB300, Φ8
	Stirrups	HPB300,Φ6@70mm	HPB300,Φ6@160mm HPB300,Φ6@40mm
Material Properties	Yield Strength f_y, MPa	340	450
	Elastic Modulus E_s, MPa	2.10×105	2.00×105
Curing	Conditions	Standard curing, 28 days	Standard curing, 28 days
Specimens	Quantity	1	1
Test Protocol	Replication	Each group replicated twice Total: 4 specimens.	Each group replicated twice Total: 4 specimens.

Table 2 – Chemical composition of cement [10]

Oxide	CaO	SiO_2	Al_2O_3	SO_3	Fe_2O_3	MgO	K_2O	TiO_2	P_2O_5	Na_2O
Cement	63.00	20.95	5.39	4.52	3.21	1.34	0.77	0.39	0.19	0.07

A synchronous hydraulic control system, equipped with corresponding hydraulic rams, was used for loading. The setup included a static resistance strain indicator, load cells, dial gauges with magnetic bases, magnifying lenses with scales, steel tape measures, and other related auxiliary tools. The specifications of the equipment used in the tests are presented in Table 3.

Table 3 – Test equipment specifications

Equipment (Model)	Manufacturer
Static strain testing system (DH3818Y)	Jiangsu Donghua Testing Technology Co., Ltd. (Jingjiang, China)
Mechanical dial indicator (321-135W)	Guilin Guanglu Digital Measuring & Control Co., Ltd. (Guilin, China)
Resistance strain gauges (BX120-80AA / BX120-4AA)	Zhejiang Huangyan Test Instrument Factory (Taizhou, China)
Spoke-type load cell (LC.P-500) Servo actuator (MAS-500/500Q) Multi-channel electro-hydraulic servo coordination loading system	Hangzhou Bangwei Electromechanical Control Engineering Co., Ltd. (Hangzhou, China)

2.2 Test content and key points

The tests aimed to analyze the mechanical performance of the beams under load, assess their strength safety margin, measure crack widths, deflections at different load stages, and crack development status. Simultaneously, strain values and their variation trends in critical sections were obtained to study the law of member stiffness variation with load [11].

Given that beam test loads are typically large, multi-point loading often employs a synchronous hydraulic loading system. The load arrangement should follow the design requirements. If actual conditions differ, adjustments are made based on the principle of equivalent load to ensure that the internal force distribution under the test load is essentially consistent with the design internal forces, with equal internal force values at key sections.

The loading process was applied incrementally. Five load levels were used up to the standard load. The self-weight of the specimen and the weight of the loading equipment were included in the initial load. The appearance and development of cracks were recorded visually. Crack widths were measured using a scaled magnifying lens. Under the standard load, the maximum crack widths on both the normal section and the inclined section needed to be measured simultaneously. The flexural crack width was taken as the maximum value at the level of the reinforcement (including the bottom and side faces). Diagonal cracks were measured at their widest point. A schematic diagram of the crack pattern at each load level was drawn on the specimen, annotated with the corresponding load level and crack width.

To accurately determine the cracking load, before loading to the estimated cracking load, each load increment was set at 5% of the standard load (P), and the occurrence of the first crack was closely observed. As failure approached, the failure characteristics were recorded, and the failure load value was determined.

2.3. Failure criteria

The specimen is considered to have failed, and the corresponding load is taken as the failure load, upon the occurrence of any of the following conditions: a) Failure of concrete in the compression zone; b) Fracture of the longitudinal tensile reinforcement; c) The deflection of the member reaches 1/50 of the span after the longitudinal tensile reinforcement yields or exceeds its yield strength; OR the maximum crack width at the location of the longitudinal tensile reinforcement reaches 1.5 mm.

The specimen is considered to have failed, and the corresponding load is taken as the failure load, upon the occurrence of any of the following conditions: a) The width of a diagonal web crack

reaches 1.5 mm, OR shear-compression failure of the concrete occurs at the tip of the diagonal crack; b) Diagonal compression failure of concrete along the inclined section; OR anchorage failure, such as slippage of the main tensile reinforcement at the ends; c) When determining the actual cracking load and failure load of the specimen, the self-weight of the specimen and the weight of loading equipment such as bearing plates and distribution beams acting on the specimen must be included.

2.4. Test procedure

The test procedure was as follows: a) Calculate the load increments based on 20% of the standard load P. The initial load includes the self-weight of the specimen and the weight of equipment like distribution beams; b) Attach strain gauges according to specifications, perform moisture-proof treatment, arrange wiring, and install deflection measurement devices; c) Conduct pre-loading for 1-3 levels, check instrument functionality, and troubleshoot. The pre-load value should be lower than the cracking load; d) During formal loading, the self-weight and loading equipment weight constitute the first load level. If this does not reach the first incremental load level, supplement with additional external load; e) Maintain each load level for 2-5 minutes. Read and record data during the holding period; f) Closely monitor the operation status of instruments and the loading system throughout the test. Record crack development and the final failure mode in detail. Figure 3 shows the crack pattern and failure mode.

3. Results and discussion

3.1 Comparative response of beams under flexural and shear failure

The experimental results show clear differences between the flexural and shear responses of the reinforced concrete beams. Although both specimens were tested under vertical loading, their crack development, load-displacement behavior, reinforcement strain response, and failure mechanisms were substantially different. The flexural beam exhibited a ductile failure mode governed mainly by tensile reinforcement yielding and subsequent concrete crushing, whereas the shear beam showed a more sudden and brittle failure mode controlled by diagonal cracking in the shear span. The observed failure patterns are presented in Figure 3.

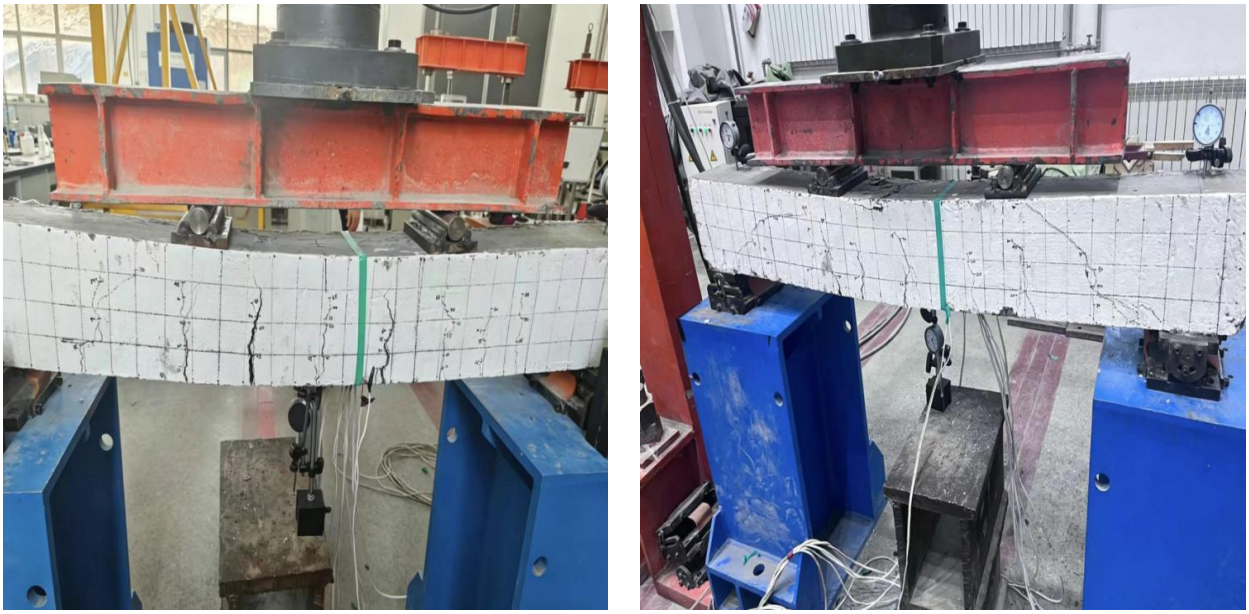

a) Flexural failure b) Shear failure

Figure 3 – Failure modes of specimens

In the flexural beam, vertical cracks developed mainly in the constant-moment region and propagated upward from the tensile zone, as shown in Figure 3a. This crack pattern is typical of

flexural failure, where tensile stresses first cause cracking at the bottom of the beam, followed by progressive stiffness reduction and yielding of the longitudinal reinforcement. The final damage mode indicates that the beam was able to undergo significant deformation before failure. In contrast, the shear beam developed dominant inclined cracks in the shear span, as shown in Figure 3b. These diagonal cracks propagated rapidly toward the loading point and support region, indicating that the inclined section controlled the failure. Compared with the flexural specimen, the crack pattern of the shear specimen was less gradual and more localized, which is consistent with the brittle nature of shear failure.

The difference between the two failure mechanisms is also reflected in the load-displacement curves shown in Figure 4.

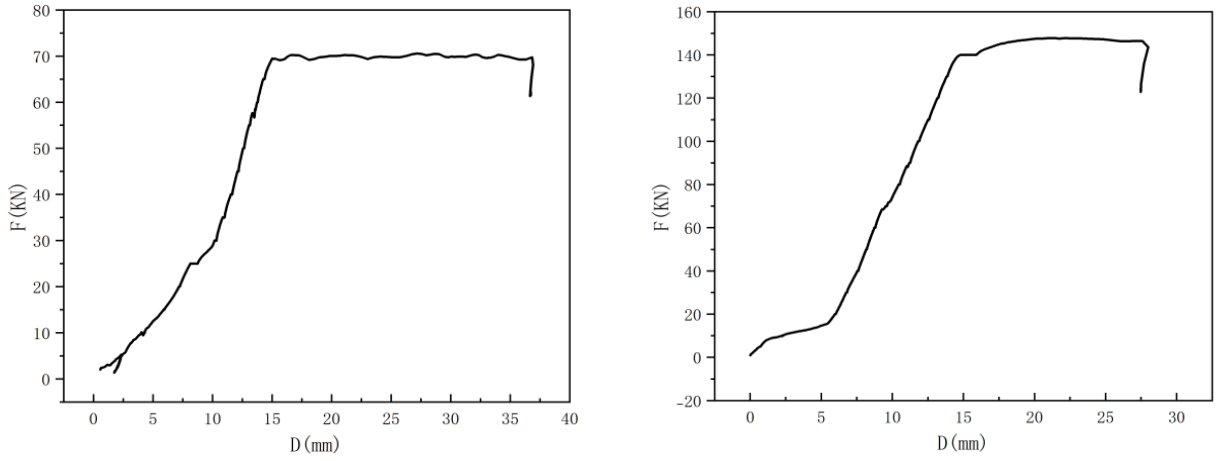

a) Flexural beam b) Shear beam

Figure 4 – Load-displacement curves

For the flexural beam, the curve in Figure 4a shows three main stages. At the initial stage, the load increased with only a small increase in displacement, indicating relatively high initial stiffness before significant cracking. As the load increased, flexural cracks developed in the tensile zone, reducing the effective stiffness of the section and causing a more rapid increase in displacement. Near the peak load, the curve became almost horizontal, showing that the beam had entered the yielding stage. When the load increased from approximately 60 kN to 63 kN, the displacement increased sharply from about 10.10 mm to 15.15 mm. This response indicates that the tangent stiffness had decreased significantly and that a plastic hinge was forming in the critical flexural region. Therefore, the flexural beam displayed ductile behavior with clear deformation development before failure.

The shear beam showed a different load-displacement response, as presented in Figure 4b. Its peak load reached approximately 140 kN, which was about 2.2 times greater than the peak load of the flexural beam. This higher load-carrying capacity can be attributed to the short shear-span behavior and the development of arch action, where part of the load is transferred directly through a compression strut between the loading point and the support. However, the higher capacity was accompanied by lower ductility. At the initial stage, the shear beam showed high stiffness and limited displacement growth. With further loading, diagonal cracks developed, and the stiffness gradually decreased. In the final stage, when the load increased from approximately 120 kN to 140 kN, the displacement increased from about 10.36 mm to 15.11 mm. This sudden displacement increase over a relatively small load interval indicates rapid stiffness loss and unstable diagonal crack propagation. Thus, unlike the flexural beam, the shear beam failed in an abrupt and brittle manner.

The steel stress-strain curves further confirm the different failure mechanisms of the two specimens. For the flexural beam, Figure 5a shows that the tensile reinforcement initially remained within the elastic range, with a nearly linear stress–strain relationship. As the load approached approximately 60 kN, the steel strain reached about 1500 με, corresponding to the yield strain of HPB300 reinforcement. After yielding, the steel strain increased rapidly while the load increased only

slightly. This confirms that the tensile reinforcement yielded before final concrete crushing, which is the expected failure sequence for an under-reinforced flexural member. The reinforcement response is therefore consistent with the ductile load-displacement behavior observed in Figure 4a.

For the shear beam, the steel stress-strain response in Figure 5b indicates a different process. The reinforcement response was approximately linear at lower load levels, but the strain increased more rapidly after diagonal cracking developed. The steel strain exceeded approximately 2000 με at around 90 kN, indicating that the HRB400 reinforcement approached or reached the yield range. At the failure stage, the strain increased sharply, reaching values above 4000 με in some measurements. This sudden increase suggests that, after the formation of major diagonal cracks, internal force redistribution became unstable and the reinforcement was rapidly engaged in resisting shear-induced deformation. Therefore, the strain response of the shear beam supports the conclusion that its failure was sudden and governed by diagonal crack propagation rather than gradual flexural yielding.

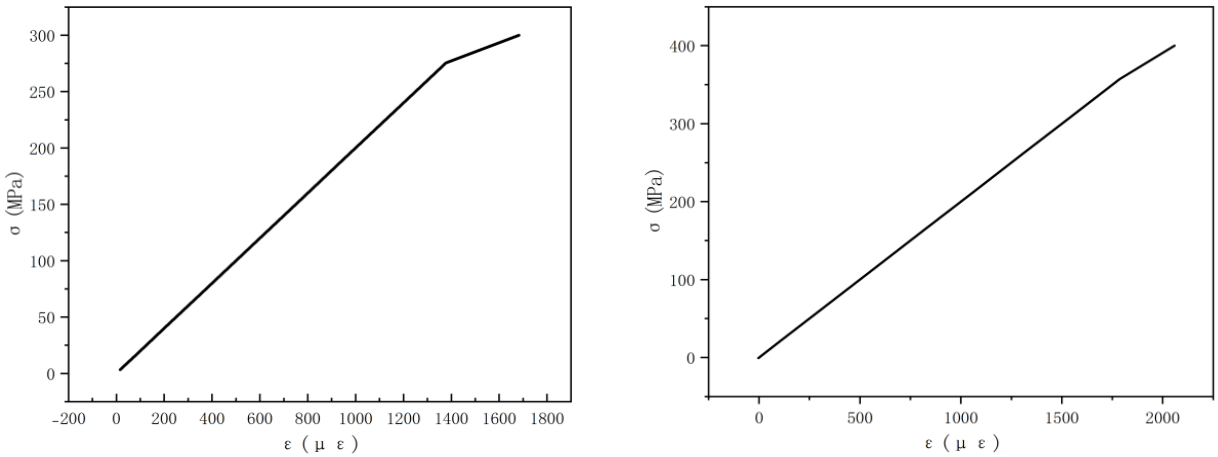

a) Flexural beam b) Shear beam

Figure 5 – Stress-strain curves of the steel reinforcement

The concrete strain distribution and neutral axis movement also provide important evidence for the different responses of the two beams. In the flexural beam, the neutral axis shifted upward gradually as the load increased. This occurred because tensile cracks propagated from the bottom of the beam toward the compression zone, reducing the effective depth of the uncracked concrete section. As a result, the compression zone became smaller, and the compressive strain in the upper concrete fibers increased. This gradual movement of the neutral axis is consistent with flexural crack development and the formation of a plastic hinge after reinforcement yielding.

In the shear beam, the neutral axis movement was less stable near failure because diagonal cracking significantly disturbed the strain distribution across the section. At approximately 120 kN, the measured concrete strains of -560 με at Gauge 1, –328 με at Gauge 2, and 144 με at Gauge 3 indicate that the neutral axis was located near Gauge 2. At 140 kN, the strain at Gauge 2 decreased to approximately –14 με, while the strain at Gauge 3 increased to about 1116 με. This sharp change indicates a rapid upward shift of the neutral axis and a sudden redistribution of stresses caused by diagonal crack development. Such behavior shows that the assumption of a stable flexural strain distribution becomes less applicable as shear failure approaches.

Overall, the experimental results demonstrate that the flexural beam and the shear beam had fundamentally different failure characteristics. The flexural beam reached a lower peak load of approximately 63 kN but showed ductile behavior, including visible flexural cracking, yielding of the tensile reinforcement, large displacement development, and a clear warning before failure. In contrast, the shear beam reached a higher peak load of approximately 140 kN due to arch action, but its failure was sudden and brittle, with rapid diagonal crack propagation, abrupt displacement growth, and sharp reinforcement strain increase. Therefore, although the shear beam had a greater load-carrying capacity, its failure mode was more dangerous from a structural safety perspective. These results

confirm that reinforced concrete beam design should avoid brittle shear failure and should promote ductile flexural behavior wherever possible.

3.2 Prediction of failure stages using a neural network learning model

Artificial Neural Networks (ANNs) are information processing systems that simulate the biological neural networks of the human brain. They are powerful computational algorithms widely used in machine learning. An ANN consists of numerous interconnected nodes, which form the input layer, output layer, and hidden layers. Its functionality is highly dependent on the connections between these nodes. ANNs have been successfully applied to understand complex engineering problems and have demonstrated excellent performance [12].

The Backpropagation (BP) Neural Network is a type of ANN [13]. It employs supervised learning aimed at error minimization, and its algorithm is trained using the backpropagation method. In the BP algorithm, signals propagate forward during the learning process, while errors propagate backward. The structure of a BP network comprises at least three layers: an input layer, a hidden layer, and an output layer. The BP network learning model used in this study was constructed using the Neural Network Toolbox in MATLAB R2025b software. A process diagram of the BP network simulation model used in this study is provided in the corresponding Figure 6.

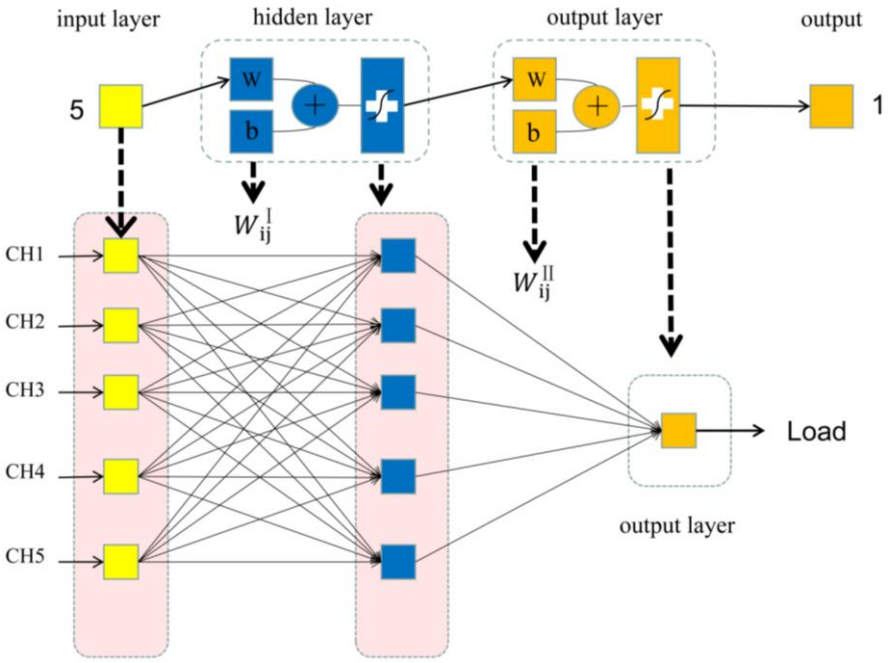

Figure 6 – Schematic of the three-layer BP neural network model

The input sample datasets were obtained from flexural failure tests and shear failure tests on simply supported, under-reinforced (beams with reinforcement ratio within the designed range) RC beams. The first dataset has a size of 6×28 (28 data entries, each containing 6 parameters). The second dataset has a size of 6×32 (32 data entries, each containing 6 parameters). The input variables are the strains in the concrete, and the output parameter is the load applied to the beam.

This study prioritized the use of the Bayesian Regularization algorithm. This selection was primarily based on the following two considerations: First, mechanical tests on concrete are characterized by small sample sizes. Data acquisition is costly, and the sample volume obtained from such tests is often limited. This makes the model highly susceptible to overfitting during training, meaning the model adapts too closely to random noise in the training data rather than the underlying physical principles. The Bayesian Regularization method effectively constrains the complexity of the neural network by introducing a regularization term, thereby enhancing its generalization capability. This ensures the model maintains reliable predictive performance even with unseen data. Second, robustness for engineering applications holds the highest priority. Compared to algorithms focused

merely on training speed, Bayesian Regularization employs a more systematic optimization process. It significantly improves the model's generalization performance and predictive stability, fundamentally ensuring its practicality and reliability for engineering decision-making. In summary, given the task of modeling the mechanical behavior of concrete, which involves scarce data and stringent requirements for predictive robustness, the Bayesian Regularization algorithm achieves a better balance between accuracy and reliability, making it the appropriate choice for this study.

3.3 Data validation

The BP neural network learning model was constructed according to Figure 6. The output of this trained model was designed as the Load, F. The model was trained using the training dataset (80% of the total dataset). The results are shown in the corresponding Figure 7a and 7b.

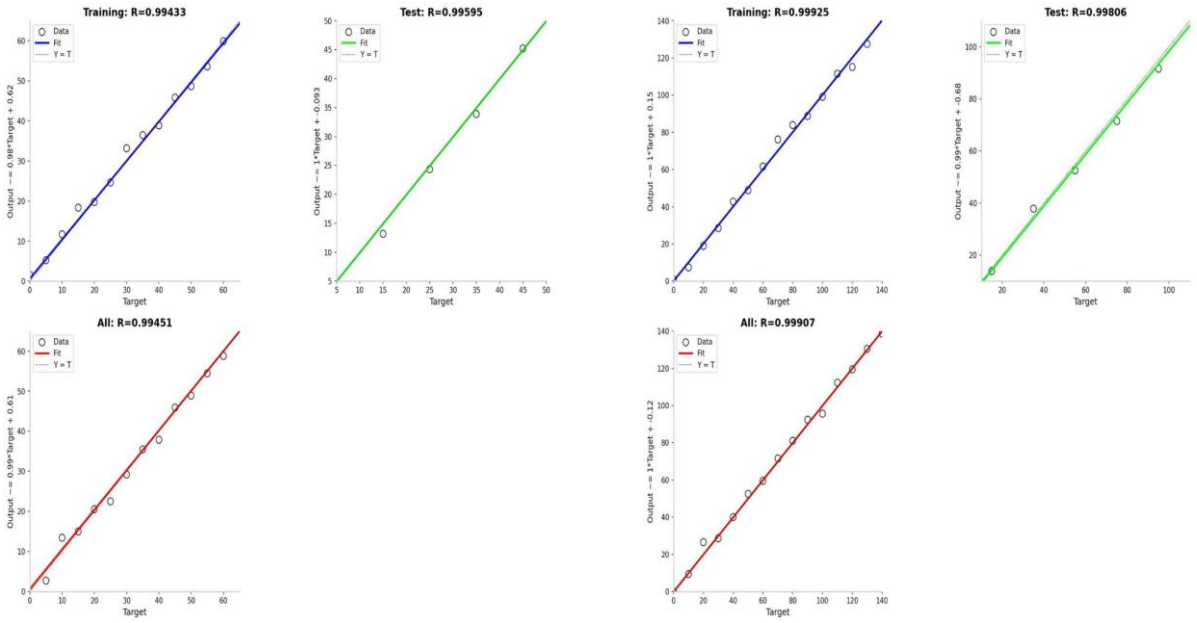

a) Regression plot for the flexural beam b) Regression plot for the shear beam

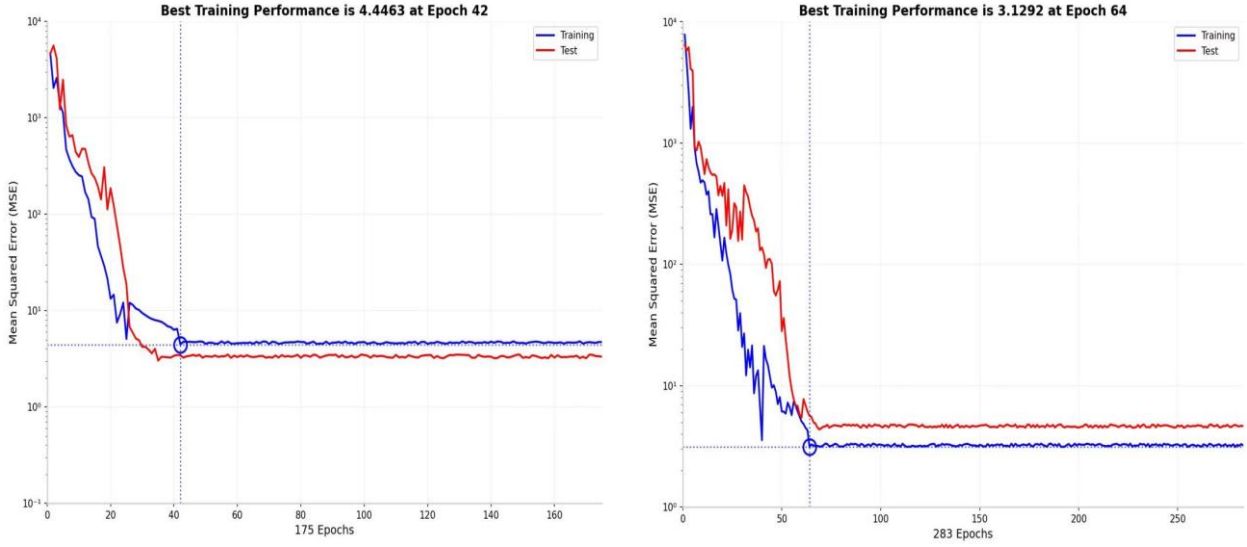

c) Training performance for the flexural beam d) Training performance for the shear beam

Figure 7 – Performance of the BP neural network prediction model

The regression value (R-value) for the trained flexural model is 0.994, and for the trained shear model, it is 0.999. The Mean Squared Error (MSE) for the trained flexural model is 4.446, and for the trained shear model, it is 3.129. The remaining 20% of the dataset was applied to validate the trained model. The results are shown in the corresponding Figures 7c and 7d. The regression value

(R-value) for the validated flexural data is 0.996, and for the validated shear data, it is 0.998. The MSE for the validated flexural model is 2.632, and for the validated shear model, it is 5.430.

Based on the performance of the current models, the BP neural network models trained on both datasets exhibit high regression values (close to 1) and low Mean Squared Errors. Furthermore, the results from the training and testing phases are close. This demonstrates the high accuracy of the models. The models can predict the load applied to an RC beam based on the strain in the concrete. Consequently, they can be used for predicting the failure stage of reinforced concrete beams.

It is noteworthy that the high regression performance (R>0.99) reported herein is derived from a limited sample size (n=28). Given the 80/20 split, the test set is statistically insufficient to capture potential process variability or noise. Thus, while the Bayesian-regularized BPNN demonstrates excellent fitting within the sampled domain, claims of its broad applicability should be tempered. The results primarily serve to establish a proof-of-concept within the specific experimental regime, necessitating future studies with expanded datasets to validate predictive robustness beyond the interpolation range.

4. Conclusion

1. Flexural failure in under-reinforced beams exhibits ductile characteristics. Experimental analysis shows that during the flexural failure of an under-reinforced beam (designed with a reinforcement ratio to ensure steel yields before concrete crushing), the tensile steel yields first. For instance, at a load of 60 kN, the steel strain reached 1500 με. This is followed by the crushing of the concrete, forming a plastic hinge. The load-deflection curve shows a distinct yield plateau, where the deflection increased abruptly from 10.10 mm to 15.15 mm. This failure mode provides ductile warning, adhering to the "yield-before-failure" design principle for under-reinforced beams.

2. Shear failure demonstrates sudden, brittle characteristics. During tests, beams with short shear spans exhibited higher load-carrying capacity (up to 140 kN, 2.2 times that of the flexural beam) through "arch action". However, failure occurred suddenly, characterized by a load increase from 120 kN to 140 kN accompanied by a sharp deflection jump of 4.75 mm and a rapid surge in steel strain. This constitutes a brittle, catastrophic failure mode that must be avoided in engineering practice.

3. The neural network model effectively predicts beam failure. The BP neural network model, based on the Bayesian Regularization algorithm, uses concrete strain as input and load as output. The model achieved high regression values, close to 1, for both training and testing (Flexural: 0.994, 0.995; Shear: 0.999, 0.998), along with low Mean Squared Errors. This confirms the model's high accuracy in predicting the load and identifying the failure stage of reinforced concrete beams, demonstrating its suitability for engineering applications.

Acknowledgments

This work was supported by the National Natural Science Foundation of China (Grant No. 52368051). The abovementioned funding sources and support are gratefully acknowledged.

Reference

[1] B. Bakleh, G. Wardeh, H. Hasan, A. Jahami, and A. Formisano, "A Physically Based 1D Finite Element Framework for Long-Term Flexural Response of Reinforced Concrete Beams," *CivilEng*, vol. 7, no. 1, p. 15, 2026, doi: 10.3390/civileng7010015.

[2] I. I. Luchko and V. F. Lazar, "Evaluation of Stresses in Reinforced-Concrete Beam Elements, Their Strength, and Crack Resistance," *Mater. Sci.*, vol. 38, no. 1, pp. 136–150, 2002, doi: 10.1023/A:1020145420154.

[3] Z. Nuguzhinov *et al.*, "Stress Intensity Factor of Reinforced Concrete Beams in Bending," *Buildings*, vol. 11, no. 7, p. 287, 2021, doi: 10.3390/buildings11070287.

[4] P. L. Ng, J. Y. K. Lam, and A. K. H. Kwan, "Tension stiffening in concrete beams. Part 1: FE analysis," *Proc. Inst. Civ. Eng. - Struct. Build.*, vol. 163, no. 1, pp. 19–28, 2010, doi: 10.1680/stbu.2009.163.1.19.

[5] L. C. Hoang and M. P. Nielsen, "Continuous reinforces concrete beams: stress and stiffness estimates in the serviceability limit state," in *BKM Serie R, Rapporter / Institut for Baerende Konstruktioner og Materialer, Danmarks Tekniske Universitet*, Lyngby, Denmark: Danmarks Tekniske Universitet, 1996, p. 42.

[6] L. Y. Zhou and L. Qiao, "Ultimate Load Analysis of Reinforced Concrete Beam with Finite Element," *Adv. Mater. Res.*, vol. 243–249, pp. 1340–1345, 2011, doi: 10.4028/www.scientific.net/AMR.243-249.1340.
[7] A. R. T. Wayghan and V. Sadeghian, "A Shear Hinge Model for Analysis of Reinforced Concrete Beams," *ACI Struct. J.*, vol. 118, no. 6, pp. 279–291, 2021, doi: 10.14359/51733001.
[8] D. T. W. Looi, R. K. L. Su, and E. S. S. Lam, "A unified shear stress limit for reinforced concrete beam design," *HKIE Trans.*, vol. 22, no. 4, pp. 223–234, 2015, doi: 10.1080/1023697X.2015.1102654.
[9] M. V. G. Silveira and R. A. D. Souza, "Analysis and design of reinforced concrete deep beams using the stress fields method," *Acta Sci. Technol.*, vol. 39, no. 5, p. 587, 2017, doi: 10.4025/actascitechnol.v39i5.28409.
[10] A. Jierula, X. Li, W. Wang, H. Niyazi, and S. Wang, "Experimental study on mechanical properties of polypropylene fiber foamed concrete after exposure to high temperatures," *Case Stud. Constr. Mater.*, vol. 24, p. e05966, 2026, doi: 10.1016/j.cscm.2026.e05966.
[11] A. Jierula, S. Ding, H. Liu, and B. Yang, "Damage Evolution in Different Reinforcement Configurations during Four-Point Bending: Acoustic Emission Analysis Using K-means Clustering," *J. Nondestruct. Eval.*, vol. 45, no. 1, p. 40, 2026, doi: 10.1007/s10921-026-01333-x.
[12] A. Jierula, T.-M. Oh, S. Wang, J.-H. Lee, H. Kim, and J.-W. Lee, "Detection of damage locations and damage steps in pile foundations using acoustic emissions with deep learning technology," *Front. Struct. Civ. Eng.*, vol. 15, no. 2, pp. 318–332, 2021, doi: 10.1007/s11709-021-0715-y.
[13] A. Jierula, S. Wang, T.-M. Oh, J.-W. Lee, and J. H. Lee, "Detection of source locations in RC columns using machine learning with acoustic emission data," *Eng. Struct.*, vol. 246, p. 112992, 2021, doi: 10.1016/j.engstruct.2021.112992.

Information about authors:
Abudusaimaiti Kali – MSc; 1) College of Civil Engineering and Architecture, Xinjiang University, Urumqi, China; 2) Xinjiang Key Laboratory of Building Structure and Earthquake Resistance, Xinjiang University, Urumqi, China; abdusmt@xju.edu.cn
Zihao Wang – Bachelor Student; 1) College of Civil Engineering and Architecture, Xinjiang University, Urumqi, China; 2) Xinjiang Key Laboratory of Building Structure and Earthquake Resistance, Xinjiang University, Urumqi, China; 880711@stu.xju.edu.cn
Alipujiang Jierula – PhD; 1) College of Civil Engineering and Architecture, Xinjiang University, Urumqi, China; 2) Xinjiang Key Laboratory of Building Structure and Earthquake Resistance, Xinjiang University, Urumqi, China; alpj@xju.edu.cn

Author Contributions:
Abudusaimaiti Kali – methodology, testing, modeling, analysis, interpretation, editing.
Zihao Wang – data collection, testing, analysis, visualization, drafting, editing.
Alipujiang Jierula – concept, methodology, resources, testing, analysis, interpretation, editing, funding acquisition.

Conflict of Interest: The authors declare no conflict of interest.

Use of Artificial Intelligence (AI): The authors declare that AI was not used.

Received: 02.05.2026
Revised: 20.06.2026
Accepted: 25.06.2026
Published: 26.06.2026